Doctoral theses at NTNU, 2017:365

Knut Andreas Kvåle

Dynamic behaviour of floating bridges exposed to wave excitation

A numerical and experimental investigation

NTNU
Norwegian University of
Science and Technology

Doctoral thesis

Knut Andreas Kvåle

ISBN 978-82-326-2800-1 (printed ver.)
ISBN 978-82-326-2801-8 (electronic ver.)
ISSN 1503-8181

NTNU

Norwegian University of Science and Technology
Thesis for the Degree of
Philosophiae Doctor
Faculty of Engineering
Department of Structural Engineering

Doctoral theses at NTNU, 2017:365

NTNU
Norwegian University of
Science and Technology

Knut Andreas Kvåle

Dynamic behaviour of floating bridges exposed to wave excitation

A numerical and experimental investigation

Thesis for the Degree of Philosophiae Doctor

Trondheim, December 2017

Norwegian University of Science and Technology
Faculty of Engineering
Department of Structural Engineering

NTNU
Norwegian University of
Science and Technology

NTNU
Norwegian University of Science and Technology

Thesis for the Degree of Philosophiae Doctor

Faculty of Engineering
Department of Structural Engineering

ISBN 978-82-326-2800-1 (printed ver.)
ISBN 978-82-326-2801-8 (electronic ver.)
ISSN 1503-8181

Doctoral theses at NTNU, 2017:365

Printed by NTNU Grafisk senter

Abstract

By utilizing the buoyancy of the water in a crossing, floating bridges may provide permanent road links where other bridge types would be impossible or too costly to build. Still, floating bridges are not wide-spread in modern road infrastructure. One major issue in this regard is the lack of available information about the performance of existing floating bridges, and consequently, how well the numerical prediction methodology enables an accurate description of their real-life behaviour. The fluid-structure interaction combined with dynamic and stochastic excitation makes numerical prediction of floating bridges a complex problem.

A better understanding of the dynamic behaviour of floating bridges would be highly valuable for the design of new floating bridges. The accuracy of the numerical prediction methodology is a crucial consideration for both the general trust in the numerical models, but also for reducing the required safety margins in designs.

This dissertation concerns the issues listed above by means of numerical modelling using state-of-the-art methodology and a comprehensive monitoring system installed on the Bergsøysund Bridge, an existing floating pontoon bridge. The dynamic response of the Bergsøysund Bridge is predicted within the framework of the finite element method and compared with the measured response. Furthermore, by applying operational modal analysis, the modal parameters are determined experimentally from the recorded data, and compared with the modal parameters resulting from the solution of the eigenvalue problem of the numerical model.

For realistic sea states, the case study reveals that the response is only weakly dependent on the directional spreading of the wave field. Furthermore, the correlation between the wave excitation at the different pontoons is very low, such that the wave spectral density matrix may be approximated to be block-diagonal without significant effects to the resulting response spectral density. The predicted and measured lateral response quantities are for most cases in good agreement. Predictions of the vertical response is not accurate when considering how the energy is distributed over relevant frequencies, but standard deviations are normally accurately predicted. Torsional response is not predicted with a satisfactory accuracy. The operational modal analysis does prove to be challenging. Large damping, closely spaced modes, and an arc-shaped design prone to coupled motion are factors that complicate the task. Modal damping ratios as high as 12–14% are observed both numerically and experimentally. Some of the experimental mode shapes are comprised of a mix of multiple of the predicted mode shapes, where the amount and fashion of the mixing is varying from recording to recording. This may indicate a modal coupling of the mode shapes, which implies that energy is transferred between modes. The variability of the identified natural frequencies drops as the significant wave height, which characterize the excitation level, increases. Furthermore, the damping levels are increasing for increasing excitation level.

Floating bridges are structures prone to complex dynamic behaviour. The importance of verification of numerical models should therefore be emphasized. Due to this, the current work is considered to be relevant for the future development of floating bridges.

Acknowledgements

This study was conducted with financial support from the Norwegian Public Roads Administration. I gratefully appreciate this support.

I would like to express my sincere gratitude to my main supervisor, Associate Professor Ole Øiseth, for his encouragement and support, and for sharing his valuable knowledge. His ability to quickly tackle new scientific and theoretical challenges has been a great resource. Furthermore, special thanks are extended to my co-supervisor, Professor Anders Rønnquist, for his ability to take a step back and see things from a broader perspective, and for common conference travels. Together, Ole and Anders' low-key and friendly approach to becoming, untrained researchers, has made this a very memorable experience. My last co-supervisor, the late Professor Ragnar Sigbjörnsson, was a big inspiration for me as an academic aspirant during the first year of my PhD study. His vast knowledge and humble approach to other humans will never be forgotten.

My office mate, Petter Nåvik, deserves special thanks for being an excellent discussion partner and good company. Thank you for taking this knowledge-gaining experience together with me.

I would also like to extend my thanks to researchers Torodd Nord, Finn-Idar Grøtta Giske, Svein Remseth, and Bernt Leira, for scientific collaboration with common publications, and to PhD candidates Aksel Fenerci and Øyvind Wiig Petersen for scientific cooperation and valuable discussions. I would also like to thank the following researchers and colleagues, working on other scientific topics involving structural dynamics: Gunnstein T. Frøseth, Bartosz Siedziako, Yuwang Xu, Daniel Cantero, Michael Styrk Andersen, Tor Martin Lystad, Henrik Skyvulstad, Tore A. Helgedagsrud, Bjørn T. Svendsen, and Stefano Derosa.

Furthermore, I would like to thank my other colleagues at the Department of Structural Engineering for providing a stimulating and enjoyable working environment. Thanks are also extended to the laboratory personnel at the department, for their assistance in the installation of the monitoring system. Gøran Loraas deserves special thanks for his efforts in this regard.

Elsevier, the publisher of the three first appended papers, granted the permission to include the published papers in the thesis. This is highly appreciated. Thanks are also extended to all the anonymous reviewers that have provided valuable and constructive feedback during the review processes of the papers.

Finally, I would like to direct big thanks to my family and friends for their support. In particular, I would like to express my deepest gratitude to my dear wife Heidi. Your patience and unconditional support have been invaluable for this work, and I am forever grateful for the sacrifices you have made to make this possible.

Preface

This thesis is submitted in partial fulfilment of the requirements for the degree *Philosophiae Doctor* at the Norwegian University of Science and Technology (NTNU). The work has been carried out at the Department of Structural Engineering, Faculty of Engineering.

Associate Professor Ole Øiseth, Professor Anders Rönnquist and the late Professor Ragnar Sigbjörnsson have supervised the work.

The thesis is based on journal and conference papers that are either published or submitted.

Knut Andreas Kvåle

Trondheim, Norway
August 31, 2017

List of appended papers

The main part of the thesis is comprised of the following five papers:

Paper 1 K. A. Kvåle, R. Sigbjörnsson, and O. Øiseth, "Modelling the stochastic dynamic behaviour of a pontoon bridge: A case study", Computers & Structures, vol. 165, pp. 123–135, Mar. 2016. doi:10.1016/j.compstruc.2015.12.009

Paper 2 K. A. Kvåle and O. Øiseth, "Structural monitoring of an end-supported pontoon bridge", Marine Structures, vol. 52, pp. 188–207, Mar. 2017. doi:10.1016/j.marstruc.2016.12.004

Paper 3 K. A. Kvåle, O. Øiseth, and A. Rønnquist, "Operational modal analysis of an end-supported pontoon bridge", Engineering Structures, vol. 148, pp. 410–423, Oct. 2017. doi:10.1016/j.engstruct.2017.06.069

Paper 4 K. A. Kvåle and O. Øiseth, "Dynamic response of an end-supported pontoon bridge due to wave excitation: numerical predictions versus measurements", Submitted for journal publication, 2017.

Paper 5 K. A. Kvåle and O. Øiseth, "Characterization of the wave field around an existing end-supported pontoon bridge from simulated data", in Proceedings of the International Conference on Earthquake engineering and Structural Dynamics, Reykjavik, Iceland, 2017.

Other scientific contributions

The following papers resulted from the work during the PhD study, in addition to the five appended papers:

K. A. Kvåle, O. Øiseth, and R. Sigbjörnsson, "Modelling of the stochastic dynamic behaviour of the Bergsøysund Bridge," in Proceedings of the 26th Nordic Seminar on Computational Mechanics, 2013, pp. 100–103.

K. A. Kvåle, O. Øiseth, and R. Sigbjörnsson, "Modelling of the stochastic dynamic behaviour of the Bergsøysund Bridge: an application of the power spectral density method," in Proceedings of the 9th International Conference on Structural Dynamics, EURODYN 2014, 2014, pp. 2921–2928.

K. A. Kvåle, O. Øiseth, A. Rønnquist, and R. Sigbjörnsson, "Modal Analysis of a Floating Bridge Without Side-Mooring," in Dynamics of Civil Structures, Volume 2, vol. 2, Springer, 2015, pp. 127–136. doi:10.1007/978-3-319-15248-6_14

O. Øiseth, A. Rönnquist, K. A. Kvåle, and R. Sigbjörnsson, "Monitoring wind velocities and dynamic response of the Hardanger Bridge," in Conference Proceedings of the Society for Experimental Mechanics Series, 2015, vol. 2, pp. 117–125. doi:10.1007/978-3-319-15248-6_13

K. A. Kvåle, O. Øiseth, and A. Rönnquist, "Covariance-Driven Stochastic Subspace Identification of an End-Supported Pontoon Bridge Under Varying Environmental Conditions," in Dynamics of Civil Structures, Volume 2. Conference Proceedings of the Society for Experimental Mechanics Series., J. Caicedo and S. Pakzad, Eds. Cham: Springer International Publishing, 2017, pp. 107–115. doi:10.1007/978-3-319-54777-0_14

K. A. Kvåle, O. Øiseth, A. Rönnquist, and S. Remseth, "Simulation and monitoring of floating bridge behaviour," in Earthquake Engineering and Structural Dynamics in Memory of Ragnar Sigbjörnsson, 2018. In press.

F.-I. G. Giske, K. A. Kvåle, B. J. Leira, and O. Øiseth, "Long-term extreme response analysis of a long-span pontoon bridge," Marine Structures, vol. 58, pp. 154–171, Mar. 2018. doi:10.1016/j.marstruc.2017.11.010

T. S. Nord, K. A. Kvåle, Ø. W. Petersen, M. Bjerkås, and E.-M. Lourens, "Operational modal analysis on a lighthouse structure subjected to ice actions," Procedia Engineering, vol. 199, pp. 1014–1019, Jan. 2017. doi:10.1016/J.PROENG.2017.09.268

Contents

1 Introduction

1.1 Background

Floating bridges have existed for four millennia [1], but have only been used as road links in modern infrastructure since around 1940. A list of the longest modern floating bridges for road vehicle traffic is given in Table 1. By utilizing the water in the crossing, the structure may benefit from large stiffness originating from the buoyancy and added damping from the fluid-structure interaction, which in most cases will be beneficial for the dynamic behaviour. It does, however, come at the cost of potentially large forces due to the currents and waves, and a more complex dynamic behaviour.

The Norwegian Public Roads Administration (NPRA) is currently planning a new Coastal Highway, E39, along the Norwegian west-coast, where existing ferry connections will be exchanged with permanent road links. Close to half of the traditional Norwegian export is generated in the areas surrounding the planned highway [2], and saved time in transportation will result in significant benefits to the industry. The fjord-dense geography dominating the route poses a big challenge for the bridge designs; the straits are deep and wide, and will require significant extension of the current bridge technology. For several of the crossings, floating bridges are deemed among the most feasible and economic alternatives.

1.1.1 Dynamic behaviour of floating bridges

The first floating bridges built were not designed with emphasis on their dynamic behaviour. Two research groups were simultaneously exploring the dynamics of floating bridges in the 70s and 80s: the research group at the University of Washington in the United States, led by Hartz [3–7]; and the research group at NTNU and SINTEF in Norway, led by Holand and Langen [8–10]. Borgman [11] systematized the methodology for conducting time simulations of waves. Furthermore, Langen and Sigbjörnsson [12, 13] elaborated and exemplified the methodology for dynamic analysis of floating bridges, with case studies on the Nordhordland Bridge (referred to as the Salhus Bridge at the time); and researchers at NTNU and SINTEF [14, 15] made further developments in cooperation with the NPRA. The early history of floating bridges in the State of Washington played a key role to set the agenda for the research conducted in the United States, whereas the experience drawn from the Norwegian oil adventures on the Norwegian Continental Shelf was defining in the development of and research on floating bridges in Norway. While the floating bridges in Washington are relying on a straight single-pontoon girder with side-anchoring to the seabed, the floating bridges in Norway are horizontally curved structures with discretely distributed pontoons and no side-anchoring. Even though the two types of structures have a lot in common, they are principally very different. A design without side-mooring would have to be

Tab. 1: Floating road bridges used as part of modern infrastructure. Bridges no longer in operation are not listed unless they have been replaced by newer versions.

Name	Length[+]	Location	In operation	Design
Lacey V. Murrow Memorial Bridge[1]	2020 m	Washington, United States	1940–[†]	Horizontally straight side-anchored continuous pontoon deck
Kelowna Floating Bridge (Okanagan Lake Bridge)	650 m	British Columbia, Canada	1958–2008	Horizontally straight side-anchored continuous pontoon deck
William R. Bennett Bridge (Okanagan Lake Bridge)[*]	690 m	British Columbia, Canada	2008–	Horizontally straight side-anchored continuous pontoon deck and elevated end-section
Governor Albert D. Rosellini Bridge (Evergreen Point Floating Bridge)[2]	2310 m	Washington, United States	1963–2016	Horizontally straight side-anchored continuous pontoon deck
New Governor Albert D. Rosellini Bridge (Evergreen Point Floating Bridge)[*]	2350 m	Washington, United States	2016–	Horizontally straight side-anchored continuous pontoon deck
William A. Bugge Bridge (Hood Canal Bridge)	1988 m	Washington, United States	1961–[‡]	Horizontally straight side-anchored continuous pontoon deck
Demerara Harbour Bridge[o]	1851 m	Georgetown, Guyana	1978–	Horizontally straight with discrete steel pontoons and side-anchoring
Homer M. Hadley Memorial Bridge[3]	1772 m	Washington, United States	1989–	Horizontally straight side-anchored continous pontoon deck
Bergsøysund Bridge	840 m	Møre og Romsdal, Norway	1992–	Horizontally curved with discrete pontoons and no side-anchoring
Nordhordland Bridge (Salhus Bridge)	1246 m	Hordaland, Norway	1994–	Horizontally curved with discrete pontoons, no side-anchoring and a cable-stayed fixed section
Yumemai Bridge (Yumeshima-Maishima Bridge)	410 m	Osaka, Japan	2000–	Horiozontally straight swing arch bridge, with two pontoons

[+] Length of floating section
[1] Commonly referred to as 1st Lake Washington Bridge
[†] Collapsed in 1990, but repaired and reopened
[*] Replaced the bridge listed above
[2] Commonly referred to as 2nd Lake Washington Bridge
[‡] Collapsed in 1979, but repaired and reopened
[o] Originally intended for temporary use
[3] Commonly referred to as 3rd Lake Washington Bridge

based on a philosophy of high flexibility, in contrast to side-anchored designs that as a result are much stiffer.

Due to the experiences drawn from the design of the Bergsøysund and Nordhordland Bridges, Norwegian consultant companies were engaged when the old Kelowna Floating Bridge in British Columbia, Canada, was planned to be replaced by a new, modern floating bridge. The project resulted in new research on the dynamics of floating bridges, in Canada, led by Isaacson [16–18].

In the late 90s, a massive research project named the Mega-Float [19, 20] was initiated. Following this, research in regard with the plans of a new swing-type floating bridge, the Yumemai Bridge, emerged [21, 22].

The above-listed references are mainly concerning the simulation and modelling of floating structures, and do only in a few selected cases involve measurement of their true behaviour. Peterson [23] compared the measured and predicted response of the Evergreen Point Floating Bridge, later renamed to Governor Albert D. Rosellini Bridge; however, with emphasis on the performance of the mooring cables. A preliminary comparison between the measured and predicted response of the Hood Canal Bridge was conducted by Georgiadis [6], as a consequence of its collapse during a storm in 1979. There exist substantial amounts of research concerning testing of dynamic behaviour of various structures. Studies comparing predicted and experimental response of floating bridges are, however, close to non-existing. This is explained by the small amount of existing test subjects compared to, e.g., suspension bridges. The uncertainties of the methods used to estimate dynamic behaviour of floating bridges are therefore not well-known, which leads to a high conservatism in design and unnecessarily high construction costs, in the best case.

1.1.2 Studying the Bergsøysund Bridge

The Bergsøysund Bridge is a 930-metre-long pontoon bridge located in Møre og Romsdal county on the western coast of Norway. It provides a permanent road link between the islands Bergsøya and Aspøya. Seven floating concrete pontoons are supporting the steel truss, which are providing additional stiffness, damping and mass to the system. The arc-shaped design of the bridge is ensuring that axial forces at the abutments are supporting the bridge laterally. Therefore, a steel rod is placed on each of the ends, for the absorption of axial forces. Furthermore, rubber bearings are providing vertical and lateral support. A photograph of the bridge is given in Figure 1, and the bridge location is depicted in the map shown in Figure 2. The bridge has no side-mooring and relies solely on the support provided at its ends, and thus the design philosophy is based on a high flexibility. This makes the structure susceptible to large displacements and dynamic behaviour. It was completed in 1992 and is the first long-span floating bridge without side-mooring in existence.

The current study investigates the behaviour of the Bergsøysund Bridge by means of an extensive monitoring system, which enables a precise description of the dynamic behaviour of the structure. The recorded response is compared with numerical predictions to assess the accuracy of the applied methodology.

Furthermore, operational modal analysis is applied to the recorded acceleration data to estimate the modal parameters of the bridge. The field of modal analysis has seen numerous applications in civil structures, as in, e.g., [24–28]. Larssen [29] presented methodology to estimate the structural parameters from response measurements only, with emphasis on applications to submerged floating tunnels. Because no vibration data from real-life structures were available at the time of that study, simulated response and measurements from a scale model in a wave basin

Fig. 1: The Bergsøysund Bridge. Photograph by NTNU/K. A. Kvåle.

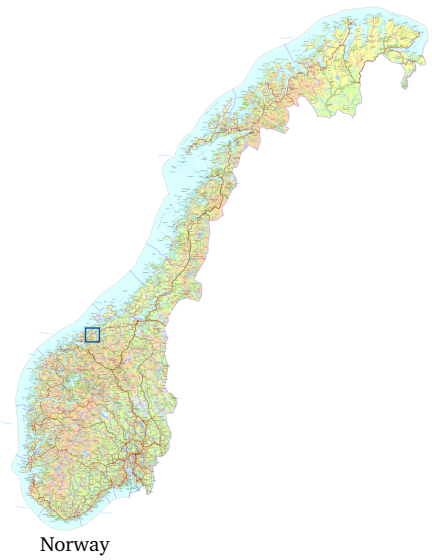

Fig. 2: Map section depicting the surrounding geography and location of the Bergsøysund Bridge. Map sections: © Kartverket.

were used. As to the author's knowledge, operational modal analysis has not been systematically applied to data from floating bridges, prior to the work presented in the current study.

1.2 Objectives and limitations

The objectives of the thesis can be summarized as follows:

- To study and quantify the uncertainty of the dynamic response of floating bridges subjected to wave excitation
- To apply, and compare the accuracy of, state-of-the-art operational modal analysis methods on a floating bridge case study
- To contribute to a better understanding of the dynamic behaviour of floating bridges

Nonlinearities and wind excitation are topics not directly treated herein.

1.3 Structure of the thesis

Chapters 2 and 3 present theory and results that are either very important to the problem or to supplement the content of the appended papers. Chapter 4 reviews the contributions and main findings in the appended papers, and some summarizing conclusions are given in Chapter 5. Thereafter, the appended papers, consisting of three published journal papers, one conference paper, and one submitted manuscript, follow. The papers represent the main work of the PhD study. The study may be sub-divided into the following three topics:

1. Numerical predictions (paper 1 and 5)
2. Measurement of real-life behaviour (paper 2 and 3)
3. Predictions versus measurements (paper 3 and 4)

2 | Floating bridge dynamics

To describe and simulate the dynamic behaviour of a floating bridge, a numerical simulation framework must be established. The hydrodynamics, describing both the wave excitation and the fluid-structure interaction have to be considered. The dynamics of the elastic structure are modelled by relying on a finite element method (FEM) framework, and in turn combined with the hydrodynamics. The random nature of the excitation makes a stochastic approach fundamental. These aspects are described in the current chapter.

2.1 Water waves and fluid-structure interaction

The appropriate selection of relevant wave forces acting on a structure is a choice that is highly dependent on the shape and size of the bodies interacting with the water. The following main forces are acting on a wave-exposed structure [30, 31]:

- *Froude-Krylov force* from the incident waves
- *Diffraction force* from the disturbance of the wave field due to the body
- *Radiation force* from the generation of radiating waves, due to the relative motion of the body
- *Viscous force* from the pressure drops resulting from flow separation around the body; also a consequence of the relative motion of the body

For slender bodies, the viscous drag force is more important than the radiation forces, and vice versa for bulky bodies. Because the size of the pontoons on the case study structure is relatively large compared to the relevant wave lengths, the viscous drag force is not considered in the current study.

The following is mainly based on Newman [32]. Other relevant sources on this subject are, e.g., [30, 33, 34].

A regular wave is a single sine wave, or *monochromatic* wave, and is the basis for more complex waves, through the superposition principle and Fourier analysis. The regular and plane wave is assumed to be expressed mathematically as follows:

$$\eta(x', t) = a\cos(\kappa x' - \omega t + \epsilon) \tag{1}$$

where η is the sea surface elevation function; x' is the distance along the wave direction, as depicted in Figure 3; t is the time; a is the amplitude of the wave; κ is the angular wavenumber,

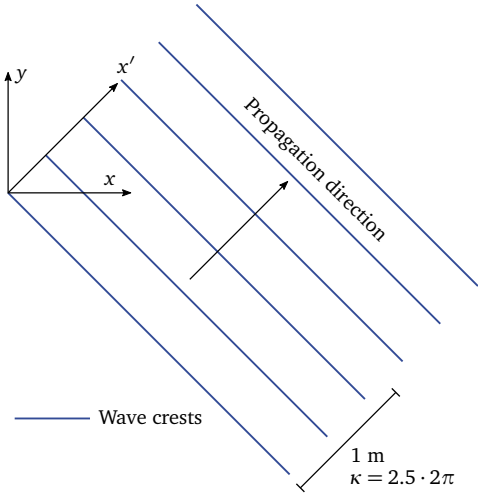

Fig. 3: Regular wave along axis x'.

defined as radians per unit distance; ω is the circular frequency; and ϵ is a random phase shift, which also indicate that any sinusoidal function may be used.

A flow is irrotational if the following holds true everywhere in the fluid:

$$\nabla \times \mathbf{v} = \mathbf{0} \tag{2}$$

where $\mathbf{v}$ is the fluid velocity; and ∇ is the del operator, which is defined in Cartesian coordinates (x, y, z) as follows:

$$\nabla \equiv \left[\frac{\partial}{\partial x}, \frac{\partial}{\partial y}, \frac{\partial}{\partial z} \right] \tag{3}$$

Here, x and y are describing the position in the horizontal plane and z is the vertical position. One big advantage of modelling a fluid as irrotational is that its velocity can be defined mathematically by means of a scalar velocity potential ϕ, as follows:

$$\mathbf{v} = \nabla \phi \tag{4}$$

By assuming that the fluid is incompressible, the conservation of mass can be expressed as follows, i.e., by the *continuity equation*:

$$\nabla \cdot \mathbf{v} = 0 \tag{5}$$

When Equations 4 and 5 are combined, Laplace's equation is obtained:

$$\nabla^2 \phi \equiv \frac{\partial^2 \phi}{\partial x^2} + \frac{\partial^2 \phi}{\partial y^2} + \frac{\partial^2 \phi}{\partial z^2} = 0 \tag{6}$$

This is the main differential equation describing all potential flows. For ϕ to describe specific situations, boundary conditions have to be imposed. For a floating body, the total velocity potential may be decomposed into three contributions:

$$\phi = \phi_w + \phi_d + \phi_r \tag{7}$$

where the three terms are described as follows:

- ϕ_w is the contribution from the undisturbed incident wave
- ϕ_d is the contribution from the diffraction of the incident wave, caused by the body
- ϕ_r is the contribution from the motion of the body, which produces radiating waves that originate from the body, and may be described as the sum of contributions from all six rigid degrees of freedom: $\phi_r = \sum_{j=1}^{6} \phi_{r,j}$

Thus, for a fixed body, the last term vanishes. Also, this decomposition implies that the radiation term may be considered to be a separate problem, i.e., the problem can be considered as a fixed body subject to incident waves plus a moving body in still water.

2.1.1 Boundary conditions

A kinematic boundary condition (KBC) may be specified from the fact that all particles on the free surface stays on the free surface. Mathematically, this reads out as follows:

$$\frac{D}{Dt}(z-\eta)\Big|_{z=\eta} = \left(\frac{\partial\phi}{\partial z} - \frac{\partial\eta}{\partial t} - \frac{\partial\phi}{\partial x}\frac{\partial\eta}{\partial x} - \frac{\partial\phi}{\partial y}\frac{\partial\eta}{\partial y}\right)\Big|_{z=\eta} = 0 \tag{8}$$

where $\frac{D}{Dt}$ is the *substantial derivative*.

Furthermore, the pressure is assumed atmospheric ($p = p_{\text{atm}}$) everywhere on the surface $z = \eta$. This forms the dynamic boundary condition (DBC) from Bernoulli's equation, as follows:

$$\eta = -\frac{1}{g}\left(\frac{\partial\phi}{\partial t} + \frac{1}{2}\nabla\phi\cdot\nabla\phi\right) \tag{9}$$

where g is the acceleration of gravity. Equations 8 and 9 form the total *free-surface boundary condition*.

The bottom of the seabed is also providing a boundary condition, from the fact that it cannot be penetrated, as follows:

$$\frac{\partial\phi}{\partial z}\Big|_{z=-d} = 0 \tag{10}$$

Here, d is the depth of the water. This implies that the potential is constant along the bottom, and thus, that it will not cause any flow across the seabed.

An impenetrability boundary condition is also required for the floating body:

$$\frac{\partial\phi}{\partial n} = \mathbf{v}, \quad \text{on } S_b \tag{11}$$

where S_b is the wetted surface of the floating body, the directional derivative $\frac{\partial\phi}{\partial n}$ is equivalent to $\nabla\phi\cdot\mathbf{n}$, and $\mathbf{n} = \mathbf{n}(x,y,z)$ is the normal vector field corresponding to the surface. If the diffraction problem is to be considered separately, the velocity potential $\phi_w + \phi_d$ may be solved for $\mathbf{v} = \mathbf{0}$ on S_b, i.e., with the body being fixed, and the radiation problem solved afterwards, by assuming still water.

It is reasonable to assume that the potential contributions are harmonic functions, due to the harmonic nature of the sought-after wave elevation and body motion, which implies:

$$\phi_{r,j}(x,y,z,t) = \text{Re}\left[a_j\hat{\phi}_{r,j}(x,y,z)\text{e}^{i\omega t}\right] \tag{12}$$

$$\phi_w(x,y,z,t) + \phi_d(x,y,z,t) = \text{Re}\left[A[\hat{\phi}_w(x,y,z) + \hat{\phi}_d(x,y,z)]\text{e}^{i\omega t}\right] \tag{13}$$

Thus, the following is obtained:

$$\phi(x,y,z,t) = \mathrm{Re}\left[\left(\sum_{j=1}^{6} a_j \hat{\phi}_{r,j}(x,y,z) + A[\hat{\phi}_w(x,y,z) + \hat{\phi}_d(x,y,z)]\right) e^{i\omega t}\right] \tag{14}$$

Still, the boundary problem is not unique, and a radiation condition at infinity is required. The radiation potential is assumed to give waves far away due to the motion of the body, which must be on the following form:

$$\phi_{r,j} \propto \mathrm{Re}\left[a_j(x^2+y^2)\exp(-i\kappa\sqrt{x^2+y^2})\right], \quad \text{for } x^2+y^2 \to \infty \tag{15}$$

2.1.2 Linearized boundary conditions

When the wave height η is small, the free-surface boundary conditions simplify drastically:

- Free-surface KBC (linearization of Equation 8): $\frac{\partial \eta}{\partial t} = \frac{\partial \phi}{\partial z}$
- Free-surface DBC (linearization of Equation 9): $\eta = -\frac{1}{g}\frac{\partial \phi}{\partial t}$

To study the effect of the nonlinearities, the potential function can be expanded as a Taylor series, about the plane $z = 0$, as follows:

$$\phi(x,y,\eta,t) = \phi(x,y,0,t) + \eta\left(\frac{\partial \phi}{\partial z}\right)_{z=0} + \frac{1}{2}\eta^2\left(\frac{\partial^2 \phi}{\partial z^2}\right)_{z=0} + \ldots \tag{16}$$

By retaining the second order term, two important implications follow. Firstly, the excitation will include a mean drift force, which is a result of the net mass transport of water past the pontoon. Secondly, the excitation frequency components will also include sums and differences of the frequency components present in the sea surface elevation.

2.1.3 Panel methods

The potentials ϕ_d and ϕ_r are both dependent on the surface of the body. Except for very simple geometries, it is not feasible to obtain the potentials analytically. Therefore, *panel methods* represent a very useful tool to enable such calculations for almost any reasonable surface. Panel methods may therefore represent complex flow situations from the superposition of known solutions to simple potential flows.

2.1.4 Hydrodynamic forces

By retaining only the linear terms in Bernoulli's equation, the following equation is obtained for the pressure p:

$$p = -\rho\left(\frac{\partial \phi}{\partial t} + gz\right) \tag{17}$$

where ρ is the mass density of the water. The sum of all external forces and moments (3 forces and 3 moments) acting on the floating body may therefore be written as:

$$\begin{aligned}\{p_h\}(t) = &\underbrace{-\rho g \int_{S_b} \begin{Bmatrix} \mathbf{n} \\ \mathbf{r}\times\mathbf{n} \end{Bmatrix} z dS}_{\text{hydrostatic forces}} + \underbrace{\begin{Bmatrix} \mathbf{F}_G \\ \mathbf{F}_G \times \mathbf{r}_G \end{Bmatrix}}_{\text{gravitational forces}} \\ &\underbrace{-\rho \mathrm{Re}\left[\sum_{j=1}^{6} i\omega a_j e^{i\omega t} \int_{S_b} \begin{Bmatrix} \mathbf{n} \\ \mathbf{r}\times\mathbf{n} \end{Bmatrix} \phi_j dS\right]}_{\text{added mass and damping}} \\ &\underbrace{-\rho \mathrm{Re}\left[i\omega A e^{i\omega t} \int_{S_b} \begin{Bmatrix} \mathbf{n} \\ \mathbf{r}\times\mathbf{n} \end{Bmatrix} (\phi_w + \phi_d) dS\right]}_{\text{wave excitation}}\end{aligned} \tag{18}$$

where $\mathbf{n}$ is the normal vector on the surface of the body, with positive direction inwards; $\mathbf{r}$ is the position vector to the surface; $\mathbf{F}_G = [0, 0, -mg]$ is the gravitational force of the body with mass m; and $\mathbf{r}_G$ is the position vector to the centre of gravity (CG) of the body.

The first and second terms correspond to the hydrostatic component, and the forces and moments due to the weight of the floating body, respectively. Together, they form the total static forces. By only retaining the terms that are dependent on the displacement of the floating body, the stiffness coefficients may be established as follows, for a body in its equilibrium position [32]:

$$K_{33} = \rho g S \tag{19}$$
$$K_{44} = \rho g V \Delta h_1 \tag{20}$$
$$K_{55} = \rho g V \Delta h_2 \tag{21}$$

where V is the displaced volume, S is the waterplane area, and ρV equals the mass of the body m. Finally, $\Delta h_i = z_{M,i} - z_G$ is introduced as the *metacentric height* corresponding to stability along axis i, where $z_{M,i}$ is the corresponding *metacentre*, and z_G is the vertical coordinate of the CG. The metacentre can furthermore be written as follows:

$$z_{M,i} = I_{ii}/V + z_B, \quad i = 1, 2 \tag{22}$$

where z_B is the vertical location of the centre of buoyancy; and I_{ii} is the *waterplane moment*, analogous to the first area moment, defined as $I_{ii} = \int\int_{S_0} x_i^2 dS$ and S_0 is the waterplane area in the static condition. The concept of metacentric height and hydrostatic stability is illustrated in Figure 4.

The third term in Equation 18 is originating from the radiation potential, and results in complex values, which implies both mass and damping contributions.

Finally, the fourth term describes the wave excitation resulting from the incident wave and the diffraction effects caused by the body.

The total hydrodynamic excitation in Equation 18, due to a small monochromatic wave proportional to $e^{i\omega t}$, can be written as follows:

$$\{p_h(t)\} = \{P(\omega)\}e^{i\omega t} - [M_h(\omega)]\{\ddot{u}(t)\} - [C_h(\omega)]\{\dot{u}(t)\} - [K_h]\{u(t)\} \tag{23}$$

where $[M_h(\omega)]$, $[C_h(\omega)]$ and $[K_h]$ are the added hydrodynamic mass, potential hydrodynamic damping and restoring stiffness, respectively; and $\{P(\omega)\}$ is the frequency domain wave excitation. No further attention is devoted to the description of the forces, as the topic is well described in text books (e.g. [32]).

A note on stability and restoring forces

The hydrostatic term in Equation 18 is expressing the buoyancy forces acting on the body. Together with the gravitational force of the body, the hydrostatic forces give rise to restoring forces and moments to restore the body to its equilibrium position. By assuming small displacements and rotations, this is interpreted as a stiffness contribution to the FE model. The reasoning behind the restoring roll moment due to a small angle of a free-floating pontoon is illustrated in Figure 4a. Note that by adding a superstructure on top of the pontoon, the centre of gravity is shifted, and thus, the restoring moment affected (Figure 4b). Also, the gravitational and buoyancy forces, which are equal, are increased. The weight of the structure resting on top of the pontoons must therefore be considered to establish the appropriate rotational hydrostatic stiffness contributions. When the metacentre, denoted M in Figure 4b, is located above the gravitational centre, the body is considered stable, and will return to its original equilibrium position. When the metacentre is located below, however, the body is unstable, which implies that it has a negative stiffness contribution to the system.

2.2 Stochastic water waves

The sea surface elevation is a scalar function of position $\{r\}$ and time t, and may be expressed as follows [30, 35]:

$$\eta(\{r\},t) = \int_{\kappa_x,\kappa_y,\omega} \mathrm{e}^{i\{\kappa\}\cdot\{r\}-i\omega t} dZ_\eta(\{\kappa\},\omega) \tag{24}$$

where Z_η denotes the spectral process that describes the sea surface elevation and $\{\kappa\}$ is the wave number vector, the two-dimensional extension of the wave number, which is defined as follows:

$$\{\kappa\} = \begin{Bmatrix}\kappa_x\\ \kappa_y\end{Bmatrix} = \kappa \begin{Bmatrix}\cos\theta\\ \sin\theta\end{Bmatrix} \tag{25}$$

Here, θ is defined as the angle relative to the global x-axis. For wave fields assumed to be stationary and homogeneous, the spectral process of the sea surface elevation is related to the cross-spectral density as follows:

$$E\left(dZ_{\eta_p}(\{\kappa\},\omega) dZ_{\eta_q}(\{\kappa\},\omega)^*\right) = S_{\eta_p,\eta_q}(\{\kappa\},\omega) d\kappa_x d\kappa_y d\omega \tag{26}$$

where the indices p and q denote two arbitrary points on the xy-plane, $S_{\eta_p,\eta_q}(\{\kappa\},\omega)$ is the 3D cross-spectral density corresponding to the wave elevations at the two points, * is the complex conjugation operator, and the expectation operator is denoted $E(\cdot)$. In linear wave theory, the *dispersion relation* specifies the relation between wave number and frequency, as follows:

$$\omega^2 = g\kappa \tanh(\kappa d) \tag{27}$$

where d is the water depth. For $d \to \infty$, i.e., deep water, this reduces to:

$$\omega^2 = g\kappa \tag{28}$$

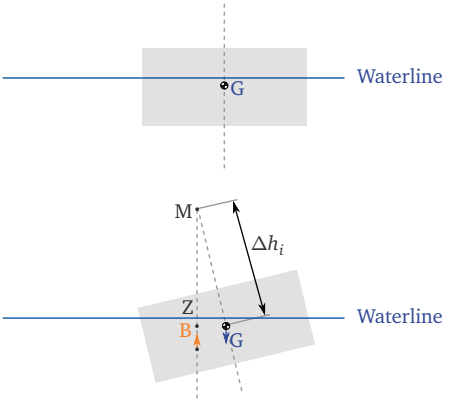

(a) Without superstructure.

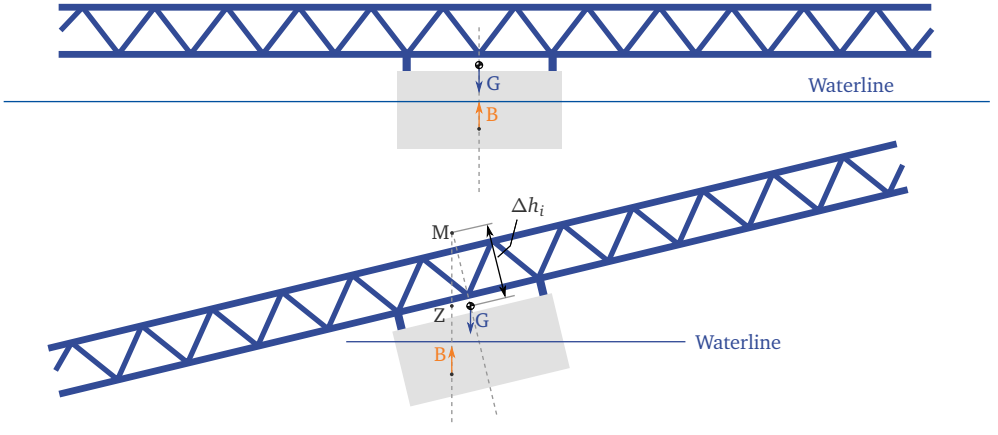

(b) With superstructure. The addition of the superstructure raises the centre of gravity such that the restoring arm, and thus, the restoring moment is reduced.

Fig. 4: Stability of a floating pontoon. G is the gravitational force acting from the CG, M denotes metacentre, Z is the point along the vertical line from the buoyancy force B on the same vertical level as the CG.

The dispersion relation makes it possible to express the two components of the wave number vector with frequency and angle. Thus, the three-dimensional cross-spectral density can be expressed as a two-dimensional cross-spectral density, as follows:

$$E\left(dZ_{\eta_p}(\theta,\omega)dZ_{\eta_q}(\theta,\omega)^*\right) = S_{\eta_p,\eta_q}(\theta,\omega)d\theta d\omega \tag{29}$$

The power spectral density at a single point ($p = q$) then becomes:

$$S_\eta(\omega,\theta) = S_{\eta_p,\eta_p}(\omega,\theta) = S_{\eta_q,\eta_q}(\omega,\theta) \tag{30}$$

which is decomposed into one-dimensional wave spectral density $S_\eta(\omega)$ and directional distribution $D(\omega,\theta)$, as follows:

$$S_\eta(\omega,\theta) = S_\eta(\omega)D(\omega,\theta) \tag{31}$$

This is constructed such that $\int_0^{2\pi} D(\omega,\theta)d\theta = 1$ for all ω. The vector distance between points p and q is denoted as $\{\Delta r\}$, such that the cross-spectral density between the wave elevation at points p and q may be given as:

$$S_{\eta_p,\eta_q}(\omega) = \int_0^{2\pi} S_\eta(\omega)D(\omega,\theta)\mathrm{e}^{i\{\kappa\}\cdot\{\Delta r\}}d\theta \tag{32}$$

The hydrodynamic transfer function $\{q_p(\omega,\theta)\}$, which is directly related to the fourth term in Equation 18, gives 3 forces and 3 moments from the wave elevation, for the floating body located on point p. This is mathematically expressed as follows:

$$\{dZ_{p_p}(\omega,\theta)\} = \{q_p(\omega,\theta)\}dZ_{\eta_p}(\omega,\theta) \tag{33}$$

This gives the following cross-spectral density matrix corresponding to the wave excitation:

$$[S_{p_p,p_q}(\omega)] = \int_0^{2\pi} \{q_p(\omega,\theta)\}S_{\eta_p,\eta_q}(\omega,\theta)\{q_q(\omega,\theta)\}^{*T}d\theta \tag{34}$$

where ^{T} is the matrix transpose operator. This results in a 6×6 large matrix for each combination of p and q. The global wave excitation cross-spectral density matrix may thereafter be constructed by arranging these matrices as submatrices in a $(6N)\times(6N)$ large matrix, where N is the number of floating bodies.

2.3 Numerical model set-up

The model of a floating structure can be set up within a FEM framework, as follows:

$$[M_s]\{\ddot{u}(t)\} + [C_s]\{\dot{u}(t)\} + [K_s]\{u(t)\} = \{p_h(t)\} \tag{35}$$

where $[M_s]$, $[C_s]$, and $[K_s]$ are the structure's mass, damping and stiffness matrices, respectively; $\{u(t)\}$ is the displacement vector describing the displacements for all degrees of freedom (DOFs), and is a function of time t; $\{p_h(t)\}$ is the total hydrodynamic action, which is the total force acting on the structure, including both the wave excitation and the fluid-structure interaction; and the dot notation indicates time differentiation. The total hydrodynamic action can be expressed as follows:

$$\{p_h(t)\} = -\left(\int_{-\infty}^{\infty} [m_h(t-\tau)]\{\ddot{u}(\tau)\} + [c_h(t-\tau)]\{\dot{u}(\tau)\}d\tau + [K_h]\{u(t)\}\right) + \{p(t)\} \tag{36}$$

where $[K_h]$ is the stiffness contribution resulting from the gravitational and buoyancy forces of the floating part, cf. term one and two in Equation 18; $[m_h(t)]$ and $[c_h(t)]$ are the time-domain descriptions of the added hydrodynamic mass and added hydrodynamic damping, which is a consequence of the fluid-structure interaction between the floating pontoons and the water, cf. term three in Equation 18; and $\{p(t)\}$ is the wave excitation, cf. term four in Equation 18. By

using the following convolution integral notation: $f * h = \int_{-\infty}^{\infty} f(t-\tau)h(\tau)d\tau$, Equations 35 and 36 may be combined to yield the following equation of motion:

$$[M_s]\{\ddot{u}(t)\} + [m_h(t)] * \{\ddot{u}(t)\} + [C_s]\{\dot{u}(t)\} + [c_h(t)] * \{\dot{u}(t)\} + ([K_s] + [K_h])\{u(t)\} = \{p(t)\} \quad (37)$$

From the fact that convolution in the time domain is equivalent to multiplication in the frequency domain, the following simple frequency domain expression is established:

$$[M(\omega)]\{d\ddot{Z}_u(\omega)\} + [C(\omega)]\{d\dot{Z}_u(\omega)\} + [K]\{dZ_u(\omega)\} = \{dZ_p(\omega)\} \quad (38)$$

$$\left(-\omega^2[M(\omega)] + i\omega[C(\omega)] + [K]\right)\{dZ_u(\omega)\} = \{dZ_p(\omega)\} \quad (39)$$

where $\{Z_u(\omega)\}$ is the spectral process corresponding to the displacement, $\{Z_p(\omega)\}$ is the spectral process corresponding to the wave excitation, $\{d\dot{Z}_u(\omega)\} = i\omega\{dZ_u(\omega)\}$, and the following full frequency-domain system matrices are introduced:

$$[M(\omega)] = [M_s] + [M_h(\omega)] \quad (40)$$

$$[C(\omega)] = [C_s] + [C_h(\omega)] \quad (41)$$

$$[K] = [K_s] + [K_h] \quad (42)$$

Note that $[m_h(t)]$ and $[c_h(t)]$ simply are the Fourier transforms of $[M(\omega)]$ and $[C(\omega)]$, respectively.

2.3.1 Sub-structuring of problem

In the current study, a slight modification of the approach given above is made. The total system matrices are obtained from division into two sub-structures: (i) an FEM model including all the structural components, inertia of the pontoons and the stiffness contribution from the buoyancy and self-weight of the pontoons; and (ii) a hydrodynamic model providing the added mass and added damping. The first sub-structure is used to construct a modal space, such that the number of DOFs are reduced, and to avoid using all the free DOFs of the FEM model. The mode shapes are defined by the displacements and rotations at the pontoon locations. Then, the contributions from the second sub-structure are transformed to the modal space given by these mode shapes. It is important to realize that this therefore cannot be considered a true *modal* transformation, but rather a convenient change of coordinate basis: the matrices will not become diagonal. This approach is thoroughly described in the first appended paper [36].

2.4 Modal analysis

There are two important special characteristics of this type of problem:

1. The arc-shape of the bridge gives mode shapes with both vertical and horizontal components.

2. The large, non-classical, damping contributions resulting from the fluid-structure interaction results in complex modes. This implies that the maximum displacement of the DOFs included in a mode is not reaching their maximum at the same instance, but rather with relative phase shifts to each other.

Furthermore, as an effect of the coordinate basis transformation, represented by the mode shapes resulting from the first sub-structure, the final eigenvalue problem can be considered as a two-step procedure as follows:

$$\{u\} = [\Phi]\{y\} \tag{43}$$
$$\{y\} = [\Psi]\{g\} \tag{44}$$

where $\{u\}$ represents the chosen physical DOFs, $[\Phi]$ is the modal transformation matrix related to the first substructure only and $\{y\}$ represents the corresponding generalized coordinates, $[\Psi]$ is the modal transformation matrix resulting from the eigenvalue solution of the reduced problem and $\{g\}$ the corresponding generalized coordinates. A column in $[\Psi]$, i.e., a mode shape, is therefore in practice describing a weighted combination of various mode shapes originating from the first sub-structure. This implies the following:

$$\{u\} = [\Phi][\Psi]\{g\} \tag{45}$$
$$\{u\} = [\Gamma]\{g\} \tag{46}$$

As seen here, the full modal transformation matrix, representing the mode shapes of the structure, can be obtained through: $[\Gamma] = [\Phi][\Psi]$.

2.5 Response prediction

The procedure highlighted above presents a way to establish the frequency-dependent system matrices, and from this the frequency domain transfer function, which relate the force exerted to the system with the response that follows.

When the assumption of linearity is reasonable, as for the prediction of the response in the serviceability state, a frequency domain approach stands out as the best approach due to its efficiency combined with better interpretability. However, for harsher conditions, as for response prediction in the ultimate state, the nonlinearities may render the linear frequency domain approach unsuitable. Therefore, such situations call for a time-domain approach. Both are described in the following.

2.5.1 Frequency-domain solution: the power spectral density method

The equation of motion given in Equation 38 may be reformulated with the frequency domain transfer function, as follows:

$$\{dZ_u(\omega)\} = [H(\omega)]\{dZ_p(\omega)\} \tag{47}$$

The following definitions of spectral densities are introduced:

$$[S_u(\omega)]d\omega = E\left(\{dZ_u(\omega)\}\{dZ_u(\omega)\}^{*T}\right) \tag{48}$$
$$[S_p(\omega)]d\omega = E\left(\{dZ_p(\omega)\}\{dZ_p(\omega)\}^{*T}\right) \tag{49}$$

Equations 47–49 are combined to give the equation representing the *power spectral density method*, as follows:

$$[S_u(\omega)] = [H(\omega)][S_p(\omega)][H(\omega)]^{*T} \tag{50}$$

Handling nonlinearities

The *Kryloff-Bogoliuboff method* [37] and the *perturbation technique* [38] are two well-known linearization approaches, that may reduce the errors caused by handling the nonlinear problem as a linear one. The Kryloff-Bogoliuboff method is based on introducing and minimizing an error term on the right-hand side of the equation of motion, which is the error from the linearization. Furthermore, by assuming that the nonlinearities originating from the damping and the stiffness forces are independent and additive, coefficients representing the linearized system may be determined. The result is that the nonlinear system and the equivalent linearized system have the same work per cycle [39]. The perturbation technique is based on separating the response into linear and nonlinear contributions of increasing order, and similarly splitting the equation of motion into multiple equations. In effect, this results in more terms being introduced in Equation 50. When the nonlinear effects are severe, the linearization methods will not provide sufficient accuracy.

Certain nonlinearities may be handled in a bi-spectral analysis [40], using Volterra-series. General nonlinearities, however, should be treated directly in a full nonlinear time-domain simulation approach.

It is referred to the cited literature for more details.

2.5.2 Time-domain solution: Monte Carlo simulation

The equation of motion given in Equation 37 represents a direct simulation approach for the response, given a specified time history of the wave excitation. The numerical solution of the convolution integral is very demanding computationally. In practice, the convolution integrals are often avoided. The alternative approaches to accomplish this are reviewed in [41]. To represent the stochastic nature of the excitation, samples from its spectral density is drawn based on a specified random selection scheme, and multiple simulations are run. All the resulting response time histories are thereafter averaged, which forms a stochastic description of the response. This procedure is referred to as *Monte Carlo simulation* [42]. No further details are given about this topic herein, and it is referred to the cited paper. Time simulation from amplitude sampling is also discussed in the fifth appended paper [43].

3 | Structural monitoring

3.1 Monitoring system

A comprehensive monitoring system was installed on the Bergsøysund Bridge, such that valuable data on its behaviour could be obtained. The layout of the sensor network is depicted in Figure 5 and the data transfer and synchronization set-up illustrated in Figure 6. Digital sensors connected to logger nodes are communicating through Wi-Fi with a main logger unit. Synchronization of the data retrieved from all the digital sensors is achieved by acquiring time stamps from Global Positioning System (GPS) sensors. The monitoring system consists of 14 (2×7) triaxial accelerometers, five anemometers, six wave radars and one Global Navigation Satellite System (GNSS) sensor for displacement measurement. The monitoring system is described in detail in the second appended paper [44].

3.1.1 Time integration of accelerations

Time integration from accelerations to displacements may be performed in the frequency domain, when assuming zero-mean motion, as follows:

$$\{u(t)\} = \mathscr{F}^{-1}\left[(i\omega)^{-2}\mathscr{F}\left(\{\ddot{u}(t)\}\right)\right] \tag{51}$$

Here, $\mathscr{F}(\cdot)$ is the Fourier transform and $\mathscr{F}^{-1}(\cdot)$ is the inverse Fourier transform. Numerically, these transformations are efficiently performed by applying the fast Fourier transform (FFT). To avoid false drift originating from low-frequency noise, a high-pass filter should be applied. The resulting displacements obtained from transforming and integrating the accelerations of the midmost pontoon are compared with the displacements recorded by the GNSS sensor in Figure 7. The data shown is obtained from the recording with the largest significant wave height and displacement observed in the survey to date. The figure is supplementing a similar comparison in the frequency domain, i.e., with spectral densities, that was conducted in the second appended paper. A very good agreement is observed for the lateral component. Longitudinal motion is not accurately described, due to the low amplitude. Furthermore, the agreement between the vertical displacements is suffering, probably due to the known issues regarding the vertical accuracy of the GNSS technology.

3.1.2 Reconfiguration of the wave radar layout

Based on the findings in the fifth appended paper [43], a modification of the original wave radar layout shown in Figure 5 was made. The layout changes are indicated in Figure 8. To fully characterize the sea state, under the assumption of homogeneity, the two-dimensional

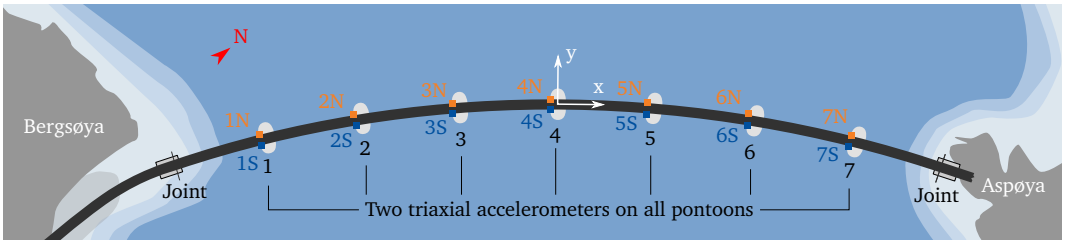

(a) Top view.

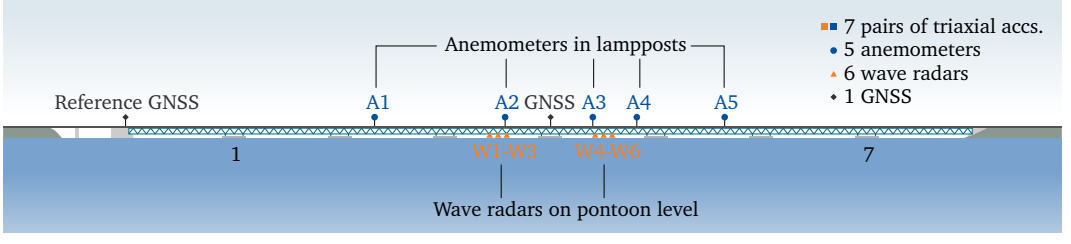

(b) Side view.

Fig. 5: Monitoring system. Reproduced from [44] with permission from Elsevier.

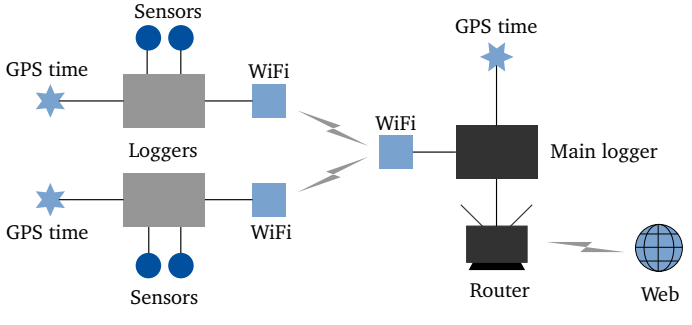

Fig. 6: Communication and structure of monitoring system. Reproduced from [44] with permission from Elsevier.

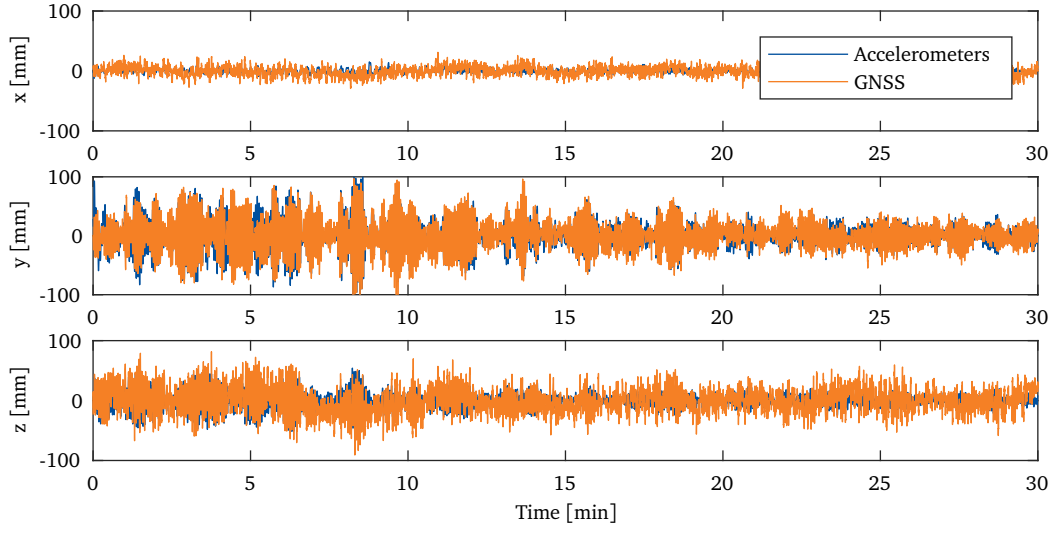

(a) Full 30-minute recording.

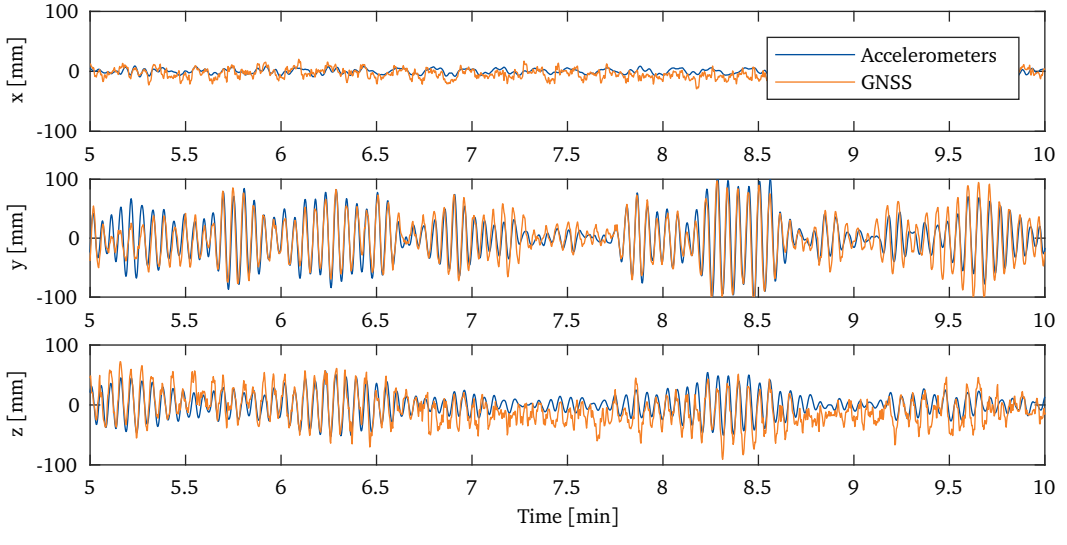

(b) Selected time segment.

Fig. 7: Comparison between recorded displacements from GNSS sensor and numerically integrated accelerations from accelerometers on the midmost pontoon.

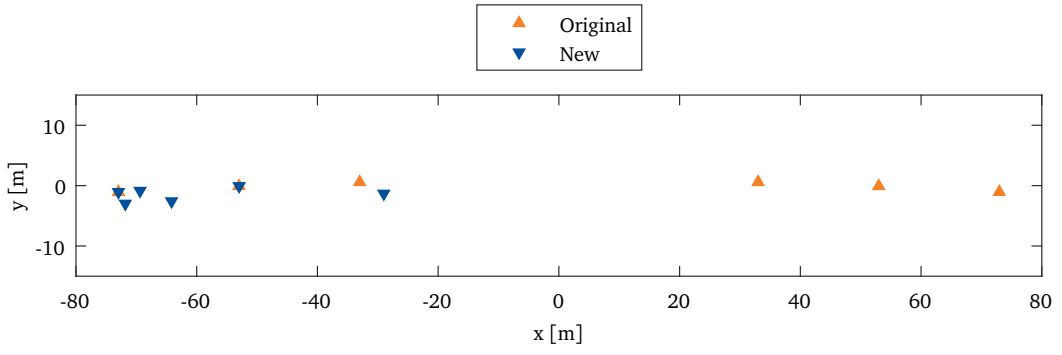

Fig. 8: Original and new configuration of the wave radar layout.

wave spectral density is sufficient, cf. Equation 31. Based on a defined reference sea state, time simulation of the wave elevation at the locations of the wave radars was performed. The defined sea state was set to a low excitation level ($H_s = 0.3m$) and was otherwise specified with realistic values for both the directional distribution ($\cos^{2s}$ with $s = 17$ and head sea, i.e., with a mean wave direction hitting the structure laterally) and the one-dimensional wave spectral density (JONSWAP spectrum with $\gamma = 2.5$ and $T_p = 3s$). To assess the sensor layout, the two-dimensional wave spectral density was estimated from the time simulations by applying the implementation of the enhanced maximum entropy principle (EMEP) found in the DIWASP toolbox [45] for MATLAB. The resulting two-dimensional wave spectral densities are shown in Figure 9 for both the original and updated sensor layout, together with the reference spectral density (Figure 9a). It is apparent that the layout modification theoretically enables the characterization of relevant sea states. More details about the simulation procedure and modelling approach is given in the appended paper.

3.2 Operational modal analysis

Traditionally, dynamic testing relies on the estimation of terms in the frequency response function matrix, which requires measurement of both excitation forces and selected response quantities. For operating structures, such as bridges exposed to both traffic loads and environmental action, this is not always practically viable. Therefore, modal analysis based on ambient vibrations, often referred to as operational modal analysis, provides the most cost-efficient and convenient basis for modal testing. In the current study, operational modal analysis is used to estimate the modal properties of the Bergsøysund Bridge. Self-implemented code for the algorithms covariance-driven stochastic subspace identification (Cov-SSI), data-driven stochastic subspace identification (Data-SSI) and frequency domain decomposition (FDD), are used to estimate the modal parameters of the bridge. More details on this is provided in the third appended paper [46].

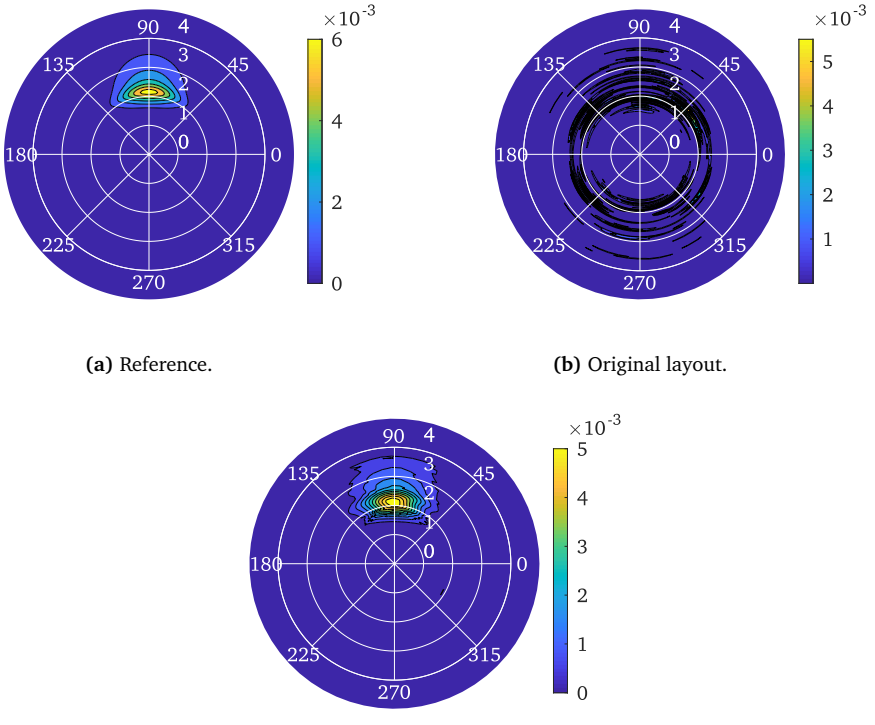

(a) Reference.

(b) Original layout.

(c) New layout.

Fig. 9: 2D wave spectral densities.

4 | Summary of appended papers

Paper 1: Simulation of stochastic behaviour

K. A. Kvåle, R. Sigbjörnsson, and O. Øiseth, "Modelling the stochastic dynamic behaviour of a pontoon bridge: A case study", Computers & Structures, vol. 165, pp. 123–135, Mar. 2016.

This paper presents a comprehensive model set-up for pontoon bridges, with the Bergsøysund Bridge as a case study example. The numerical model set-up is based on a finite element model of the structural components, which is combined with hydrodynamic models of the pontoons. By using a state-space representation, the complex eigenvalue problem is solved. The frequency dependency from the fluid-structure interaction contributions, that in turn results in a quadratic eigenvalue problem, is overcome by iteration. The paper investigates the effects the spreading of the waves and the significant wave height have on the resulting response, by parameter studies. It is concluded that the effect of wave spreading is very small, and that it in practical cases can be disregarded. A two-dimensional map of the sea surface correlation in space is presented for various sea states, which proves to be a useful tool in the interpretation of the excitation situation. For the case study, it is concluded that realistic sea states are not able to excite the pontoons in a correlated manner, which implies that a block-diagonal spectral density matrix representing the load excitation is sufficient. Finally, the paper presents and discusses the results obtained by approximating the frequency-dependent coefficients to be constant. The best agreement with the full model is found when using the values of the frequency-dependent matrices at the weighted frequency of the maximum of the response spectral densities.

Paper 2: Structural monitoring

K. A. Kvåle and O. Øiseth, "Structural monitoring of an end-supported pontoon bridge", Marine Structures, vol. 52, pp. 188–207, Mar. 2017.

A comprehensive monitoring system is installed on the Bergsøysund Bridge, and is described in detail in this paper. The effects that the environmental parameters have on the response is investigated, and as expected, it is concluded that the significant wave height has the largest effect on the response. It is noted that the observed wave energy is normally located at frequencies above the frequencies of the first ten fundamental vibration modes of the structure. This is considered to be beneficial with regard to displacements and stress levels, but at the same time the response following such an excitation is much more difficult to predict accurately due to the high number of modes required. A distinct relation between significant wave height and acceleration is observed, as expected. Relatively large variability in the relation between mean

wind speed and significant wave height is also observed, which is explained by two factors: (i) the complexity of the surrounding geography and (ii) the large inertia in the wave process resulting in a slow energy transfer. The displacements recorded from a global navigation satellite system (GNSS) sensor are compared with the double time-integrated accelerations of the midmost pontoon, to assess the performance of the sensor. For large motion, the sensor performs good, in particular for the lateral displacements.

Paper 3: Operational modal analysis

K. A. Kvåle, O. Øiseth, and A. Rønnquist, "Operational modal analysis of an end-supported pontoon bridge", Engineering Structures, vol. 148, pp. 410–423, Oct. 2017.

In this paper, operational modal analysis methods are applied to acceleration recordings of the Bergsøysund Bridge, yielding estimates of natural frequencies, damping ratios and mode shapes. Frequency domain decomposition (FDD), data-driven stochastic subspace identification (Data-SSI) and covariance-driven stochastic subspace identification (Cov-SSI) are applied to the data, and the methods' capabilities to capture the modal parameters on the case study discussed. It is concluded that the Cov-SSI method gives the best results, also regarding robustness and speed. The resulting modal parameters are compared with those obtained from an updated version of the numerical prediction model. A very good agreement is found between the predicted and measured natural frequencies and mode shapes. However, the damping ratios deviate significantly. If the damping of all modes are considered under one, the damping levels may be considered to be near-consistent with the prediction. The large damping levels, the closely spaced modes and the arc-shaped design makes the overall motion patterns complicated, and thus the identification challenging. In agreement with the theoretical model, the fact that the mode shapes are complex-valued gives rise to a phase shift between the maximum displacements at the different degrees of freedom under consideration. The mode shapes obtained from the eigenvalue solution of the model are used as reference to enable an automatic extraction of modal parameters of several recordings, and the relationship between parameters characterizing the excitation and the modal parameters resulting from Cov-SSI analyses is studied. It is shown that increasing significant wave height results in a lower variability in the natural frequency estimates, and a larger mean damping.

Paper 4: Response prediction and comparison with measurements

K. A. Kvåle and O. Øiseth, "Dynamic response of an end-supported pontoon bridge due to wave excitation: numerical predictions versus measurements", Submitted for journal publication, 2017.

This paper combines the efforts in the first paper on the stochastic modelling and the second paper on the structural monitoring, to investigate the accuracy of the numerical response predictions. Firstly, response spectral densities predicted from a selected measured high-excitation case, was compared with the measured response. Secondly, by fitting JONSWAP spectra to the wave spectral densities of a large pool of recordings, the standard deviations resulting from predictions were compared globally with corresponding response measurements. In this way, coefficients of determination could be calculated for all the degrees of freedom, to evaluate the overall fit. Thirdly, linear functions were fitted to numerical probability density functions obtained from measurements, to describe how peak period and spectrum-peakedness relate to the significant

wave height. By doing so, it was possible to estimate the response merely by the significant wave height, which matched well with the mean of the predictions obtained when retaining all parameters. With all the approaches, it was shown that the lateral response is generally well estimated, whereas the vertical response is predicted in a decent manner. The torsional response is not predicted with a sufficient accuracy.

Paper 5: Characterizing the wave field from simulated sea surface elevation

K. A. Kvåle and O. Øiseth, "Characterization of the wave field around an existing end-supported pontoon bridge from simulated data", in Proceedings of the International Conference on Earthquake engineering and Structural Dynamics, Reykjavik, Iceland, 2017.

The wave excitation is one of the main concerns in regard to the dynamic analysis of floating bridges, and an appropriate sea state description is therefore an essential requirement. The monitoring system on the Bergsøysund Bridge, described in the second paper, involves the monitoring of the sea surface elevation at six single points by means of wave radars. The sensor layout of these wave radars is the topic under investigation in this paper. By conducting time simulation of the wave elevations at the six points of the wave radars, from a two-dimensional wave spectral density chosen to be a reference case, the simulated sea state is attempted to be identified. This is performed by applying the methods Fourier Expansion Method and Extended Maximum Entropy Principle. The latter method is shown to be superior in the identification of the reference sea state. More importantly, it is shown that the original wave radar layout is not appropriate for the identification of realistic sea states on site, and consequently, a new layout is suggested.

5 | Concluding remarks

In this doctoral dissertation, the behaviour of floating bridges has been studied through five papers. The main scientific contributions from the study can be summarized as follows:

- A database of recordings from the Bergsøysund Bridge monitoring program, eventually to be made openly available to other researchers
- Insight into the dynamic behaviour of the Bergsøysund Bridge, which to a variable extent may be extended to other floating bridges
- New experience on the application of operational modal analysis methods on floating bridge response data; including both the description of case-specific challenges, and how to overcome them

The main conclusions are listed more specifically in the following. Note that the conclusions are based on the case study on the Bergsøysund Bridge, and are not necessarily extendable to other floating bridges.

Directional spreading
The numerical prediction model is used to conduct parameter studies with varying directional spreading. The results indicate that for realistic excitation levels, the directional spreading of the waves is not affecting the resulting response significantly. This conclusion is valid for all the sea states considered.

Modal parameters
A state-space approach combined with iteration is effectively applied to solve for the modal parameters of the numerical model. Cov-SSI is successfully applied to the acceleration data to give the experimental modal parameters. The combination of closely spaced modes and large damping makes less sophisticated operational modal analysis methods unsuitable. The arc-shape of the bridge combined with the anisotropic stiffness contribution from the buoyancy, gives mode shapes including both vertical and horizontal component, which is observed both numerically and experimentally. The large damping contributions from the fluid-structure interaction yield vertical modes with critical damping ratios up to the range 12–14%, which is confirmed experimentally. It is observed that the mode shapes obtained experimentally are varying significantly from recording to recording. This is particularly valid for the modes with the largest damping ratios. Furthermore, to a variable extent, they are observed to mix with each other in different manners. This may indicate a coupling effect between these modes, i.e., that the modes are feeding each other with energy. Because the nonclassical damping contribution from the fluid-structure interaction gives

rise to complex-valued mode shapes, the displacements due to a vibration mode is not reaching their maximum at the same time instance, but are separated in time by phase shifts; something also observed experimentally.

Correlation of wave excitation
Due to the arc-shaped design combined with the relatively large distance between the pontoons, the pontoons are excited in a close-to uncorrelated manner when exposed to realistic excitation conditions. Therefore, the wave excitation spectral density matrix may in most cases be approximated to be block-diagonal, without any cross-terms describing the relation between the excitation of the different pontoons.

Wind-to-wave energy transfer
Results are indicating that wind and wave directions are differing significantly in some cases. High complexity of the geography surrounding the Bergsøysund Bridge and large inertia of the wind-generated waves are the main explanations for this observation.

Effects of increasing excitation level
The increase of significant wave height, characterizing the excitation level, results in a reduction of the variability in the identified natural frequencies. Furthermore, the mean values of the critical damping ratios are increased due to increased significant wave height.

Response predictions
The lateral, vertical and torsional response is considered the most critical. The numerical predictions of the response are shown to be reasonably accurate for the lateral motion. Vertical response is predicted adequately in most practical cases, when not considering the frequency content of the response, but rather merely the standard deviations. Response in rotation about the bridge's longitudinal axis, i.e., torsional response, is not predicted sufficiently accurate. The analyses performed with the full parameter sets yielded the following coefficients of determination for the standard deviations of lateral, vertical and torsional acceleration, respectively: $R^2 > 0.83$, $0.52 < R^2 < 0.77$, and $0.39 < R^2 < 0.62$; which supports the above conclusions.

Characterization of the wave field
The original wave radar layout, presented in the second appended paper, is not deemed suitable for characterizing the directional properties of the wave field. Consequently, they are moved, and the EMEP method is applied successfully to reconstruct a realistic reference sea state from the simulated time data of the sea surface elevations at six new locations.

The study demonstrates that floating bridges are prone to complex dynamic behaviour. The linear prediction model was able to predict the response level of the floating bridge under investigation rather accurately, when exposed to first-order wave excitation corresponding to the sea states measured during the monitoring survey. The detailed characteristics of the behaviour was shown to be accurately described only for the lateral motion.

5.1 Future work

The investigation of the following aspects is suggested as a continuation of the current study:

- An investigation of the errors observed between the measured and predicted torsional response
- The use of more sophisticated techniques for the automated operational modal analysis
- The application of input-based operational modal analysis to mitigate or reduce the potential influence from the non-white-noise wave excitation
- The characterization of the wave field from measured sea surface elevation

References

[1] E. Watanabe, "Floating bridges: past and present," *Structural Engineering International*, vol. 13, no. 2, pp. 128–132, 2003.

[2] O. Elleveset, "Project Overview Coastal Highway Route E39," 2012.

[3] B. Mukherji, *Dynamic behavior of a continuous floating bridge*. Doctoral dissertation, University of Washington, 1972.

[4] B. J. Hartz and B. Mukherji, "Dynamic response of a floating bridge to wave forces," in *Proc. International Conference on Bridging Rion-Antirion. Patras, Greece*, 1977.

[5] B. J. Hartz, "Dynamic Response of the Hood-Canal Floating Bridge," in *Second ASCE/EMD Specialty conference on dynamic response of structures*, (Atlanta, GA), 1981.

[6] C. Georgiadis, *Wave Induced Vibrations of Continuous Floating Structures*. Doctoral dissertation, University of Washington, 1981.

[7] B. J. Hartz and C. Georgiadis, "A finite element program for dynamic response of continuous floating structures in short-crested waves," in *Proceedings, International Conference on Finite Element Analysis*, (Shanghai), PRC 1982, 1982.

[8] I. Holand, R. Sigbjörnsson, and I. Langen, "Dynamic analysis of a curved floating bridge," in *IABSE Proceedings*, (Trondheim, Norway), pp. P–5/77 1–16, IABSE, Zürich, 1977.

[9] D. Clough, R. Sigbjornsson, and S. N. Remseth, "Response of a submerged, buoyant tubular bridge subjected to irregular sea waves," *SINTEF Rep.*, vol. 71, p. A77028, 1977.

[10] I. Holand and I. Langen, "Salhus floating bridge: theory and hydrodynamic coefficients," tech. rep., 1972.

[11] L. E. Borgman, "Ocean wave simulation for engineering design," tech. rep., 1967.

[12] R. Sigbjörnsson and I. Langen, "Dynamisk analyse av flytebro i irregulære kortkammede bølger," tech. rep., SINTEF, Trondheim, Norway, 1979.

[13] I. Langen and R. Sigbjörnsson, "On stochastic dynamics of floating bridges," *Engineering Structures*, vol. 2, no. 4, pp. 209–216, 1980.

[14] B. J. Leira and I. Langen, "Probabilistic Aspects of Floating Bridge Design," in *Proc. ICOSSAR*, (Kobe, Japan), 1985.

[15] S. N. Remseth, B. J. Leira, K. M. Okstad, K. M. Mathisen, and T. Haukås, "Dynamic response and fluid/structure interaction of submerged floating tunnels," *Computers and Structures*, vol. 72, no. 4, pp. 659–685, 1999.

[16] M. Isaacson and O. U. Nwogu, "Wave loads and motions of long structures in directional seas," *Journal of Offshore Mechanics and Arctic Engineering*, vol. 109, no. 2, pp. 126–132, 1987.

[17] E. R. Morris, *A dynamic analysis of the Okanagan Lake floating bridge*. Doctoral dissertation, University of British Columbia, 1999.

[18] E. Morris, V. Szabo, G. Yang, and M. Isaacson, "Frequency domain dynamic analysis of a floating bridge," in *Coastal Structures 2003*, pp. 1334–1346, 2004.

[19] K. Inoue, "Mega Float: Achievements to Date And Ongoing Plan of Research," in *Proceedings of the Ninth (1999) International Offshore and Polar Engineering Conference*, (Brest, France), pp. 1–9, International Society of Offshore and Polar Engineers, 1999.

[20] K. Inoue, S. Nagata, and H. Niizato, "Stress Analysis For Detailed Mega-Float Structures Subject to Wave Loads," in *Proceedings of The Twelfth (2002) International Offshore and Polar Engineering Conference*, (Kitakyushu, Japan), pp. 283–289, International Society of Offshore and Polar Engineers, 2002.

[21] N. Kumamoto and T. Maruyama, "Elastic response analysis method for floating bridges in waves," tech. rep., Mitsubishi Heavy Industries, Ltd., 2000.

[22] E. Watanabe, T. Maruyama, H. Tanaka, and S. Takeda, "Design and construction of a floating swing bridge in Osaka," *Marine Structures*, vol. 13, no. 4-5, pp. 437–458, 2000.

[23] S. T. Peterson, *Experimental response and analysis of the Evergreen Point floating bridge*. Doctoral dissertation, Washington State University, 2002.

[24] B. Peeters and G. D. Roeck, "Stochastic System Identification for Operational Modal Analysis: A Review," *Journal of Dynamic Systems, Measurement, and Control*, vol. 123, no. 4, p. 659, 2001.

[25] Á. Cunha and E. Caetano, "Experimental modal analysis of civil engineering structures," *Sound and Vibration*, vol. 40, no. 6, pp. 12–20, 2006.

[26] F. Magalhães, Á. Cunha, and E. Caetano, "Dynamic monitoring of a long span arch bridge," *Engineering Structures*, vol. 30, pp. 3034–3044, nov 2008.

[27] D. M. Siringoringo and Y. Fujino, "System identification of suspension bridge from ambient vibration response," *Engineering Structures*, vol. 30, pp. 462–477, feb 2008.

[28] J. M. W. Brownjohn, F. Magalhaes, E. Caetano, and A. Cunha, "Ambient vibration re-testing and operational modal analysis of the Humber Bridge," *Engineering Structures*, vol. 32, pp. 2003–2018, aug 2010.

[29] R. M. Larssen, *Estimation of structural parameters from response measurements on submerged floating tunnels*. Doctoral dissertation, Norwegian University of Science and Technology, 1996.

[30] O. Faltinsen, *Sea loads on ships and offshore structures*, vol. 1. Cambridge university press, 1993.

[31] A. Naess and T. Moan, *Stochastic dynamics of marine structures*. New York: Cambridge University Press, 2012.

[32] J. N. Newman, *Marine hydrodynamics*. MIT press, 1977.

[33] B. Kinsman, *Wind waves: their generation and propagation on the ocean surface*. Courier Dover Publications, 1965.

[34] L. H. Holthuijsen, *Waves in oceanic and coastal waters*. Cambridge University Press, 2010.

[35] D. Hauser, K. Kahma, and H. E. Krogstad, "Measuring and analysing the directional spectra of ocean waves," tech. rep., 2005.

[36] K. A. Kvåle, R. Sigbjörnsson, and O. Øiseth, "Modelling the stochastic dynamic behaviour of a pontoon bridge: A case study," *Computers and Structures*, vol. 165, pp. 123–135, 2016.

[37] N. Kryloff and N. Bogoliuboff, *Introduction to nonlinear mechanics (translated by S. Lefschetz)*. No. 11, 1947.

[38] S. H. Crandall, "Perturbation Techniques for Random Vibration of Nonlinear Systems," *The Journal of the Acoustical Society of America*, vol. 35, pp. 1700–1705, nov 1963.

[39] M. K. Ochi, *Applied probability and stochastic processes in engineering and physical sciences*. Wiley New York, 1990.

[40] L. J. Tick, "The Estimation of "Transfer Functions" of Quadratic Systems," *Technometrics*, vol. 3, pp. 563–567, nov 1961.

[41] R. Taghipour, T. Perez, and T. Moan, "Hybrid frequency–time domain models for dynamic response analysis of marine structures," *Ocean Engineering*, vol. 35, pp. 685–705, may 2008.

[42] M. Shinozuka, "Monte Carlo solution of structural dynamics," *Computers & Structures*, vol. 2, pp. 855–874, jan 1972.

[43] K. A. Kvåle and O. Øiseth, "Characterization of the wave field around an existing end-supported pontoon bridge from simulated data," in *Proocedings of the International Conference on Earthquake engineering and Structural Dynamics*, (Reykjavik, Iceland), 2017.

[44] K. A. Kvåle and O. Øiseth, "Structural monitoring of an end-supported pontoon bridge," *Marine Structures*, vol. 52, pp. 188–207, mar 2017.

[45] D. Johnson, "DIWASP, a directional wave spectra toolbox for MATLAB®: User Manual," *Center for Water Research, University of Western Australia*, 2002.

[46] K. A. Kvåle, O. Øiseth, and A. Rønnquist, "Operational modal analysis of an end-supported pontoon bridge," *Engineering Structures*, vol. 148, pp. 410–423, oct 2017.

Paper 1

Knut Andreas Kvåle, Ragnar Sigbjörnsson, Ole Øiseth

"Modelling the stochastic dynamic behaviour of a pontoon bridge: A case study"

Computers & Structures, vol. 165, pp. 123–135, Mar. 2016.

Computers and Structures 165 (2016) 123–135

Contents lists available at ScienceDirect

Computers and Structures

journal homepage: www.elsevier.com/locate/compstruc

Modelling the stochastic dynamic behaviour of a pontoon bridge: A case study

Knut Andreas Kvåle, Ragnar Sigbjörnsson, Ole Øiseth *

Department of Structural Engineering, Norwegian University of Science and Technology, Trondheim, Norway

ARTICLE INFO

Article history:
Received 27 May 2015
Accepted 17 December 2015

Keywords:
Floating bridge
The Bergsøysund Bridge
Stochastic dynamics

ABSTRACT

Herein, a study on the hydrodynamic modelling of pontoon bridges is presented, with the Bergsøysund Bridge as a representative example. The model relies on the finite element method and linearized potential theory. The primary emphasis is placed on the stochastic response analysis within the framework of the power spectral density method. The quadratic eigenvalue problem is solved using a state-space representation and an iterative algorithm. The contribution of the fluid–structure interaction to the overall modal damping is investigated. Response effects due to changes in the sea state are studied. A frequency-independent approximation of the hydrodynamic coefficients is presented and discussed.

1. Introduction

Although the history of floating bridges may be traced back as far as 2000 BC [1], only in recent decades have floating bridges begun to be developed to a sufficient degree of sophistication such that they can be applied as critical components of modern infrastructure. Compared with land-based bridges, including cable-stayed bridges, only limited information on floating bridges is currently available, particularly regarding construction records, environmental conditions, durability, operations and performance. This is clear from the fact that only approximately twenty long floating bridges currently exist throughout the world. The major trends in the development of floating bridges and other very large floating structures (commonly abbreviated VLFSs) have been presented by Wang et al. [2] and Wang and Wang [3].

The state-of-the-art design philosophy for floating bridges in 1997 was outlined by Moe [4]. It was remarked that standard engineering practices were not directly applicable to floating bridges. A verified design code for floating bridge design would drastically reduce the effort required during the planning stage and would thus increase the potential economic advantages of floating bridges over many alternative bridge concepts. From a broader perspective, a unifying, efficient, and reliable method for simulating the behaviour of floating bridges is the primary goal.

The Norwegian Public Roads Administration (NPRA) is currently investigating possible technological solutions for a ferry-free Coastal Highway Route E39 along the western coast of Norway. This route stretches 1100 km between the cities of Kristiansand and Trondheim and requires multiple crossings of deep and wide fjords. The ferry-free crossings of these deep fjords represent considerable engineering challenges that are difficult or impossible to solve using existing bridge technology; pontoon-type floating bridges have been proposed as feasible options.

Of all existing floating bridges, only a few rely on discretely distributed pontoons, whereas the remainder are based on continuous pontoon girders. The majority of these bridges are also provided with additional stiffness through side-mooring. Only two long-span end-supported floating bridges exist in the world: the Bergsøysund Bridge and the Nordhordland Bridge, both relying on discretely distributed pontoons and both located in Norway. In connection with the planning of these structures, interest in the stochastic dynamic behaviour of floating bridges flourished in certain research communities, who combined the knowledge from the highly developed Norwegian offshore industry with knowledge gained during the construction of the floating bridges found in the State of Washington, USA, and in British Columbia, Canada. Much of this pioneering work can be credited to the research groups of Holand and Hartz (see, e.g., [5–11]) and Borgman [12]. The methodology was further developed, elaborated and exemplified by Sigbjörnsson [13] and by Langen and Sigbjörnsson [14].

Since the remarkable efforts contributed to the methodology in the 70s and early 80s, few case studies have been performed on real floating bridges. The effects of the flexibility of the superstructure of a pontoon bridge were studied by Kumamoto and Maruyama [15], who emphasized the relevance of such a study in regard to the design of the Yumeshima–Maishima (Yumemai) Bridge in Osaka, Japan, around the year 2000. This unique bridge is described in [16] and is the successor to the previous massive

* Corresponding author.

http://dx.doi.org/10.1016/j.compstruc.2015.12.009
0045-7949/

research project concerning VLFSs in Japan: the Mega-Float. Seif and Inoue [17] performed a conceptual case study of the Bergsøysund Bridge, in which the response of the bridge was simulated in the time domain for various wave directions and spreading indices for a specified crest length.

Morris et al. [18] performed a frequency-domain analysis of the planned William R. Bennett Floating Bridge in British Columbia. Among other relevant contributions of more recent vintage are [19,20].

Floating bridges play a modest role in modern infrastructure, partly because of the limited knowledge of the uncertainties that arise with increased spans. The longest existing floating bridges are moored to the seabed and rely on continuous pontoon solutions. However, individual pontoons are beneficial in many cases, and for deep straits such as fjords, it is not practically feasible to incorporate anchoring. From this kind of design follows a greater importance of the correlation of the wave action field.

An intermediate study concerning the stochastic modelling of the dynamic behaviour of the Bergsøysund Bridge was performed by Kvåle et al. [21]. The cited paper presents a similar study of the Bergsøysund Bridge; however, the current paper is far more elaborate and extensive, with respect to both the model and the interpretation of the analyses. The current paper presents a two-part combined model of the Bergsøysund Bridge, in which the fluid–structure interaction is considered using linear potential theory and the superstructure is represented by a finite element (FE) model consisting of beams and shells. The presented model serves as a basis for evaluating and discussing the damping contribution from the fluid–structure interaction. The effects of changes in the sea state, as represented by the crest length and the significant wave height, are studied in terms of both the wave excitation and the global response of the bridge. Because of the discretely distributed pontoons used in the bridge design, the wave excitation acts at only a few well-separated points. Thus, the correlation of the wave action on the bridge is an important issue and a vital aspect of this paper. With time-domain analyses in mind, the memory effect in the contribution from the fluid–structure interaction is avoided by applying two different frequency-independent approximations, and the resulting errors are discussed.

2. Outline of the theoretical model

A floating bridge is a complex structure, requiring theories from multiple scientific fields for the establishment of a complete numerical model. This section serves to outline the theoretical and mathematical framework needed for such a model. The frequency-domain equations of motion are established in Section 2.1. To solve these equations of motion with regard to the response, the power spectral density method is introduced in Section 2.2. The load acting on the structure is established through a random, Gaussian representation of the sea surface, which is established in Section 2.3 in the form of spectral densities. Furthermore, the load spectral densities are computed based on the sea surface spectral densities, as discussed in Section 2.4. To obtain a useful interpretation of the global system, a modal study is beneficial. Because of the self-exciting nature of a floating bridge, particular attention must be paid to the eigenvalue solution, as shown in Section 2.5.

2.1. Equations of motion

Within the framework of a finite element method (FEM) formulation, the equations of motion for a floating structure can be written as follows (see, e.g., Naess and Moan [22]):

$$[M_s]\{\ddot{u}(t)\} + [C_s]\{\dot{u}(t)\} + [K_s]\{u(t)\} = \{p_h(t)\} \tag{1}$$

where t is the time; $[M_s]$, $[C_s]$ and $[K_s]$ are the structural mass, damping and stiffness matrices, respectively; $\{u(t)\}$ is the displacement vector; and $\{p_h(t)\}$ is the total hydrodynamic action, including both the fluid–structure interaction and the wave action. The floating elements contribute via forces from the interaction between the water and the structure. The total hydrodynamic action can be formally expressed as follows:

$$\{p_h(t)\} = \int_{-\infty}^{\infty}[m_h(t-\tau)]\{\ddot{u}(t)\}d\tau + \int_{-\infty}^{\infty}[c_h(t-\tau)]\{\dot{u}(t)\}d\tau + [K_h]\{u(t)\} + \{p(t)\} \tag{2}$$

Here, $[m_h(t)]$ and $[c_h(t)]$ are the time-domain representations of the added hydrodynamic mass and the added hydrodynamic damping, respectively; and $\{p(t)\}$ represents the wave excitation forces. The first three terms on the right-hand side are models of the fluid–structure interaction forces. The time-domain representation of the added mass, $[m_h(t)]$, is related to the frequency-dependent hydrodynamic mass, $[M_h(\omega)]$, as follows:

$$[m_h(t)] = \frac{1}{2\pi}\int_{-\infty}^{\infty}[M_h(\omega)]e^{i\omega t}d\omega \tag{3}$$

Similarly, for the hydrodynamic damping, the following holds:

$$[c_h(t)] = \frac{1}{2\pi}\int_{-\infty}^{\infty}[C_h(\omega)]e^{i\omega t}d\omega \tag{4}$$

The restoring forces, however, are assumed to be independent of frequency. This implies that the frequency-domain and time-domain representations are identical. Here, the angular frequency is denoted by ω, and $i \equiv \sqrt{-1}$.

The wave excitation force, $\{p(t)\}$, is modelled herein as a homogeneous, stochastic, Gaussian process. The literature supports the validity of this assumption for the case of deep water and moderate wave heights (see, e.g., [23]). It follows that the response process inherits the properties of Gaussianity and homogeneity. It is assumed that the displacement and force processes can be expressed using generalized harmonic decomposition [24] as follows:

$$\{u(t)\} = \int_{-\infty}^{\infty} e^{i\omega t}\{dZ_u(\omega)\} \tag{5}$$

$$\{p(t)\} = \int_{-\infty}^{\infty} e^{i\omega t}\{dZ_p(\omega)\} \tag{6}$$

where $\{Z_u(\omega)\}$ and $\{Z_p(\omega)\}$ are the spectral processes corresponding to the response vector and the wave excitation force vector, respectively. The equations of motion can now be re-written in the frequency domain as follows:

$$\left(-\omega^2[M(\omega)] + i\omega[C(\omega)] + [K]\right)\{dZ_u(\omega)\} = \{dZ_p(\omega)\} \tag{7}$$

The fluid–structure interaction gives rise to inertia, damping and restoring forces. Hence, the system mass, damping and restoration (stiffness) are expressed as follows:

$$[M(\omega)] = [M_s] + [M_h(\omega)] \tag{8}$$

$$[C(\omega)] = [C_s] + [C_h(\omega)] \tag{9}$$

$$[K(\omega)] = [K_s] + [K_h] \tag{10}$$

By applying linearized potential theory, numerical values can be established for the wave excitation process, the hydrodynamic restoration matrix, the frequency-dependent added damping matrix and the frequency-dependent added mass matrix. This will be further discussed in Section 2.4. For further details regarding the establishment of the equations of motion, the reader is referred to [22].

2.2. Solution technique – the power spectral density method

The probabilistic properties of the response and wave excitation processes can be fully described in terms of the cross-spectral density, provided that the mean value is zero. The cross-spectral densities of the displacement response, $\{u(t)\}$, and the wave action process, $\{p(t)\}$, can be expressed as follows [25,13,26]:

$$[S_u(\omega)]d\omega = E\left(\{dZ_u(\omega)\}\cdot\{dZ_u(\omega)\}^H\right) \tag{11}$$

$$[S_p(\omega)]d\omega = E\left(\{dZ_p(\omega)\}\cdot\{dZ_p(\omega)\}^H\right) \tag{12}$$

where the Hermitian operator $()^H$ is introduced to represent the complex conjugate and matrix transpose and $E()$ is the expectation operator. Combining Eqs. (11) and (12) with Eq. (7) results in the following well-known expression:

$$[S_u(\omega)] = [H(\omega)][S_p(\omega)][H(\omega)]^H \tag{13}$$

This represents the power spectral density method and enables the computation of the response spectral densities given the spectral densities of the applied wave action.

2.3. Modelling the sea surface

The sea surface elevation is modelled as a scalar quantity given as a function of the location in space $\{x\}$ and time t, and it is an inherently random process. This is discussed in detail in Kinsman's book [27]. A thorough review of the stochastic modelling of directional seas can be found in [28]. The sea surface can be expressed mathematically in terms of the following integral:

$$\eta(\{x\},t) = \int \exp\left(i\{\kappa\}\cdot\{x\} - i\omega t\right)dZ_\eta(\{\kappa\},\omega) \tag{14}$$

where $\{\kappa\} = \{\kappa_x \quad \kappa_y\}$ is the wave number vector, ω is the frequency, and Z_η is the spectral process corresponding to the sea surface elevation. For stationary and homogeneous random fields, the spectral process is related to the wave spectral density as follows:

$$\begin{aligned} E\left(dZ_{\eta_r}(\{\kappa\},\omega)dZ_{\eta_s}(\{\kappa\},\omega)^H\right) &= dG_{\eta_r\eta_s}(\{\kappa\},\omega) \\ &= S_{\eta_s\eta_r}(\{\kappa\},\omega)d\kappa_x d\kappa_y d\omega \end{aligned} \tag{15}$$

where the indices r and s correspond to two points in space (and generally also time), $G_{\eta_r\eta_s}(\{\kappa\},\omega)$ denotes the spectral distribution, and $S_{\eta_r\eta_s}(\{\kappa\},\omega)$ is the corresponding spectral density. In polar coordinates, the wave number vector can be expressed as follows:

$$\{\kappa\} = \begin{Bmatrix}\cos\theta \\ \sin\theta\end{Bmatrix}\kappa \tag{16}$$

Here, θ refers to the wave direction and κ is the modulus of the wave number vector. Within the framework of Airy wave theory, the wave number and wave frequency are related through the dispersion relation:

$$\omega^2 = g\kappa\tanh(\kappa h) \tag{17}$$

where g is the acceleration of gravity and h is the water depth. For deep-water waves, $\tanh(\kappa h)\approx 1$. Hence, the cross-spectral density can be expressed as a function of the wave frequency and wave direction. The two-dimensional auto-spectral density is obtained from the cross-spectral density by merging the points r and s. For a homogeneous stochastic wave field, the two-dimensional wave spectral density is a function that is independent of the considered point in space:

$$S_{\eta_r\eta_r}(\omega,\theta) = S_{\eta_s\eta_s}(\omega,\theta) \tag{18}$$

This implies that the auto-spectral density can be expressed as a function of frequency and direction, i.e., $S_\eta(\omega,\theta)$; this quantity is commonly referred to as the directional wave spectral density and is traditionally written as follows:

$$S_\eta(\omega,\theta) = S_\eta(\omega)D(\omega,\theta) \tag{19}$$

where $S_\eta(\omega)$ is the so-called one-dimensional wave spectral density and $D(\omega,\theta)$ is the directional distribution. The cross-spectral density of the water elevation can then be expressed as follows for deep-water waves, under the assumption that the directional function is independent of the frequency [13]:

$$S_{\eta_r\eta_s}(\omega) = S_\eta(\omega)\int_{-\pi}^{\pi} D(\theta)\exp\left(-i\frac{|\omega|\omega}{g}(\Delta x\cos\theta + \Delta y\sin\theta)\right)d\theta \tag{20}$$

Here, Δx and Δy represent the distance between the points r and s and the mean wave direction is taken to be zero. The integral term expresses the coherency between the wave heights at the two points.

2.4. Fluid–structure interaction

The hydrodynamic forces acting on a submerged body due to a stochastic sea wave can be expressed using the following equation:

$$\{dZ_h(\omega)\} = \{dZ_p(\omega)\} - \left(-\omega^2[M_h(\omega)] + i\omega[C_h(\omega)] + [K_h]\right)\{dZ_u(\omega)\} \tag{21}$$

The vector $\{dZ_p(\omega,\theta)\}$ denotes the wave-induced process, which can be related to the wave process $dZ_\eta(\omega,\theta)$ as follows:

$$\{dZ_p(\omega,\theta)\} = \{Q_r(\omega,\theta)\}dZ_\eta(\omega,\theta) \tag{22}$$

Here, $\{Q_r(\omega,\theta)\}$ denotes the hydrodynamic transfer function that relates the wave-induced force process and the wave amplitude process, where r refers to the spatial location of an element, i.e., a pontoon. The total hydrodynamic action process $\{dZ_h(\omega)\}$ describes the fluid–structure interaction and the wave action induced by the prescribed sea state. Hydrodynamic transfer functions and fluid–structure interaction contributions are commonly established based on potential theory or experiments in wave basins. Panel methods are used to simulate the flow field around a body based on the superposition of known potential flow solutions. In this manner, simulations of the submerged body exposed to a wave of unit height with varying frequency and direction can yield both the hydrodynamic transfer functions and the hydrodynamic coefficients (mass, damping, and stiffness). The reader is referred to [29] for a thorough description of the application of potential theory to obtain these quantities. It is important to note that under the assumption of potential flow, all viscous effects are disregarded. Furthermore, potential flow methods are fundamentally based on superposition, making them linear by nature.

Finally, the cross-spectral density matrix corresponding to the wave excitation acting between two selected points can be written as follows:

$$[S_{p_rp_s}(\omega)] = \int_\theta \{Q_r(\omega,\theta)\}S_{\eta_r\eta_s}(\omega,\theta)\{Q_s(\omega,\theta)\}^H d\theta \tag{23}$$

Here, $\{Q_r(\omega,\theta)\}$ is the directional wave excitation transfer function for element r and $\{Q_s(\omega,\theta)\}$ is the directional wave excitation transfer function for element s. The matrix in Eq. (23) corresponds to the six local degrees of freedom (DOFs) of points r and s and is included as a sub-matrix within the full cross-spectral density matrix corresponding to the wave excitation of all points of interest.

2.5. Eigenvalue solution

When damping is not neglected, the eigenvalues and eigenvectors become complex. The eigenvalue problem then reads as follows:

$$\left(\lambda^2[M(\omega)] + \lambda[C(\omega)] + [K]\right)\{u\} = \{0\} \tag{24}$$

Because the mass and damping matrices are non-linear functions of frequency, the eigenvalue problem is, in general, non-linear and must be solved in an iterative manner. First, the frequency dependence is disregarded. Then, Eq. (24) can be re-written in state-space as follows:

$$\begin{Bmatrix} \{\dot{u}\} \\ \{\ddot{u}\} \end{Bmatrix} + \begin{bmatrix} [0] & -[I] \\ [M]^{-1}[K] & [M]^{-1}[C] \end{bmatrix} \begin{Bmatrix} \{u\} \\ \{\dot{u}\} \end{Bmatrix} = \begin{Bmatrix} \{0\} \\ [M]^{-1}\{p\} \end{Bmatrix} \tag{25}$$

In condensed form, this reads as follows:

$$\{\dot{z}\} + [A]\{z\} = \{Q\} \tag{26}$$

This results in the following solution for the state-space variable:

$$\{z\} = \sum_{r=1}^{2N} \{q_r\} e^{\lambda_r t} \tag{27}$$

where $\{q_r\}$ and λ_r are the eigenvector and eigenvalue, respectively, corresponding to solution r of Eq. (26). It is assumed that the eigenvalues are sorted such that $\{q_{r+N}\}$ and λ_{r+N} are complex conjugates of $\{q_r\}$ and λ_r, respectively. This can further be re-written in this compact manner, representing the displacements only:

$$\{u\} = [\Psi]\{g\} \tag{28}$$

where $[\Psi]$ is the modal transformation matrix that contains the complex mode shapes and $\{g\}$ represents the generalized DOFs.

Because of the frequency dependency of the matrices that form the eigenvalue problem, it is a non-linear problem, which, in this case, is solved by iteration. The iterative procedure used for this purpose is illustrated by the pseudocode presented in Table 1. The main workings of this algorithm are identical to those of the algorithms used to solve similar problems related to the wind loads on suspension bridges, as described by Agar [30].

The eigenvalues for an under-critically damped and frequency-independent SDOF problem are as follows:

$$\lambda_r = -\xi_r\omega_r \pm \sqrt{1-\xi_r^2}\,\omega_r i \tag{29}$$

This results in the following well-known relations:

$$\omega_r = |\lambda_r| \tag{30}$$

$$\xi_r = -\frac{\Re(\lambda_r)}{|\lambda_r|} \tag{31}$$

Table 1
Pseudocode of the iterative algorithm used to solve the eigenvalue problem.

```
INPUT N, tolerance
FOR n = 1 to 2N
    ω = 0
    diff = tolerance + 1
    WHILE diff > tolerance
        Solve eigenvalue problem for chosen ω ⇒ λ_r and {q_r}
        Sort λ_r, and correspondingly sort {q_r}
        ω_0 = ω
        ω = |λ_n|   (n = r)
        diff = |ω_0 − ω|
    END
    Store eigenvalue λ_n = λ_r and eigenvector {q_n} = {q_r}
END
```

where ω_r and ξ_r are the undamped natural frequency and the critical damping ratio, respectively, of mode r.

3. Case study: The Bergsøysund Bridge

The Bergsøysund Bridge is a 931 m long floating bridge that crosses the strait between Aspøya and Bergsøya, located on the northwestern coast of Norway. This bridge consists of a steel truss supported by 7 discretely distributed light-weight concrete pontoons, as shown in Figs. 1 and 2. The geography surrounding the bridge is depicted in the map shown in Fig. 3. As indicated in Fig. 4, the depth of the strait at all pontoon locations except one is approximately equal to or greater than 100 m; therefore, it is reasonable to model the problem using deep-water waves. No mooring is present, which makes this bridge a very interesting case study: the Bergsøysund Bridge is one of the longest end-supported floating bridges in the world.

3.1. Two-part combined model

In the computational set-up, which is illustrated in Fig. 5, the problem is divided into two sub-structures: (i) an Abaqus FE model representing all structural contributions, including the inertia of the pontoons themselves and the constant buoyancy provided by the pontoons, and (ii) a DNV HydroD WADAM hydrodynamic model, excluding static contributions due to gravity and hydrostatics.

The FE model consists of the steel frame and the tension rods at both abutments, both represented by linear beam elements, as well as the bridge deck, represented by shell elements. A rendering of this model is shown in Fig. 6. The neoprene bearings at the ends of the bridge are modelled as linear springs.

The hydrodynamic contributions are considered separately for each pontoon. The pontoons are modelled with their natural waterlines near those indicated in the design plans for the bridge.

The set-up of the model is described step by step below, corresponding to the numbering indicated in Fig. 5:

1. The beams and shells in the FE model define the structural system matrices $[M_s]$ and $[K_s]$. Additionally, the inertia of the mass of the pontoons themselves, $[M_{h0}]$, and the frequency-independent buoyancy (stiffness) from the hydrodynamic model, $[K_h]$, are included. Note that the stiffness contributions corresponding to each pontoon, $[K_{h,i}]$, must be transformed and summed; both of these tasks are performed in the FE software.
2. A modal analysis of the FE model is performed, yielding the modal transformation matrix, $[\Phi^l]$, and the natural frequencies, ω_n^l.
3. The modal quantities are used to establish the modal system matrices, $[\widetilde{M}^l]$ and $[\widetilde{K}^l]$, corresponding to a preselected number of vibration modes. Rayleigh damping is enforced to establish the modal damping matrix, $[\widetilde{C}^l]$, with mass and stiffness proportionality constants of $\alpha = \beta = 5 \cdot 10^{-3}$. The assumed values of these parameters correspond to a very lightly damped steel structure, i.e., with damping in the range of 0.5–1.0% of critical damping.
4. The seven pontoons of the bridge can be classified into three types (1 and 7; 2 and 6; 3, 4 and 5) based on the physical properties arising from their geometries and ballasting; thus, three different pontoon models are needed. The hydrodynamic stiffness contributions from each pontoon are not included here because they are considered as part of the FE model. The hydrodynamic mass and damping matrices representing the contributions of the individual pontoons

Fig. 1. The Bergsøysund Bridge. Photograph: K.A. Kvåle.

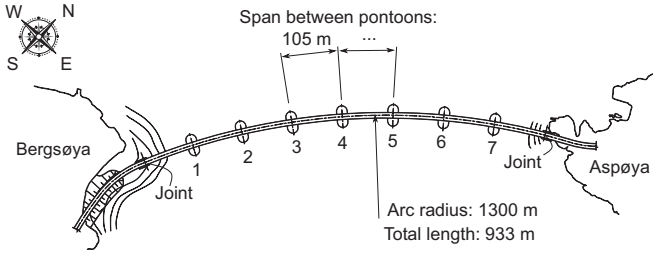

Fig. 2. Overhead view of the Bergsøysund Bridge, including the chosen pontoon numbering.

Fig. 3. Map section showing the geography surrounding the bridge. © Kartverket (www.kartverket.no). Two map sections from Kartverket are combined in this figure.

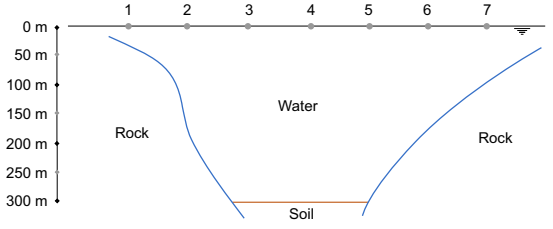

Fig. 4. Water depth profile across the strait, with annotations indicating pontoon locations.

are therefore the only contributions that are considered as part of sub-structure II. The discretization used for the hydrodynamic system matrices is provided in Table 2.

5. To form the total mass and damping contributions, the pontoon-wise matrices corresponding to sub-structure II are transformed into the global DOFs and summed.
6. The global mass and damping from sub-structure II are transformed into the modal space defined by sub-structure I using the modal transformation matrix $[\Phi^I]$.
7. The total modal system matrices are established by summing the contributions from sub-structures I and II. These matrices are used to establish the modal frequency-domain transfer function, $[\tilde{H}(\omega)]$.
8. The numerical functions for the one-dimensional wave spectral density and the spreading function are established based on the chosen models (in this case, the one-parameter Pierson–Moskowitz spectrum for the one-dimensional wave spectral density and cos-2s for the spreading function). The numerical two-dimensional wave spectral density is established.
9. Based on the same three hydrodynamic analyses as those used to establish the hydrodynamic mass, damping and stiffness, the hydrodynamic transfer function, $\{Q_r(\omega,\theta)\}$, is established. The discretization used for the hydrodynamic transfer function is provided in Table 2.
10. Eq. (23) is solved numerically for all combinations of pontoons (7^2). At this point, the hydrodynamic transfer function is transformed into the global coordinate system.
11. The sub-matrices are stacked to form the total load spectral density matrix.
12. The load spectral density matrix is transformed into the modal space defined by sub-structure I.
13. The power spectral density method (Eq. (13)) is used to establish the displacement spectral densities.
14. Finally, the response spectral density is transformed from modal into physical DOFs.

3.2. Modal parameters

By employing the algorithm introduced in Table 1, the frequency-dependent eigenvalue problem was solved, yielding the natural frequencies, damping estimates and mode shapes. The natural frequencies presented are the undamped ones. The resulting mode shapes were used to sort the modes according to their displacement type into horizontally transversal (H), vertically transversal (V), torsional (T), and combinational (C) modes. The natural frequencies and critical damping ratios for 10 selected modes are presented in Table 3, and the corresponding mode shapes are presented in Fig. 7.

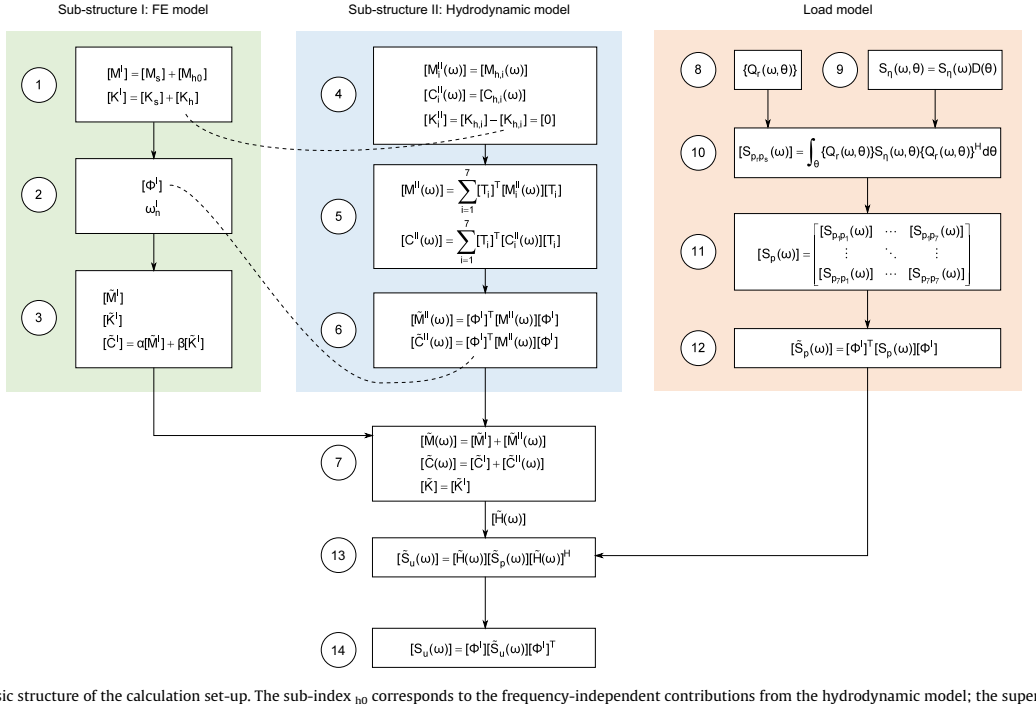

Fig. 5. Basic structure of the calculation set-up. The sub-index $_{h0}$ corresponds to the frequency-independent contributions from the hydrodynamic model; the superindices ^{I} and ^{II} correspond to sub-structures I and II, respectively; and $\sim$ indicates modal quantities.

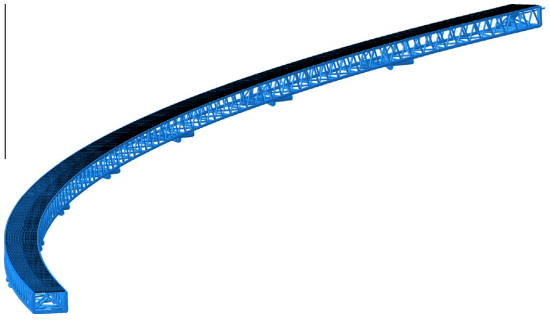

Fig. 6. Rendering of the FE model.

Table 2
Properties of the discretization used in the hydrodynamic analysis. The angle is defined as the angle between the positive local x axis of the pontoon and the wave direction.

Variable	Range	Increment	Affected quantities
Freq. [rad/s]	$[7.5 \cdot 10^{-2}, 4]$	$7.5 \cdot 10^{-2}$	$\{Q_r(\omega,\theta)\}$, $[M_h(\omega)]$, $[C_h(\omega)]$
Angle [°]	[0, 350]	10	$\{Q_r(\omega,\theta)\}$

Table 3
Undamped natural frequencies (and periods) and damping ratios obtained from the eigenvalue solution.

Mode no.	Period	Frequency		Damping	Type
	T [s]	ω [rad/s]	f [Hz]	ξ [%]	
1	10.7498	.5845	0.0930	1.792	H
2	7.1048	.8844	0.1408	1.298	C
3	6.1071	1.029	0.1637	11.80	V
4	5.9411	1.058	0.1683	10.66	V
5	5.2002	1.208	0.1923	7.418	C
6	5.1062	1.231	0.1958	9.234	H
7	4.3032	1.460	0.2324	3.155	V
8	3.8206	1.645	0.2617	1.115	T
9	3.3254	1.890	0.3007	6.696	H
10	3.3201	1.893	0.3012	1.078	V

The critical damping ratios of modes near 1 rad/s are found to be close to 12%. Compared with land-based steel structures, this ratio is very high. In the context of systems with significant hydrodynamic contributions, however, these damping values are not abnormally high. The high damping will affect the response spectral densities and result in blunt peaks at frequencies corresponding to these modes.

Additionally, the critical damping ratios and natural frequencies for all eigenvalues between 0 and 3 rad/s are presented in Fig. 8, along with the assessed Rayleigh damping mentioned above. From this figure, it is evident that hydrodynamic frequency-dependent damping contributes strongly to the overall damping of the structure. Upon investigation, Fig. 8 also shows that the damping ratios are clearly dependent on the type of mode. Notably, mode 9 has a significantly higher frequency than mode 6, despite their similarity. This is explained by the fact that mode 9 also includes a translational movement, resulting in a higher strain energy and, consequently, a higher frequency.

3.3. Load modelling

The hydrodynamic analysis yielded the discretized directional wave excitation transfer function $\{q_r(\omega,\theta)\}$, introduced in Eq. (23). Fig. 9 shows the transfer function vector for the middle pontoon in the model. The discretization used for the hydrodynamic transfer function is presented in Table 2.

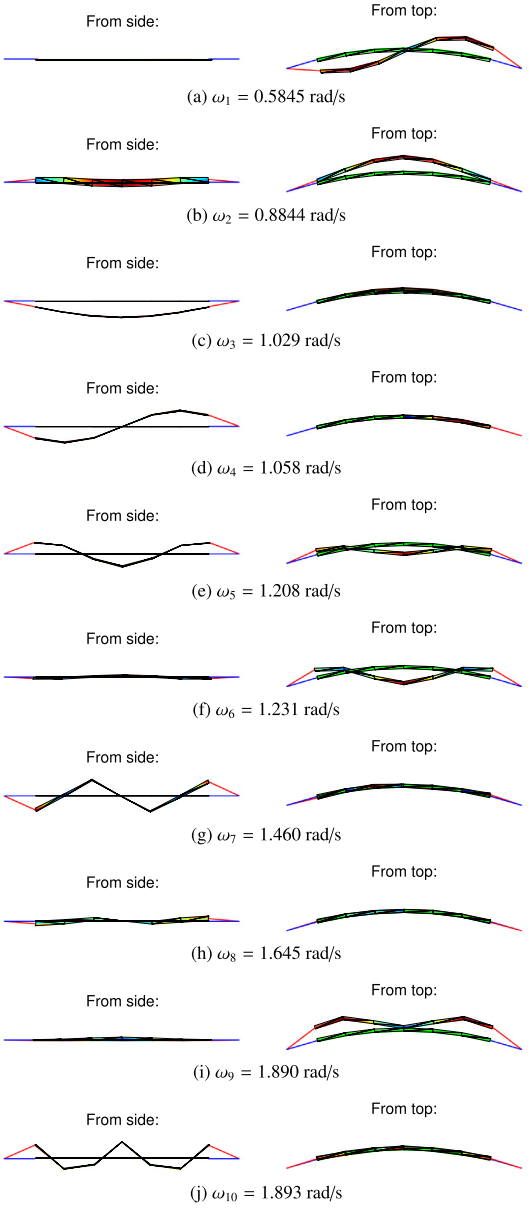

Fig. 7. Mode shapes obtained from the eigenvalue problem, corresponding to the natural frequencies and critical damping ratios presented in Table 3 and Fig. 8.

The one-parameter Pierson–Moskowitz wave spectral density suggested in [31] was used as the one-dimensional wave spectral density in the current case study. In this spectral density, the parameters of the generalized Pierson–Moskowitz spectral density are represented in terms of the significant wave height H_s as follows:

$$S_\eta(\omega) = \frac{A}{\omega^4} \cdot \exp\left(\frac{-B}{\omega^5}\right) \tag{32}$$

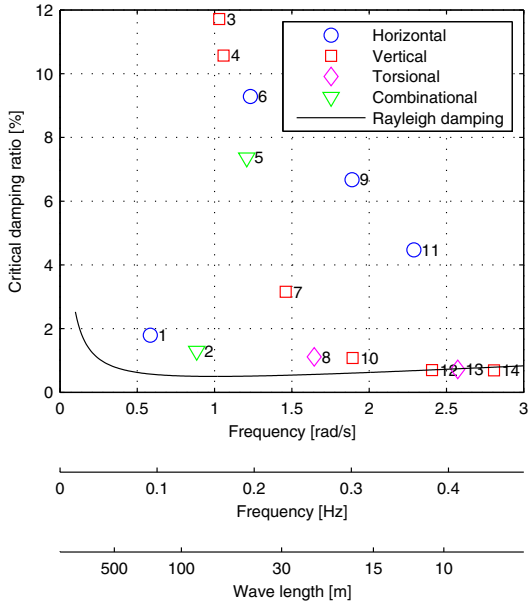

Fig. 8. Undamped natural frequencies and critical damping ratios obtained from the eigenvalue solution. The wavelength scale was constructed using Airy wave theory. The Rayleigh curve refers to the global damping added to the dry part of the structure and is not to be interpreted as a result of the eigenvalue solution.

where $A = \alpha g^2,\ B = 3.11/H_s^2,\ \alpha = 0.0081$, and g is the acceleration of gravity. The significant wave height H_s is defined as the mean wave height of the highest third of the waves (in a time series), which is often denoted by $H_{1/3}$. Furthermore, the significant wave height is related to the variance of the wave height process as follows: $H_s = 4\sigma_\eta$. The relationship between the peak wave period and the significant wave height in this spectral density model is plotted in Fig. 17 together with the measured data from a report by Veritec [32] regarding the sea state at the bridge site. This figure supports the assertion that this spectral density formulation is appropriate for the current case study.

The cos-2s distribution [33] was selected as the directional distribution $D(\theta)$:

$$D(\theta) = C\cos^{2s}\left(\frac{\theta-\theta_0}{2}\right) \tag{33}$$

where C is a normalization constant to ensure that $\int D(\theta)d\theta = 1$; s is the spreading parameter, which characterizes the crest length of the waves; θ_0 is the angle of the mean wave direction; and θ is assumed to lie within the range corresponding to valid states of the modelled sea state, i.e., $-\pi/2 < \theta - \theta_0 < \pi/2$. The mean wave angle, defined as the angle between the global x axis and the local y axis of the midmost pontoon, was chosen such that the bridge was symmetrically loaded, i.e., 90°.

The resulting directional distributions, for a mean angle of 90° and various spreading parameters, are shown in Fig. 11.

3.4. Sea-state effects

Changes in the spreading parameter s, the significant wave height H_s and the mean wave heading angle θ_0 directly affect the excitation of the structure. The effects on the response, particularly the correlation between response quantities, are more complex. Parameter studies based on simulations were performed to assess the effect of the parameters that characterize the sea state on the response.

3.4.1. Significant wave height

For the one-dimensional Pierson–Moskowitz spectral density used in this study, an increase in the significant wave height results in a lower peak frequency of the spectral density. This will, in turn, result in a higher excitation level and a lower peak frequency of the wave action. This effect is illustrated in Fig. 10 for significant wave heights corresponding to 1-year, 10-year and 100-year sea states, as reported in [32], together with the modal damping ratios and natural frequencies from the eigenvalue solution. From this figure, it is clear that the peak frequency of the wave action and the modes with the highest damping correspond better for higher significant wave heights. This means that for higher significant wave heights, the more highly damped modes are more strongly excited and therefore contribute more significantly to the overall response than in the case of lower significant wave heights. The high damping plays a crucial role in limiting the response of the structure, but high damping levels should not be regarded as strictly beneficial; high damping affects the correlations between the responses at different locations in the structure, potentially leading to larger local stress variations. During the design of a floating bridge, this effect should be taken into consideration.

The response was simulated for various significant wave heights. The resulting standard deviations of the heave motion and horizontally transversal motion of pontoons 4 and 6 are shown in Fig. 12. This figure reveals a significant increase in the horizontally transversal response of pontoon 6 as the significant wave height increases. This increase in response originates from the excitation of the first mode of vibration, the mode shape of which is presented in Fig. 7a. As the significant wave height increases, the frequency content of the wave excitation process will shift downwards, as shown in Figs. 10 and 17. This shift in frequency content excites the first vibrational mode, which is otherwise located in the low-level tail of the one-dimensional wave spectral density, and, in turn, significantly affects the response.

3.4.2. Crest length

The crest length is controlled by the spreading parameter s that appears in the directional distribution. In the current case study, the spreading parameter s was selected based on quantitative judgement and site observations. To obtain a more accurate measure of this quantity, wave recordings would be needed; however, such an effort is considered to be outside the scope of this study. The three values used for s in this survey (3, 30 and 1000) are considered to represent *short-crested*, *fairly long-crested* and *long-crested* sea conditions. Particular attention is focused on the value of $s = 3$, as on-site observations imply that a short-crested representation is the most realistic. To more clearly illustrate the effect of the spreading parameter on the sea surface, representations of the sea surface for $s = 3$, $s = 30$, and $s = 1000$ are shown in Figs. 13–15. The correlations between the wave height at the midmost pontoon and those along the rest of the bridge are shown in the same figures for the corresponding sea states.

These figures show that the correlations between the wave heights are very low; only when the waves are long-crested is there a non-zero wave-height correlation between neighbouring pontoons. As a result of the low correlation between the wave heights, the cross-spectral densities between the wave excitations of the different pontoons are very small and can be neglected for the types of sea states assumed at the bridge location. Note that the correlation plots are also highly dependent on the chosen one-dimensional wave spectral density. As the significant wave

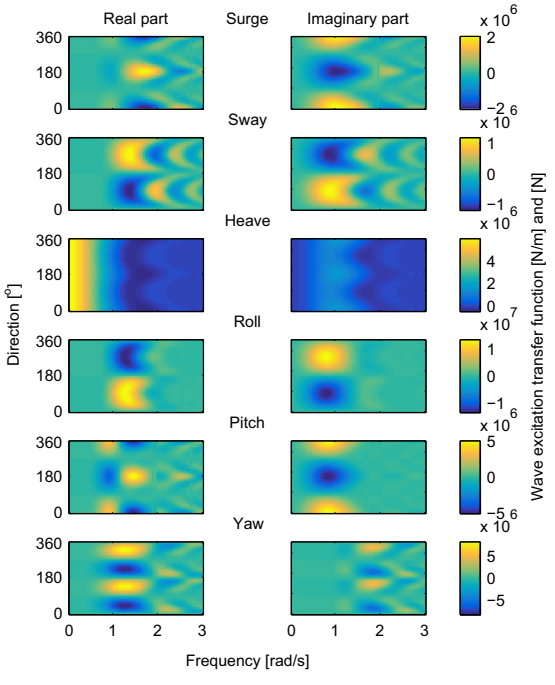

Fig. 9. Wave excitation transfer function for the middle pontoon obtained in the hydrodynamic analysis, where the rows correspond to the local degree of freedom as follows (from the top): x, y, z, θ_x, θ_y, and θ_z. The left column represents the real part, and the right column represents the imaginary part.

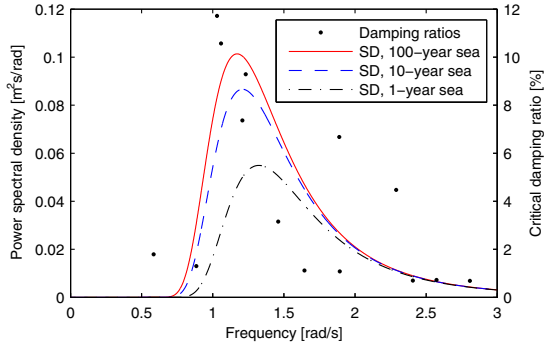

Fig. 10. Damping ratios and one-parameter Pierson–Moskowitz wave spectral densities corresponding to sea states of given return periods: $H_s = 1.41$ m for the 100-year sea state, $H_s = 1.15$ m for the 10-year sea state, and $H_s = 0.90$ m for the 1-year sea state [32].

height, which controls the form of the wave spectral density, increases, the highly correlated region expands dramatically in the directions both parallel and normal to the wave propagation.

The significant wave heights in the locations of other potential floating bridges may be far larger than those measured around the Bergsøysund Bridge, and therefore, it is important to understand the correlations between wave actions on different pontoons.

By simulating the responses for various spreading parameters, the statistics of the responses in various DOFs of the model were established. The standard deviations of the heave motion and horizontally transversal motion of pontoons 4 and 6 for varying s are

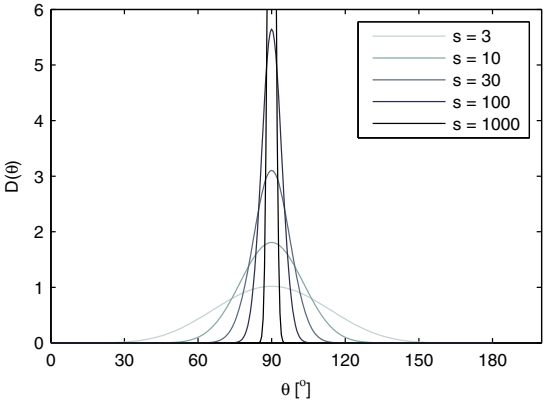

Fig. 11. The applied $\cos^{2s}$-based directional distribution, with a mean heading angle of 90°, for various spreading parameters.

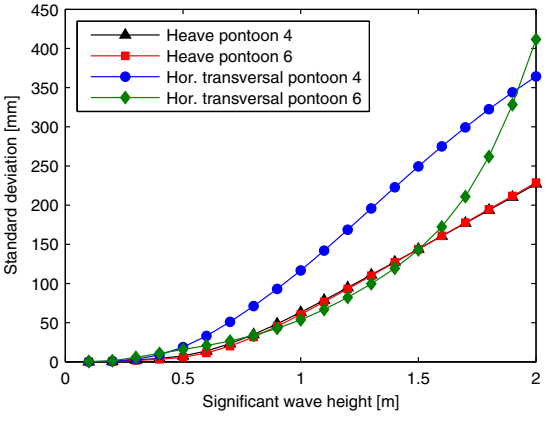

Fig. 12. Effects on the variance of selected responses with an increasing significant wave height for a spreading parameter of $s = 3$ and a mean wave heading angle of $\theta_0 = 90^\circ$.

shown in Fig. 16. This plot reveals a decrease in the response in terms of the horizontally transversal motion and an increase in the vertical motion. As the sea surface becomes more long-crested, the wave-excitation correlation increases; the pontoons are excited more simultaneously. This will, in turn, increase the response of the symmetric modes; however, it may also reduce the intensity of the antisymmetric modes of vibration. This is the cause of the somewhat unexpected behaviour in response to an increased crest length observed in the figure.

3.5. Bridge response due to typical sea state

The one-year sea state reported by Veritec, represented by a significant wave height of $H_s = 0.90$ m, is considered in the following. Furthermore, the crest length is chosen to be characterized by a spreading parameter of $s = 3$.

Figs. 18 and 19 present the resulting power spectral densities and coherences of the responses in the vertical and horizontal directions, respectively, for pontoons 3, 4 and 5; the corresponding statistics are summarized in Tables 4 and 5. The response spectral densities are represented with respect to the local DOFs of pontoon

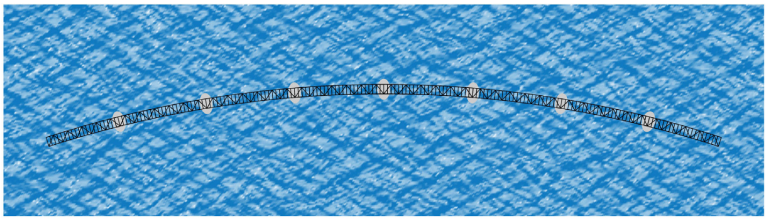

(a) Sea surface representation.

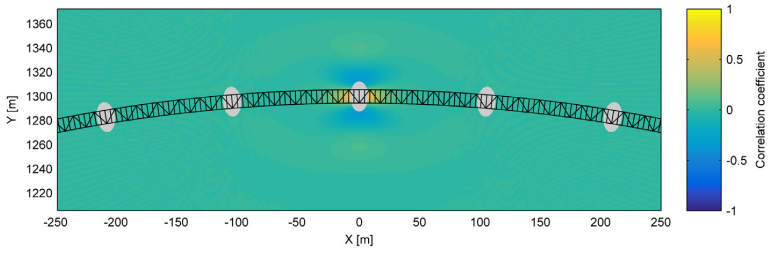

(b) Correlation with the wave height at the midmost pontoon.

Fig. 13. Sea surface representation and correlation with the wave height at the midmost pontoon for a sea state characterized by $H_s = 0.9$ m, $\theta_0 = 90^\circ$ and $s = 3$.

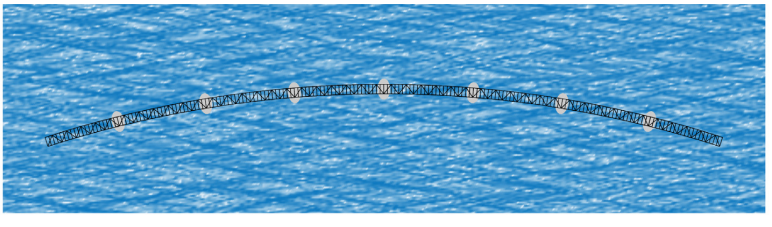

(a) Sea surface representation.

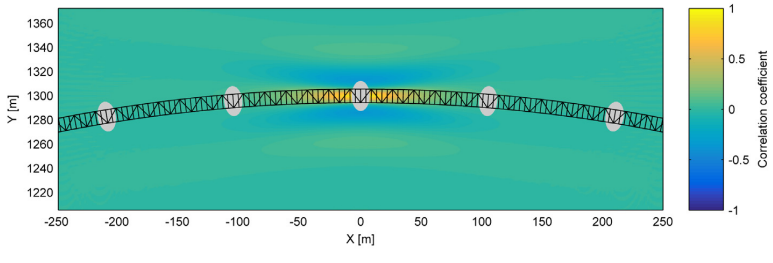

(b) Correlation with the wave height at the midmost pontoon.

Fig. 14. Sea surface representation and correlation with the wave height at the midmost pontoon for a sea state characterized by $H_s = 0.9$ m, $\theta_0 = 90^\circ$ and $s = 30$.

4. The vertical displacement responses are found to have low correlation values in general, a finding that is supported by the low coherence values between the vertical responses at the natural frequencies of the vertical modes of the bridge. The spectra that show the horizontal displacement responses do not share this tendency: high coherence is observed at and around the peaks representing the natural frequencies of the horizontal modes of the structures, and the horizontal response variables exhibit high correlations. The inconsistencies in the damping ratios between the horizontal and vertical modes, as shown in Fig. 8, are likely the cause of this result.

3.6. Simplified frequency-independent hydrodynamic model

When general non-linearities are added to the problem, a time-domain representation is close to inevitable. To properly include

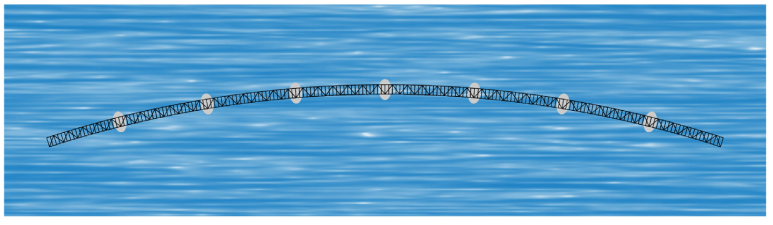

(a) Sea surface representation.

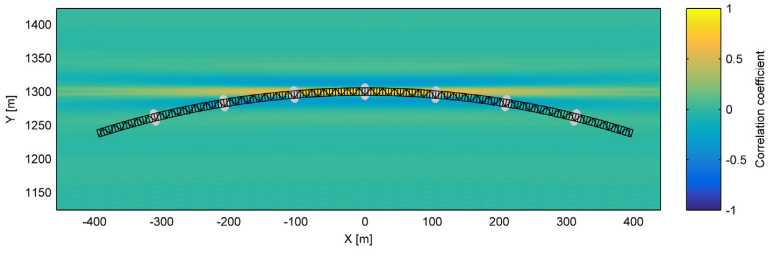

(b) Correlation with the wave height at the midmost pontoon.

Fig. 15. Sea surface representation and correlation with the wave height at the midmost pontoon for a sea state characterized by $H_s = 0.9$ m, $\theta_0 = 90^\circ$ and $s = 1000$.

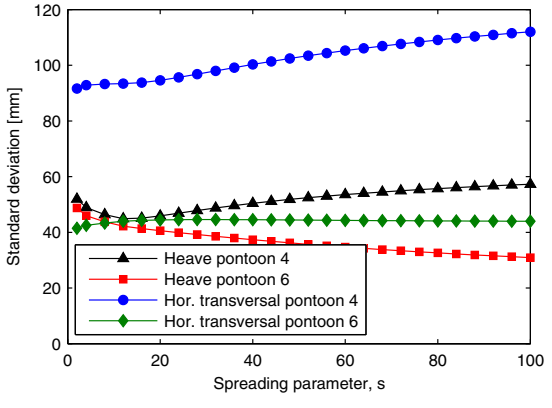

Fig. 16. Effects on the variance of selected responses with an increasing spreading parameter (and thus an increasing crest length) for a significant wave height of $H_s = 0.9$ m and a mean wave heading angle of $\theta_0 = 90^\circ$.

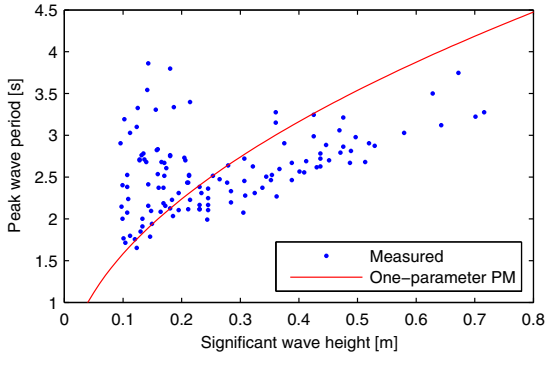

Fig. 17. Measurements of significant wave heights and wave peak periods, from the Veritec report [32], compared with the relation given by the one-parameter Pierson–Moskowitz (PM) spectral density used in the study.

the fluid–structure interaction, convolution integrals must be solved, which is considered to be a computationally expensive procedure. For this reason, approximations of the frequency-dependent coefficients as constant have received some attention in the literature. The success of simplifying the frequency-dependent hydrodynamic coefficients as independent of frequency is highly dependent on the wave action process; a narrow-banded process with a long characteristic period is much more likely to be amenable to this type of simplification. Several procedures for this purpose have been suggested, but the emphasis here is placed on approximating the frequency-dependent coefficients as constant based on their values at (i) the peak frequency corresponding to the one-dimensional wave spectral density and (ii) the weighted average frequency corresponding to the maximum peaks of the auto-spectral densities of the response, based on an exact frequency-domain solution. The weighted average of approximation (ii) is computed as follows:

$$\omega_{tot} = \frac{1}{\sum_{i=1}^{N} W_i} \sum_{i=1}^{N} W_i \cdot \omega_i \tag{34}$$

Here, the frequency corresponding to the largest value of the auto-spectral density $S_{i,i}(\omega)$ is denoted by ω_i, N is the total number of DOFs, and the weighting coefficients W_i are defined as follows:

$$W_i = \sqrt{\max\left(S_{i,i}(\omega)\right)} \tag{35}$$

A comparison of the standard deviations and correlation coefficients corresponding to the heave and horizontally transversal responses of pontoons 3 and 4 is presented in Table 6. To complement this table, the corresponding spectral densities are presented in Fig. 20. Both the figure and the table show that the second

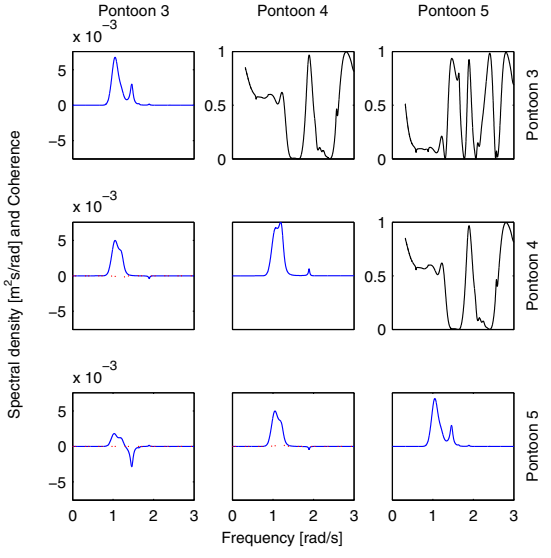

Fig. 18. Cross-spectral densities of the heave responses of the three midmost pontoons. The three black curves shown above the diagonal represent the coherence between the responses, and the blue and red/dotted curves denote the real and imaginary parts of the cross-power spectral densities, respectively. (For interpretation of the references to color in this figure legend, the reader is referred to the web version of this article.)

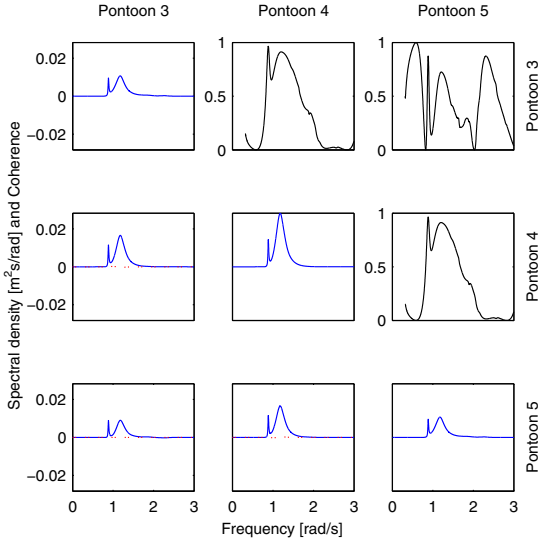

Fig. 19. Cross-spectral densities of the horizontally transversal responses of the three midmost pontoons. The three black curves shown above the diagonal represent the coherence between the responses, and the blue and red/dotted curves denote the real and imaginary parts of the cross-power spectral densities, respectively. (For interpretation of the references to color in this figure legend, the reader is referred to the web version of this article.)

approach generally outperforms the first. However, the results obtained using both procedures are rather crude, their greatest shortcoming being that they both underestimate and overestimate the response and the correlations.

Table 4
Covariances [mm²] and correlation coefficients (above the diagonal) for the heave responses of the three midmost pontoons. The statistics correspond to Fig. 18.

	Pontoon 3	Pontoon 4	Pontoon 5
Pontoon 3	1959	0.640	0.0825
Pontoon 4	1373	2345	0.640
Pontoon 5	161.5	1373	1959

Table 5
Covariances [mm²] and correlation coefficients (above the diagonal) for the horizontally transverse responses of the three midmost pontoons. The statistics correspond to Fig. 19.

	Pontoon 3	Pontoon 4	Pontoon 5
Pontoon 3	3919	0.897	0.702
Pontoon 4	5225	8662	0.897
Pontoon 5	2752	5224	3919

4. Concluding remarks

The potential of floating bridges for application as part of modern infrastructure is not fully utilized today, primarily due to the limited knowledge of their dynamic behaviours as their lengths are increased. Linear frequency-domain simulations were performed in a case study of the 23-year-old Bergsøysund Bridge in Norway, with emphasis on the response spectral densities determined using the power spectral density method and the modal parameters resulting from the complex and non-linear eigenvalue problem. The effects of different sea states and how they affect the response of the bridge were discussed.

The high damping contribution from the fluid–structure interaction results in low coherence and correlation between the heave response quantities along the bridge span. With damping levels as high as 12% for lateral modes, this result is as expected.

For a realistic 1-year sea state, a low correlation between the wave heights at the locations of the different pontoons was found; the action on each pontoon can therefore be considered independent. When the significant wave height increases to higher levels, however, the pontoons are exposed to correlated wave excitation. The correlation of the wave action amplifies the response of the modes with symmetric properties but may reduce the response of the antisymmetric modes. The geometry of the bridge also plays a crucial role in how strongly correlated the pontoon action becomes. Because the first mode of vibration has a frequency located in the tail of the one-dimensional wave spectral density for low and medium significant wave heights, its contribution to the global behaviour requires a rather large significant wave height.

The approximation of the fluid–structure interaction contributions as constant for a frequency corresponding to the weighted average frequency of the peak auto-spectral densities obtained from an exact frequency-domain solution, termed approximation (ii), performed decently for a realistic 1-year sea state. The performance of this approximation is expected to be significantly enhanced when the wave excitation process is less broadband in nature. The constant approximation of the frequency-dependent fluid–structure interaction contributions lacks consistency; it both underestimates and overestimates the response and must therefore be used with caution.

Verification of the calculation models used for floating bridges is important to ensure reliable analyses. To verify the model and quantify its uncertainties, experimental data regarding the behaviour of the bridge should be recorded and analyzed.

Table 6
Comparison of the standard deviations determined through exact computation with the standard deviations obtained using two different constant approximations of the frequency-dependent mass and damping matrices corresponding to the fluid–structure interaction. Approximation (i) uses the values of the matrices at the frequency corresponding to the peak of the one-dimensional wave spectral density, whereas approximation (ii) utilizes the matrix values at the average of the square-root-weighted frequencies corresponding to the peaks of the response spectral density obtained from an exact frequency-domain solution.

Component	Pontoon	Standard deviation [mm]			Correlation coefficient		
		Exact	Approx. (i)	Approx. (ii)	Exact	Approx. (i)	Approx. (ii)
Heave	No. 3	44.26	56.42	42.76	0.640	0.716	0.700
	No. 4	48.43	61.34	46.75			
Horizontal	No. 3	62.60	58.15	61.81	0.897	0.876	0.883
	No. 4	93.07	84.46	91.31			

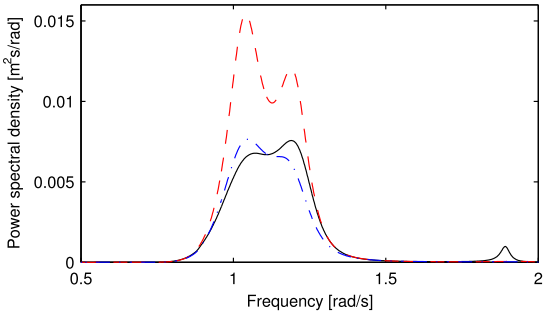

(a) Heave component.

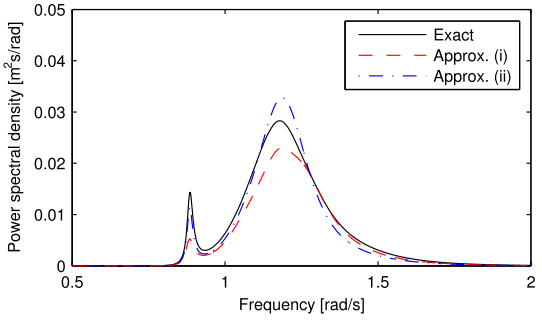

(b) Horizontally transversal component.

Fig. 20. Comparison of spectral densities obtained from exact and approximate solutions.

Acknowledgements

This research was conducted with financial support from the Norwegian Public Roads Administration. The authors gratefully acknowledge this support. Thanks are also given to the master's students who have contributed to the project.

References

[1] Watanabe E. Floating bridges: past and present. Struct Eng Int 2003;13(2):128–32.
[2] Wang CM, Watanabe E, Utsunomiya T. Very large floating structures. CRC Press; 2007.
[3] Wang CM, Wang BT. Large floating structures: technological advances, vol. 3. Springer; 2014.
[4] Moe G. Design philosophy of floating bridges with emphasis on ways to ensure long life. J Mar Sci Technol 1997;2(3):182–9.
[5] Holand I, Langen I. Salhus floating bridge: theory and hydrodynamic coefficients. SINTEF Rep 1972.
[6] Holand I, Langen I. Dynamic analysis of floating bridges. In: Aune P, Holand I, editors. Norwegian bridge building. Trondheim: Tapir Publishers; 1981.
[7] Clough D, Sigbjornsson R, Remseth SN. Response of a submerged, buoyant tubular bridge subjected to irregular sea waves. SINTEF Rep 1977;71.
[8] Langen I. Frequency domain analysis of a floating bridge exposed to irregular short-crested waves. SINTEF Rep 1980.
[9] Hartz BJ, Mukherji B. Dynamic response of a floating bridge to wave forces. In: Proc international conference on bridging Rion-Antirion. Patras, Greece; 1977.
[10] Hartz BJ. Dynamic response of the hood canal floating bridge. In: Proceedings second ASCE/EMD specialty conference on dynamic response of structures, Atlanta, GA; 1981.
[11] Hartz BJ, Georgiadis C. A finite element program for dynamic response of continuous floating structures in short-crested waves; 1982. <http://www.scopus.com/inward/record.url?eid=2-s2.0-0019936983&partnerID=tZOtx3y1>.
[12] Borgman LE. Ocean wave simulation for engineering design. Tech rep; 1967.
[13] Sigbjörnsson R. Stochastic theory of wave loading processes. Eng Struct 1979;1(2):58–64. http://dx.doi.org/10.1016/0141-0296(79)90014-2. <http://www.sciencedirect.com/science/article/pii/0141029679900142>.
[14] Langen I, Sigbjörnsson R. On stochastic dynamics of floating bridges. Eng Struct 1980;2(4):209–16. http://dx.doi.org/10.1016/0141-0296(80)90002-4. <http://www.sciencedirect.com/science/article/pii/0141029680900024>.
[15] Kumamoto N, Maruyama T. Elastic response analysis method for floating bridges in waves. Tech rep; 1999.
[16] Watanabe E, Maruyama T, Tanaka H, Takeda S. Design and construction of a floating swing bridge in Osaka. Mar Struct 2000;13(4–5):437–58. http://dx.doi.org/10.1016/S0951-8339(00)00016-2. <http://www.sciencedirect.com/science/article/pii/S0951833900000162>.
[17] Seif MS, Inoue Y. Dynamic analysis of floating bridges. Mar Struct 1998;11(12):29–46. http://dx.doi.org/10.1016/S0951-8339(97)00012-9. <http://www.sciencedirect.com/science/article/pii/S0951833997000129>.
[18] Morris E, Szabo V, Yang G, Isaacson M. Frequency domain dynamic analysis of a floating bridge. Coast Struct 2004;2003:1334–46. http://dx.doi.org/10.1061/40733(147)110.
[19] Shixiao F, Weicheng C, Xujun C, Cong W. Hydroelastic analysis of a nonlinearly connected floating bridge subjected to moving loads. Mar Struct 2005;18(1):85–107. http://dx.doi.org/10.1016/j.marstruc.2005.05.001. <http://www.sciencedirect.com/science/article/pii/S0951833905000377>.
[20] Raftoyiannis IG, Avraam TP, Michaltsos GT. Analytical models of floating bridges under moving loads. Eng Struct 2014;68:144–54. http://dx.doi.org/10.1016/j.engstruct.2014.03.002. <http://linkinghub.elsevier.com/retrieve/pii/S0141029614001400>.
[21] Kvåle KA, Øiseth O, Sigbjörnsson R. Modelling of the stochastic dynamic behaviour of the Bergsøysund Bridge: an application of the power spectral density method. In: Cunha A, Caetano E, Ribeiro P, Müller G, editors. Proceedings of the 9th International Conference on Structural Dynamics, EURODYN 2014. Porto; 2014. p. 2921–8.
[22] Naess A, Moan T. Stochastic dynamics of marine structures. New York: Cambridge University Press; 2012.
[23] Ochi MK, Wang W-C. Non-Gaussian characteristics of coastal waves. Coast Eng Proc 1984;1(19).
[24] Wiener N. Generalized harmonic analysis. Acta Math 1930;55(1):117–258. http://dx.doi.org/10.1007/BF02546511.
[25] Langen I, Sigbjörnsson R. Dynamisk analyse av konstruksjoner: dynamic analysis of structures. Tapir; 1979.
[26] Cramér H, Leadbetter MR. Stationary and related stochastic processes: sample function properties and their applications. Courier Corporation; 2013.
[27] Kinsman B. Wind waves: their generation and propagation on the ocean surface. Courier Dover Publications; 1965.
[28] Hauser D, Kahma K, Krogstad HE. Measuring and analysing the directional spectra of ocean waves. Tech rep; 2005.
[29] Faltinsen O. Sea loads on ships and offshore structures, vol. 1. Cambridge University Press; 1993.
[30] Agar T. Aerodynamic flutter analysis of suspension bridges by a modal technique. Eng Struct 1989;11(2):75–82. http://dx.doi.org/10.1016/0141-0296(89)90016-3. <http://www.sciencedirect.com/science/article/pii/0141029689900163>.
[31] Pierson WJ, Moskowitz L. A proposed spectral form for fully developed wind seas based on the similarity theory of S.A. Kitaigorodskii. J Geophys Res 1964;69(24):5181–90. http://dx.doi.org/10.1029/JZ069i024p05181.
[32] Skogen K, Dahl FE. Vind, strøm og bølger i Bergsøysundet (Krifast). Tech rep. Veritas Offshore Technology and Services A/S; 1989.
[33] Longuet-Higgins MS, Cartwright DE, Smith ND. Observations of the directional spectrum of sea waves using the motions of a floating buoy. In: Proc conf ocean wave spectra. Prentice-Hall; 1963. p. 111–32.

Paper 2

Knut Andreas Kvåle, Ole Øiseth

"Structural monitoring of an end-supported pontoon bridge"

Marine Structures, vol. 52, pp. 188–207, Mar. 2017.

Marine Structures 52 (2017) 188–207

Contents lists available at ScienceDirect

Marine Structures

journal homepage: www.elsevier.com/locate/marstruc

Structural monitoring of an end-supported pontoon bridge

Knut Andreas Kvåle*, Ole Øiseth

Department of Structural Engineering, Faculty of Engineering Science and Technology, NTNU, Norwegian University of Science and Technology, Trondheim, Norway

ARTICLE INFO

Article history:
Received 13 April 2016
Received in revised form 27 September 2016
Accepted 16 December 2016

Keywords:
The Bergsøysund Bridge
Floating bridge
Long-term extreme response

ABSTRACT

A comprehensive monitoring system is designed and installed on the Bergsøysund Bridge. The system is thoroughly described, including descriptions of all exact sensor positions and the fundamental workings of the system. Acceleration, displacement and excitation sources, such as wind and waves, are monitored. The effects on the response of the characterizing environmental parameters, namely, mean wind speed, mean wind direction, significant wave height, and wave peak period, are investigated, with long-term extreme response analyses in mind.

1. Introduction

The first concept of a floating bridge is believed to have appeared around 2000 BCE [1], but it was first applied as part of critical infrastructure during the last half of the 20th century. There is a constant strive to achieve longer spans, and thus, a good understanding of the current floating bridges is crucial.

The developments in the field of floating bridges and other very large floating structures (VLFSs) were reviewed by Wang et al. [2] and Wang and Wang [3]. In an international context, the continuous pontoon girder is by far the most common type of floating bridge. These bridges are generally side supported by anchoring to the seabed, which drastically reduces their flexibility. For some crossings, these two widespread characteristics are not feasible or beneficial. The crossings planned for the ferry-free Coastal Highway E39, on the northwestern coast of Norway, are examples of this case. The deep fjords make side anchoring to the seabed practically impossible. Furthermore, the requirement that ships should be able to pass through makes a discretely distributed pontoon solution more obvious. Only two long-span end-supported pontoon bridges exist worldwide: the Bergsøysund Bridge and the Nordhordland Bridge.

A structural monitoring system enables capturing of highly valuable recordings, describing both the environment and the bridge response. First, statistical data representing the relationships between environmental factors and the response can be established. Furthermore, the measurements will serve as a starting point for establishing the modal parameters, which characterize the bridge behaviour in an easily interpretable manner. By also monitoring the environment, the effect of changing environment on the modal parameters can be quantified. It is also possible, although challenging, to use the continuous recordings for structural health monitoring [4,5]. Numerous land-based civil structures have previously been instrumented for measuring response and environmental excitation (see, e.g., [6–8]). Similar surveys have been conducted for offshore structures (see, e.g., [9]). However, structural monitoring surveys of floating bridges are not widespread.

* Corresponding author.

http://dx.doi.org/10.1016/j.marstruc.2016.12.004
0951-8339/

Ultimate limit state (ULS) design checks are vital for all engineering structures, but these checks are far less straightforward for structures exposed to environmental excitations, such as floating bridges. Several approaches are commonly used for establishing the extreme load effects, and their appropriateness depends on how dynamic the structure is in both behaviour and excitation. The most accurate approach is the full long-term approach [10,11], but due to practical limitations, the traditional approach for offshore installations is to apply a simplified procedure, for example, as described in the NORSOK Standard (N-003) [12]. To perform a full long-term design evaluation, a joint probability density function (PDF) between all the characterizable environmental parameters is, in theory, required. Successfully establishing a close-to-exact PDF is cumbersome and unlikely. To assess the validity of the simplified approaches, a qualitative description of how the different environmental parameters are related to each other and the response is needed. This task is one of the main objectives of this paper. In other words, the answer to the following question is sought: what environmental parameters are the most crucial for the response of floating bridges?

The relationship between environmental factors and the response of the Bergsøysund Bridge is studied using a comprehensive measurement system. The correlations between several of the most common environmental parameters and the response of the bridge are studied in an attempt to describe the causalities between them. All important aspects of the measurement system are presented in detail, including accurate positions of all sensors. The performance of the real-time kinematic global navigation satellite system (RTK-GNSS) displacement sensor is also assessed by comparison, in the frequency domain, with accelerometer readings. Due to the vast amount of information gathered in the database with recordings from the monitoring system, some selected quantities have been chosen for analysis at the sacrifice of others. For instance, an investigation of the spreading of the wave field is not performed. According to previous studies, the spreading of the wave field does not considerably influence the response of this bridge when exposed to realistic sea states due to the small wave heights combined with the curved geometry of the structure [13]. Furthermore, response predictions or response checks are not conducted in the current paper because these topics deserve more attention for them to be beneficial to include.

2. Monitoring system

The Bergsøysund Bridge, a 931 m long, arch-shaped floating bridge, bridges the gap between Aspøya and Bergsøya on the northwestern coast of Norway. The steel superstructure rests on 7 separate light-weight concrete pontoons, as shown in the photograph in Fig. 1. The geography surrounding the bridge is shown in Fig. 2. The abutments consist of rubber bearings that support the bridge vertically and horizontally, and a steel rod on each of the ends absorbs all the axial forces. The bridge has no mooring, thus making it a particularly interesting case study: the Bergsøysund Bridge is the second-longest end-supported floating bridge in the world.

The monitoring system installed on the bridge is extensive. Sensors for environmental monitoring, consisting of 5 anemometers distributed in lampposts on top of the bridge deck and 6 wave radars distributed close to the centre of the bridge, and sensors for measuring the global response, consisting of two triaxial accelerometers on each pontoon supplemented with a global navigation satellite system (GNSS) sensor at the centre of the bridge, have been recording on site since March 2015 (sub-sets of the monitoring system have been in operation prior to this). Photographs of all the types of sensors are presented in Fig. 3. The sensor positions are shown in Fig. 4, and their accurate coordinates are listed in Table 1. Furthermore, specific details regarding the sensors are presented in Table 2. Traditionally, wind measurements are captured at 10 m above sea level. To reduce disturbances from the bridge, the anemometers are mounted approximately 8 m above the bridge deck, even though this implies a probe height of approximately 16 m.

All of the sensors on site are connected to a nearby logger unit, of which there is one on each pontoon. The logger units acquire a common time stamp for the measurements using GPS to ensure synchronous sampling. The data from the sensors

Fig. 1. The Bergsøysund Bridge. Photograph by NTNU/K.A. Kvåle.

Fig. 2. Map section showing the position of the Bergsøysund Bridge, located on the Norwegian west-coast, and the geography surrounding the bridge site. Map sections: ©Kartverket.

are delivered digitally through Ethernet and are subsequently handled internally in the logger unit. Finally, all the data from the logger units are transferred via WiFi to the main logger unit. This logger unit is connected to a router such that recordings can be accessed and the system configured externally via the Internet. All logged data are temporarily stored locally on the main logger unit. Finally, the data are pulled to an on-campus server at NTNU, with RAID storage, to ensure data redundancy. The basic workings of the system are illustrated in Fig. 5. To ensure stability of the system in the case of power outages on site, all the loggers have backup power available from batteries.

3. Data analysis

In this section, recordings made in the time span between February 2014 and January 2016 are analysed in a global manner. Some recordings were initiated due to a specified triggering value being reached, whereas others were manually initiated. To enable comparison between the statistical properties of the different measured processes, the measurement periods were restricted by the least stationary process. Typically, wave data are interpreted with periods above 30 min. In this case, however, all extracted statistics are based on 10-minute data due to the stationarity limitations of the wind process. Because the surrounding geography is complex in this case, small changes in the wind direction will greatly affect the resulting wave field. The disadvantage of using shorter periods is that it will most likely imply larger variances of the estimates. One of the main reasons for normally limiting the durations to longer periods is the number of waves required to contain the bias of the statistical estimates to acceptable levels. However, for this case study, the wave energy is located in considerably shorter wave periods than what is generally the case for offshore structures, which will ensure that the wave count is sufficient within a measurement period. The significant wave height (SWH), defined as the mean wave height of the highest third of the recorded waves, quickly converges with increasing period length for stationary wave recordings.

The standard deviations reported for accelerations correspond to the local degrees of freedom of each pontoon.

3.1. Preliminary data study

Waves are assumed to be the main excitation acting on the bridge. However, both traffic and wind excitation will also contribute to the total response of the bridge. Fig. 6a and b show the vertical acceleration recordings of pontoon 4, which are identified as traffic and wave excitations, respectively.

It is clear that the traffic-induced response is far more transient, leading to a considerably greater high-frequency content. To efficiently separate the recordings excited by traffic from those excited by waves, the following non-dimensional traffic indicator (TI) is proposed:

(a) CSI CUSP-3 accelerometer on truss. Closed protection box.

(b) CSI CUSP-3 accelerometer on truss. Opened protection box.

(c) Miros wave radar on walkway.

(d) Gill WindMaster Pro anemometer in lamp post.

(e) Trimble RTK GNSS sensor in designated pole.

Fig. 3. Sensors used in the system. Photographs by NTNU/G. Loraas/K.A. Kvåle.

$$\mathrm{TI} = \sqrt{\frac{\sum_{i=1}^{N} \sigma_{\mathrm{hp},i}^2}{\sum_{i=1}^{N} \sigma_i^2}} \tag{1}$$

where N is the number of acceleration recording channels, $\sigma_{\mathrm{hp},i}^2$ is the variance of the high-pass-filtered acceleration time series of channel i, and σ_i^2 is the variance of the unfiltered acceleration time series of channel i. By studying the frequency content of time series that are clearly wave driven or traffic driven, the assumption that all wave action is below 2 Hz was made. Thus, a high-pass filter with this cut-off frequency, intended for $\sigma_{hp,i}$, was designed. The resulting filter characteristics are presented in Fig. 7. This paper will place emphasis on the recordings where the bridge is excited mainly by waves, and the indicator is used to easily avoid data where this is not the case. Furthermore, all presented results rely on the data being low-pass filtered at 2 Hz. The low-pass filter applied is also illustrated in Fig. 7.

Traffic will primarily excite the bridge vertically or in a heave motion. By employing the TI introduced above, the standard deviation of the vertical acceleration of pontoon 2 was studied versus the SWHs of the estimates from all wave sensors, divided into groups based on the corresponding TI value. The resulting plot is shown in Fig. 8. Note that although the TI is calculated based on accelerations not being low-pass filtered, the data used to establish both the SWHs and the standard deviations of acceleration shown are low-pass filtered in the same manner as previously indicated. This implies that the effects observed on the response are low-frequency response effects; otherwise, an even more pronounced influence on the acceleration would have been expected. The recordings with a high TI value, which implies a traffic-induced response, inhabit

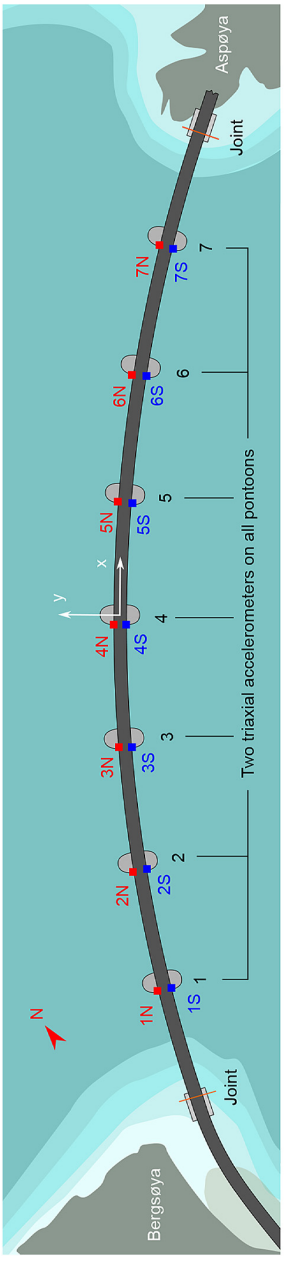

(a) View from the top, including annotations for the north direction and the global coordinate system. $z = 0$ on the bridge deck.

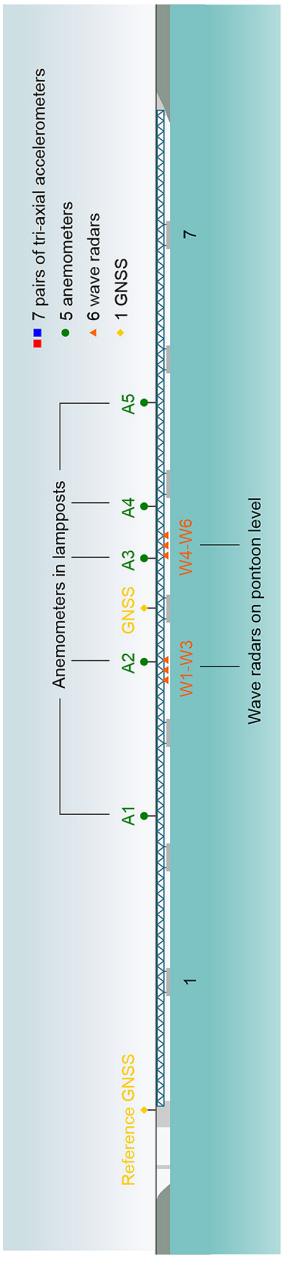

(b) View from the side.

Fig. 4. Test set-up on the Bergsøysund Bridge.

Table 1
Sensor positions.

Sensor group	Sensor	Position		
		x [m]	y [m]	z [m]
Accelerometers	1S	−318.99	−44.18	−7.00
	1N	−321.26	−35.90	−7.00
	2S	−216.35	−22.59	−7.00
	2N	−217.83	−13.92	−7.00
	3S	−112.21	−9.42	−7.00
	3N	−113.01	−0.35	−7.00
	4S	−7.21	−4.57	−7.00
	4N	−7.27	4.53	−7.00
	5S	97.74	−8.24	−7.00
	5N	98.42	0.83	−7.00
	6S	202.22	−20.28	−7.00
	6N	203.49	−11.57	−7.00
	7S	305.34	−40.79	−7.00
	7N	307.30	−32.42	−7.00
Anemometers	A1	−175.47	−6.25	8.00
	A2	−43.99	4.86	8.00
	A3	43.99	4.86	8.00
	A4	87.93	2.64	8.00
	A5	175.47	−6.25	7.50
GPS sensor	GNSS	0.00	−5.60	2.00
Wave radars	W1	−72.96	−1.05	−6.16
	W2	−52.99	−0.08	−6.16
	W3	−33.00	0.58	−6.16
	W4	33.00	0.58	−6.16
	W5	52.99	−0.08	−6.16
	W6	72.96	−1.05	−6.16

Table 2
Sensor details.

Type	Name	Placement	Sensor sample rate
Tri-axial accelerometer	CSI CUSP-3	Two on each pontoon, 14 in total	200 Hz
3D sonic anemometer	Gill WindMaster Pro	Five in different lampposts	32 Hz
Wave radar	Miros SM-140 RangeFinder	Six between pontoons 3 and 5	50 Hz
GNSS sensor	Trimble RTK GNSS	On support at Bergsøya (reference) and on centre of bridge	20 Hz

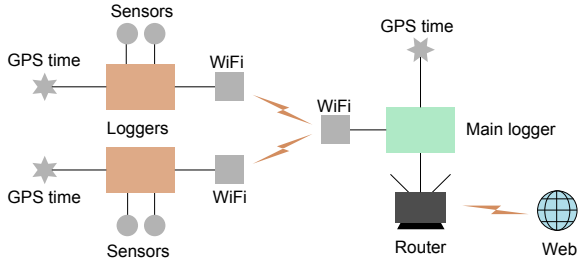

Fig. 5. Infrastructure of recording system. The system is designed and delivered by Canterbury Seismic Instruments. All the logger units are connected to a GPS antenna to ensure common time stamps for synchronous sampling.

larger vertical accelerations for low values of SWH than for low values of TI. To reduce the effects of traffic on the statistical interpretations, the records with TI > 0.6 are ignored in all of the following results.

To obtain an overview of the recordings, polar plots showing various statistical parameters plotted against the corresponding mean wind direction were created, as shown in Fig. 9. The plots are placed onto a map section to easily relate the surrounding geography to the wind directions. Note that the values for wind direction, wind speed, SWH and peak period are all spatial averages. This implies that the plotted values correspond to the averages of the statistical quantities of all sensors, of the same type, across the bridge.

The wind recordings presented in Fig. 9a reveal that the largest wind velocities are generated along the longest straits and that the 372 m tall mountain located on Aspøya efficiently blocks north-eastern winds (from 330° to 30°). The winds approaching from the coast (from 180° to 0°) are on average higher than the winds approaching from land (from 0° to 180°), but the latter subset contains the most high-wind recordings (10–20 m/s).

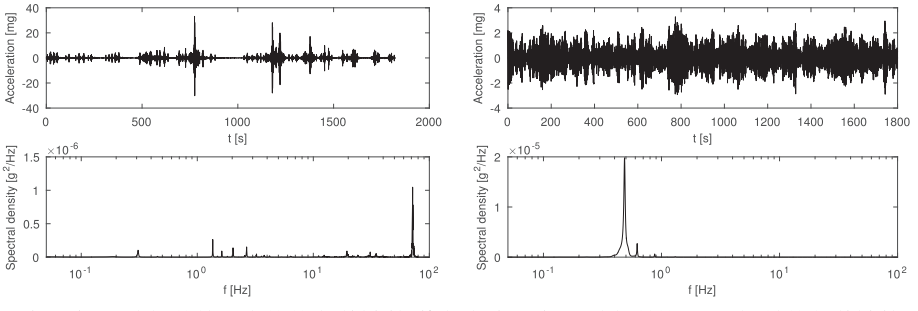

(a) Time series recorded at 09:45 on July 22, 2015, which is identified as traffic-driven excitation. $TI = 0.802$ and $H_s = 0.011$m.

(b) Time series recorded at 04:30 on December 25, 2014, which is identified as wave-driven excitation. $TI = 0.026$ and $H_s = 0.169$m.

Fig. 6. Recordings of the vertical acceleration on pontoon 4, represented both as time series and as spectral density. The frequency axis is represented logarithmically to enable identification of components of both high and low frequencies.

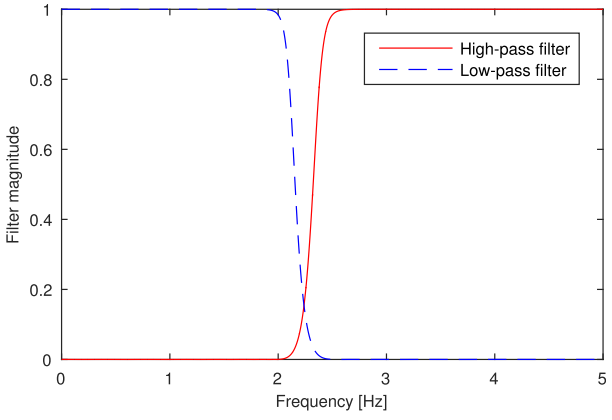

Fig. 7. Filter magnitudes of Chebyshev filters applied as low-pass and high-pass filters. The results are produced using the *cheby2* filter built into MATLAB. The applied filters are characterized by stop-band frequencies of 2.0 Hz (high-pass) and 2.5 Hz (low-pass), pass-band frequencies of 2.5 Hz (high-pass) and 2.0 Hz (low-pass), stop-band attenuation forced above 80 dB, and pass-band ripple forced below 0.2 dB.

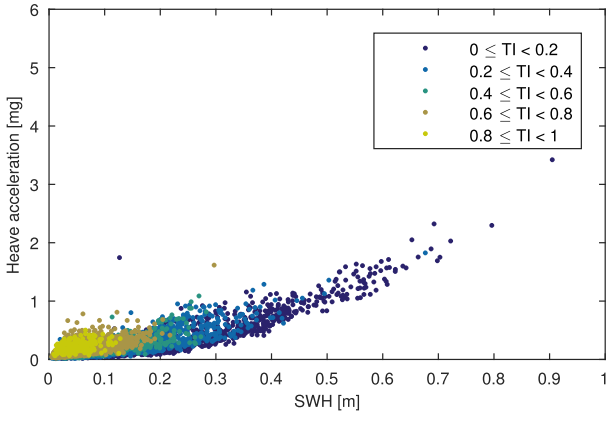

Fig. 8. Recorded standard deviations of vertical accelerations on pontoon 2 and SWH, separated into groups for different values of the traffic indicator.

The SWH was calculated for each 10-minute period of each wave sensor by employing the following well-known assumption:

$$H_s = 4\sigma_\eta \tag{2}$$

where H_s is the SWH and σ_η is the standard deviation of the sea surface elevation. Fig. 9b shows that the SWHs have a polar distribution similar to that of the mean wind speeds. The harshest wave conditions are observed when the winds are approaching from land, i.e., from 0° to 180°. Only low-height waves are expected to propagate longitudinal to the bridge, but non-negligible waves are observed for longitudinal wind directions. This result indicates that the wind direction is a less than ideal measure of the direction of the waves.

The directional effect on the standard deviations of the lateral acceleration of the midmost pontoon, shown in Fig. 9c, is even more pronounced than that for the wind speed and SWH shown in Fig. 9a and b. It is evident that the most severe lateral response is observed when the winds act perpendicular to the bridge. However, there are a considerable amount of scatter and, surprisingly, large lateral response quantities for longitudinal winds.

Fig. 9d shows that the wave peak periods are apparently evenly distributed for all wind directions. Peak periods above 5 s are estimated for some recordings but are chosen to not be represented in this plot. A more established swell-like sea state is expected to result in an increased wave peak period. Unexpectedly, no apparent relation between the mean wind direction and peak period is observed.

The wind direction is not a very good measure of wave direction due to the following two factors:

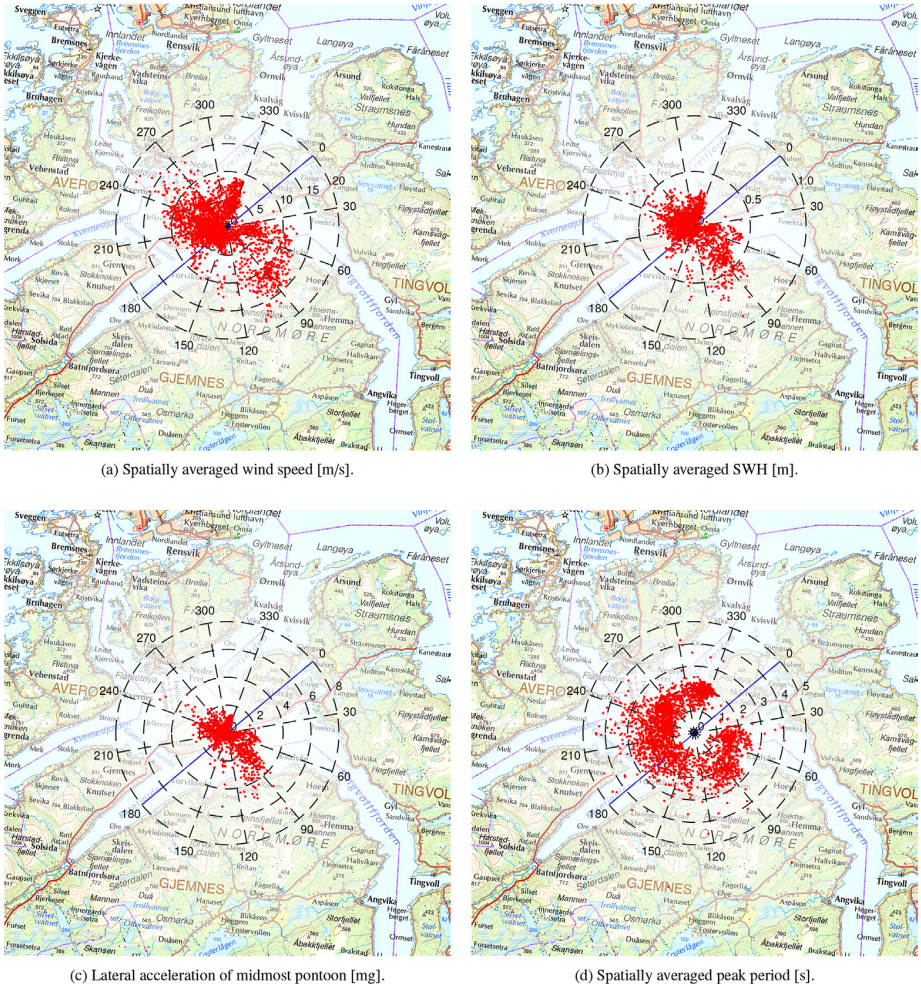

(a) Spatially averaged wind speed [m/s].

(b) Spatially averaged SWH [m].

(c) Lateral acceleration of midmost pontoon [mg].

(d) Spatially averaged peak period [s].

Fig. 9. Mean values and corresponding mean wind direction (in degrees) from ten-minute measurement periods, illustrated in polar form. Map sections: ©Kartverket.

1. The complex geography surrounding the bridge is believed to produce head sea locally across the bridge strait, even though the wave directions elsewhere are not corresponding to a head sea.
2. The waves represent a high-inertia process, and thus, the effects of changing wind will propagate slowly to the waves.

3.2. Measured excitation and response

When designing for the ULS, the long-term extreme response of the structure has to be evaluated in an appropriate manner. In the case of dynamic behaviour of the structure, it is necessary to consider the combined effects of different parameters, traditionally addressed using contour surfaces. For instance, both the peak period and the SWH need to be considered together to evaluate the effect of the waves on the response of the structure. Because both the response, by means of accelerations and displacements, and the environmental action, by means of wave heights and wind velocities, are captured, the relationship between the two is readily available for investigation.

For the critical excitation situations, the locally wind-generated waves are assumed to provide the greatest contribution. Thus, it is expected that the mean wind speed and the SWH have a clear connection. Fig. 10 shows the average of the SWHs calculated for wave sensors W3 and W4, yielding an estimate of the SWH at the location of midmost pontoon, plotted towards the average of the mean wind velocities of anemometers A2 and A3, which estimate the mean wind speed at the midspan of the bridge. As expected, there is a high correlation between wind speed and wave height. Some of the scatter shown may be

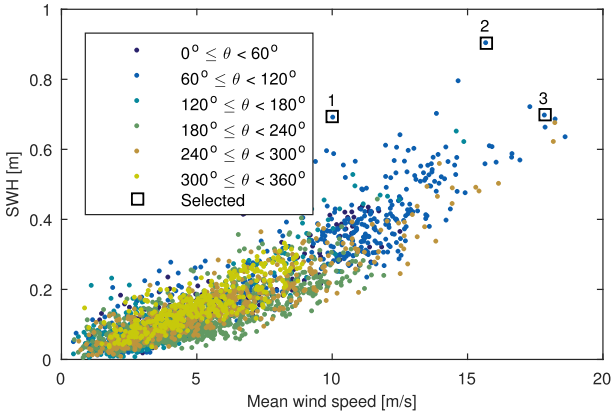

Fig. 10. Averaged SWHs of wave sensors W3 and W4 and averaged mean wind speeds of anemometers A2 and A3, separated into groups for different wind directions. Three recordings are denoted and studied in greater depth in Section 3.3.

explained by the lack of distinction between wave and wind directions. However, it is not unexpected to observe some scatter in such a plot.

The standard deviations of the vertical, lateral and torsional accelerations of the midmost pontoon are plotted versus the SWH around the centre of the bridge in Fig. 11a, b and c, respectively. The SWH is established by averaging the SWH corresponding to wave sensors W3 and W4, which are symmetrically placed about the centre. The standard deviations of the accelerations show a high sensitivity to increasing SWHs, which is an expected result and supported in Kvåle et al. [13]. By studying the different colours of the scatter points, which correspond to different ranges of wind direction, it is clear that winds approaching the bridge laterally (from 60° to 120° and from 240° to 300°) are generating a more severe sea and thus a larger response. The relatively large scatter in these figures were subjected to a more thorough investigation. The normalized range of the SWHs of the sensors on a recording was established as follows:

$$r = \frac{\max(H_s) - \min(H_s)}{\text{mean}(H_s)} \tag{3}$$

This is plotted versus the mean SWH for all recordings in Fig. 12 for different sectors of wind direction. The corresponding sectors are depicted in Fig. 13. It is clear that the inhomogeneity of the sea state, represented by SHW, is dramatically reduced as the SWH increases. Furthermore, this figure reveals that the recordings with longitudinal winds are more prone to inhomogeneity than those with lateral winds.

The relationship between wave peak period and SWH is presented in Fig. 14, in which the data points are sorted based on the corresponding mean wind velocities. When the wind speeds increase, the SWHs increase. Furthermore, the peak periods increase, and there is less scatter when the mean wind velocities increase. Fig. 14 also illustrates the relation between the measured peak period and measured SWH, which is compared with the relation given by the one-parameter Pierson-Moskowitz model [14,15]. This model has the following mathematical expression:

$$S(f) = \frac{A}{f^5}\exp\left(-B/f^4\right) \tag{4}$$

where $A = \alpha g^2(2\pi)^{-4}$, $B = 4 \cdot \alpha g^2/[(2\pi)^4 \cdot H_s^2] = 5/4T_p^{-4}$, $\alpha = 0.0081$, $g = 9.81 m/s^2$, and f is the frequency variable. This leads to the following relationship between peak period and SWH:

$$T_p = \left(\frac{5}{4}\frac{(2\pi)^4}{4\alpha g^2}\right)^{1/4} H_s^{1/2} \tag{5}$$

By investigating this figure, it is clear that the relationship set between peak period and SWH in this model overestimates the value of the peak period quite dramatically for large SWHs on the site of the bridge. Because this model is developed for offshore sites exposed to fully developed seas, this result is not unexpected. A more flexible spectral density model that incorporates more wave parameters is therefore needed.

Fig. 15 shows how the wave peak period affects the lateral response of pontoon 3 for different SWHs. This figure reveals that the response increases with increasing peak periods. This tendency applies, to some extent, for all levels of wave severities, but it is clearly more evident for the larger wave heights. As the SWH increases, the sea state is in most cases more wind generated; the swell component becomes less significant. The effect of increasing peak period on the response is

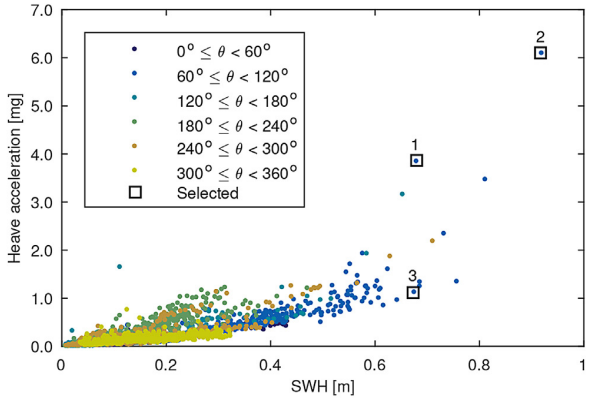

(a) Vertical acceleration.

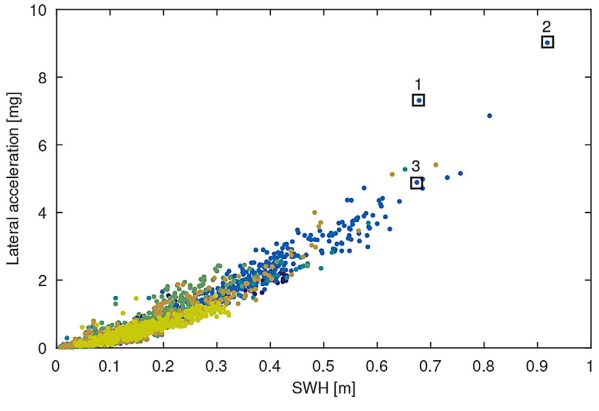

(b) Lateral acceleration.

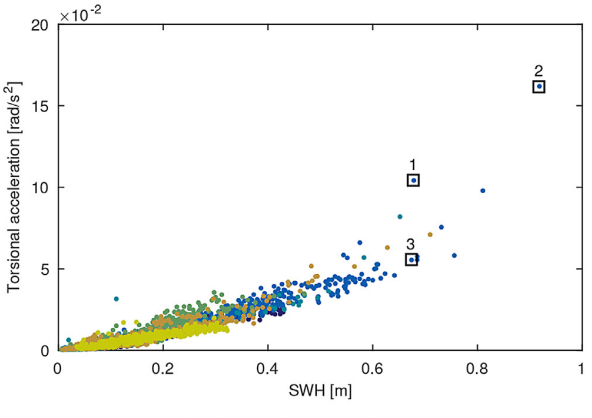

(c) Torsional acceleration.

Fig. 11. Standard deviations of accelerations of the midmost pontoon and averaged SWH between wave sensors W3 and W4. Three recordings are denoted with numbers and studied in more depth in Section 3.3.

believed to arise from the wind-generated waves, as a higher peak period is generally related to a more established and long-crested sea state. The predicted natural periods are also shown in the figure. Investigation reveals that most of the wave load acts on the bridge at periods below the first 10 analytical natural periods of the bridge. Difference-frequency effects still make resonant vibrations feasible, which is a topic recommended for further investigation. Regardless, the fact that most wave

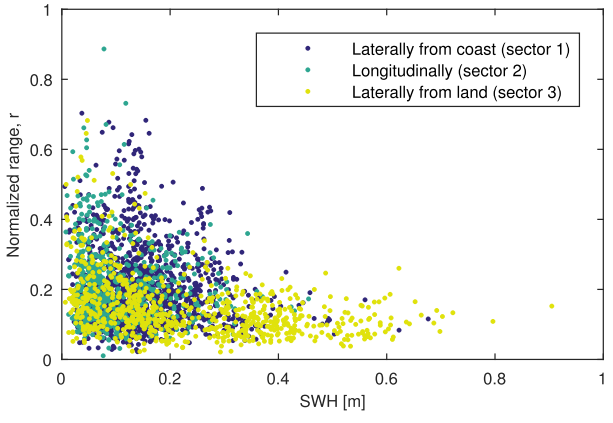

Fig. 12. Normalized range between SWHs established based on the records from all the wave sensors compared with SWH, separated into groups for different wind direction sectors. The sectors refer to the definitions presented in Fig. 13.

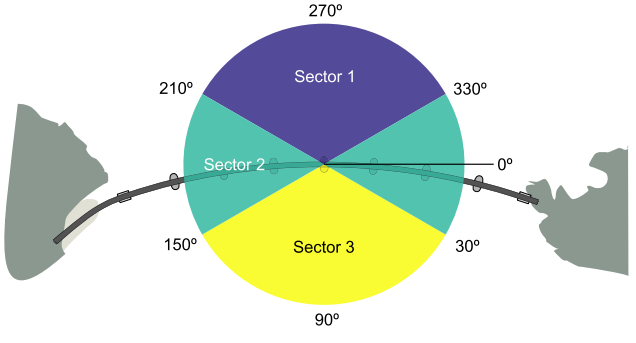

Fig. 13. Sectors corresponding to wind directions presented in Fig. 12.

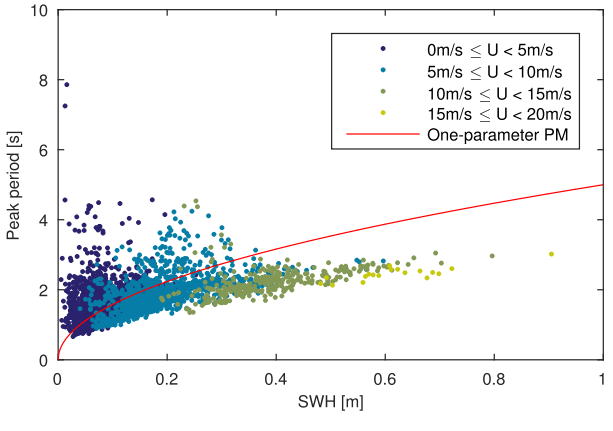

Fig. 14. Recorded peak periods and SWHs, separated into groups for different mean wind velocities, *U*. For reference, the relation given by the one-parameter Pierson-Moskowitz (PM) model is also shown here.

energy is located at frequencies above those corresponding to the first ten natural modes is highly beneficial for the performance of the bridge, due to reduced strains and displacements.

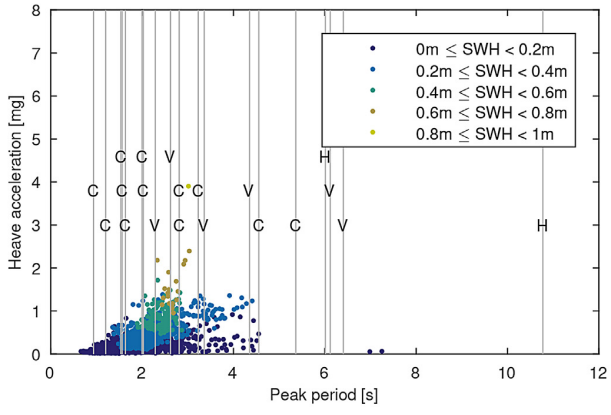

(a) Vertical acceleration of pontoon 3.

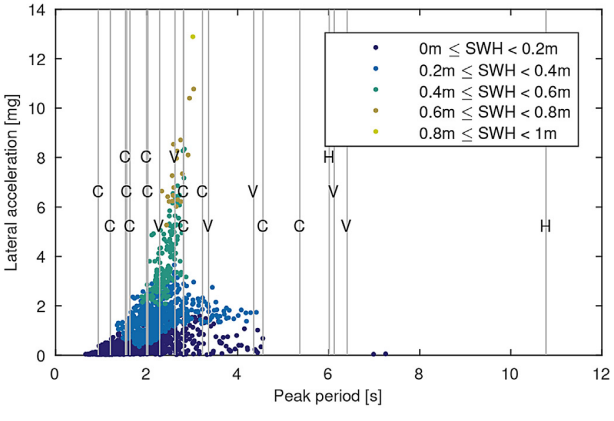

(b) Lateral acceleration of pontoon 3.

Fig. 15. Standard deviations of recorded accelerations and peak periods separated into groups for different SWHs. Grey lines denoted by letters indicate damped natural periods from a numerical prediction based on an improved version of the model presented in Ref. [13]. The letters H, V, and C denote modes with horizontal, vertical, and combinational natures, respectively.

To investigate the relationship between SWH, mean wind speed and the lateral response of the bridge, a quadratic surface was fitted to the data. This is shown in Fig. 16 for ranges of SWH and mean wind speed within the observed range during the recording period. As expected, the SWH shows the largest influence on the response, while the direct loading effect of the winds can be neglected in most cases for this structure. The scatter in the figure suggests that the SWH and the mean wind speed are not sufficient for describing the load processes acting on the bridge. A similar plot was made with SWH and peak period, which yielded similar results. The scatter indicates that there might be some parameters that are unaccounted for that affect the response of the structure.

3.3. Studies of selected recordings

Three selected recordings, denoted in Figs. 10 and 11 by squares, are studied in more depth. Table 3 summarizes the vital information regarding the recordings.

The evolutions of the wind speeds and direction through the recordings are depicted in Fig. 17. Fig. 18 shows the wave heights recorded with sensors W1-W3, as well as the corresponding spectral density estimates of all three recordings.

3.3.1. Recording no. 1

Fig. 10 reveals that the denoted third measurement period of the recording has a SWH that is too large for its wind level compared to most other recordings. Fig. 18a reveals that the sea is in build-up during this recording. The winds are approaching from approximately 15° during the first 10 min. The same first 10-minute period has a mean wind speed of approximately 8–9 m/s, which represents a rare case, based on investigation of Fig. 9a. Thereafter, a rapid change in wind

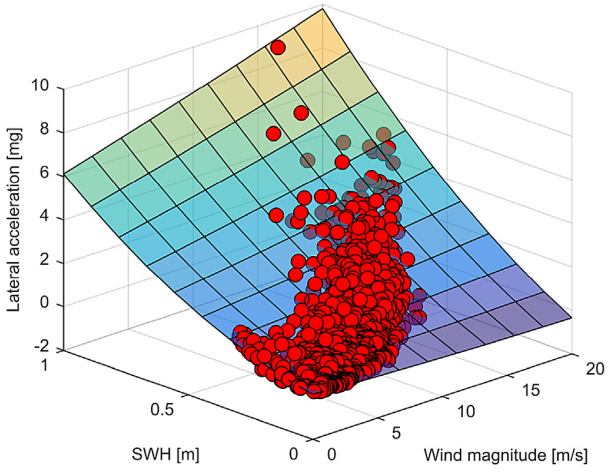

Fig. 16. Two-dimensional quadratic least-squares fit of measured data.

Table 3
Selected recordings. All recordings were made on December 30, 2015, and have durations of 30 min. Particularly interesting 10-minute periods are denoted by an asterisk. The asterisked periods correspond to the scatter points shown in Figs. 10 and 11. Statistics regarding wave and wind are spatial averages of values from all sensors. U corresponds to mean wind speed, θ corresponds to mean wind direction, and σ_l and σ_v correspond to the lateral and vertical acceleration standard deviations of pontoon 4, respectively.

No.	Time	10-minute period	Load			Response [mg]	
			SWH [m]	U [m/s]	θ [°]	σ_l	σ_v
1	03:50	0-10 min	0.29	8.70	21	1.71	0.39
		10-20 min	0.42	6.72	31	2.27	0.72
		20-30 min*	0.69	9.98	110	7.31	3.86
2	04:20	0-10 min*	0.91	15.65	101	9.02	6.10
		10-20 min	0.80	14.63	92	6.86	3.48
		20-30 min	0.71	13.84	89	5.03	2.35
3	18:25	0-10 min	0.59	16.62	104	4.25	1.01
		10-20 min*	0.70	17.82	104	4.89	1.14
		20-30 min	0.72	17.28	105	5.15	1.36

direction occurs between 15 and 22 min out in the recording. For the last 10-minute period of the recording, the winds have been blowing significantly for some time, resulting in a build-up of wave energy. This energy increase, represented by the wave height, is easily observed in Fig. 18a. However, the wind velocities have decreased as a result of fluctuating and unsettled winds. Therefore, the mean wind speed is far below normal for such severe wave action. It is also likely that winds first approaching from around 15.. during the first 10 min were causing a build-up of wave energy in the Batnfjord, which was later steered towards the bridge when the wind directions changed.

According to Fig. 11, the standard deviations of the recorded accelerations for all three components are above the trend for the given SWH. The reason for this observation is not easily found, but it might be explained by the large amount of non-stationarity inherent in the recording.

3.3.2. *Recording no. 2*

Fig. 18b shows the time series and spectral density estimates of wave radars W1, W2 and W3 for the second selected recording. The first 10-minute period of this recording recorded the largest SWHs to date in the measurement campaign, with maximum wave heights close to 1.5 m. In turn, this leads to the largest response recorded, which makes this recording of particular interest. By considering only the levels of the captured wind speeds for this recording compared to the others, shown in 17a, it is unexpected, at first glance, that the recorded waves are as severe as they are. The largest recorded wind speed is close to 20 m/s, and the mean wind speed is approximately 15 m/s. However, what is special in this case and explains this is the perfectly aligned wind directions (see Fig. 17b), both aligning the Tingvollfjord, located to the south-west of the bridge, and approaching the bridge in a close-to perfect lateral angle. This allows for the waves to build-up in the fjord and approach the bridge with few disturbances.

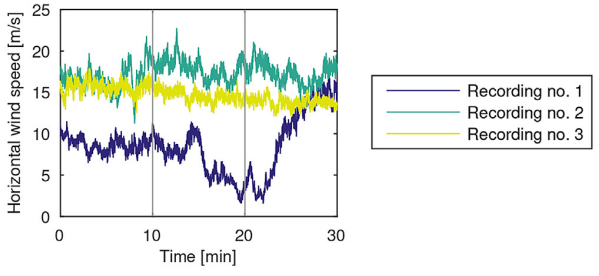

(a) Wind speeds. Vertical lines indicate 10-min period divisions.

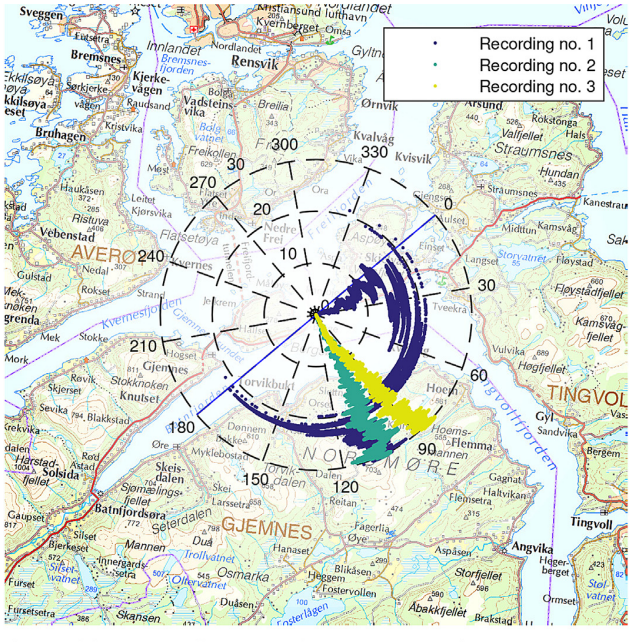

(b) Wind directions. The magnitude axis represents the time, in minutes.

Fig. 17. Time evolution of horizontal wind. The presented data are the spatial averages of data from all five anemometers.

The standard deviations of the accelerations for the denoted first 10-minute measurement period, shown in Fig. 11, are large. When taking the large SWH into account, it is not outside the expected range of variations around the trend. By investigating the spectral density estimates of displacements at midspan shown in Fig. 19, it is clear that it is highly correlated to the frequency content of the waves, as presented in Fig. 18b.

3.3.3. Recording no. 3

This recording is located within the expected range of mean wind speed and SWH. In contrast to recording no. 1, this recording shows a fairly stationary behaviour. The winds have stabilized at a high level, nearly perpendicular to the bridge, as shown in Fig. 17. Fig. 18c illustrates how this, in turn, ensures that the wave process behaves close to stationary. By comparison with the wave process and the corresponding spectral density estimates from recording no. 1, illustrated in Fig. 18a, the sea state is also considered to be both more stationary and more homogeneous.

The standard deviations of the accelerations for the denoted second 10-minute measurement period, presented in Fig. 11, are normal for this SWH. Due to the smaller and more broad-banded wave process observed in this recording, the spectral density estimate of the midspan displacement, shown in Fig. 20, reveals the modal characteristics of the system itself to a considerably greater extent than for recording no. 2.

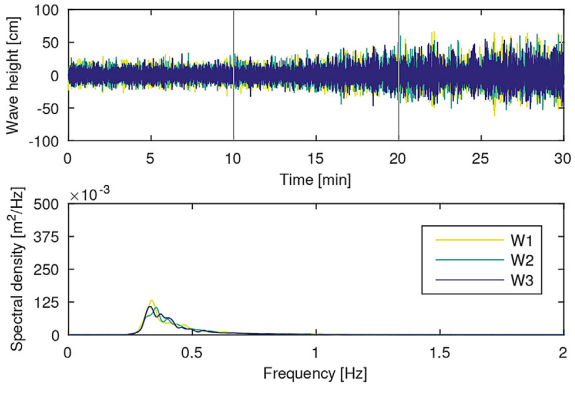

(a) Recording no. 1.

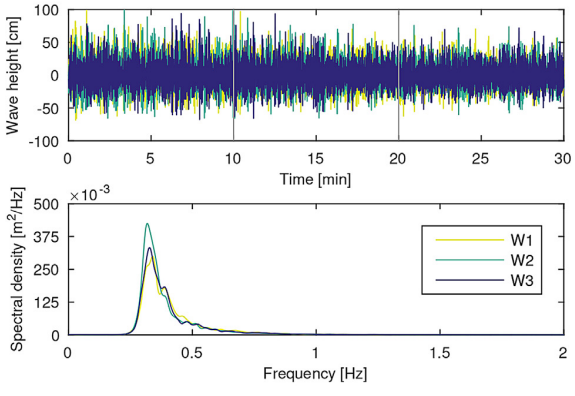

(b) Recording no. 2.

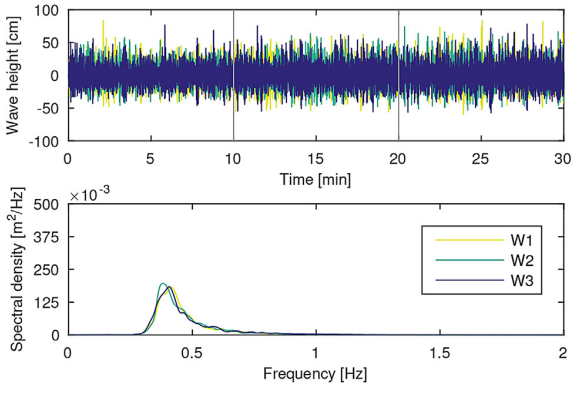

(c) Recording no. 3.

Fig. 18. Sea surface elevation from sensors W1, W2 and W3, represented both as time series and as estimates of spectral densities, from the selected recordings. The spectral density estimate is established using Welch's method, with 30 sections, 50% overlap, Hamming window, and zero-padding to ensure a finer frequency resolution. Vertical lines indicate 10-min period divisions.

3.4. Performance of GNSS sensor

The GNSS sensor is based on an RTK correction, enabling highly accurate measurements in the range of centimeters. Other similar applications of such a sensor are found in, e.g., [16, 17, 18, 19].

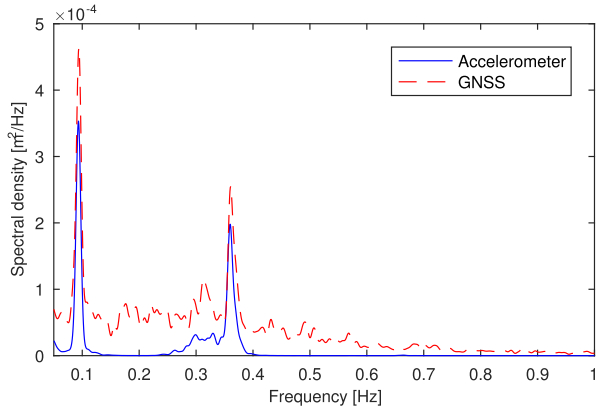

(a) Axial component.

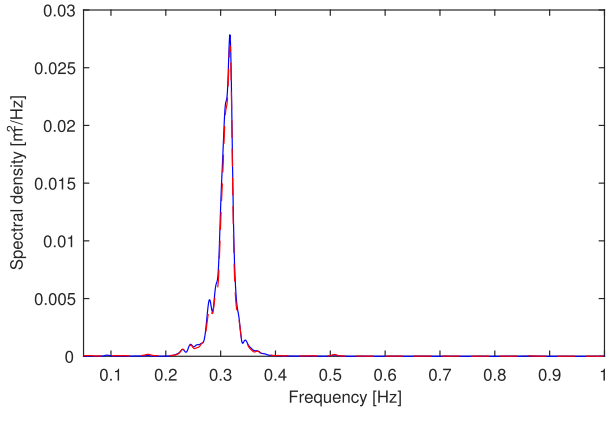

(b) Lateral component.

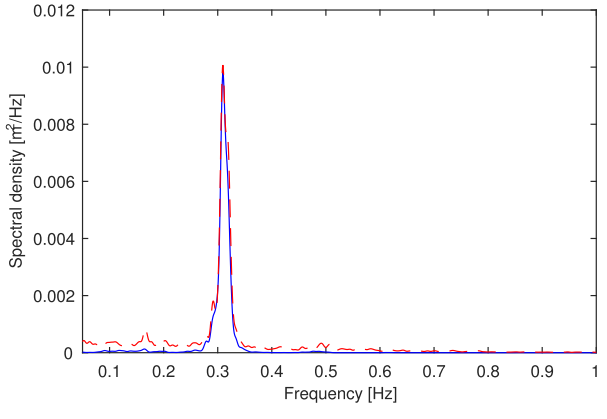

(c) Vertical component.

Fig. 19. Comparison between spectral densities from GNSS recordings and estimated displacement spectral densities from accelerations recorded with sensors 4S and 4N, corresponding to recording no. 2.

To assess the performance of the GNSS sensor on site, a comparison between the spectral density estimates of the GNSS sensor was performed using the spectral densities established from accelerometer recordings. First, the accelerations of both accelerometers on pontoon 4 were used to establish the acceleration at the position of the GNSS sensor based on rigid transformations. This accounts for all rigid rotations but assumes that the bridge is not deforming locally near the sensors.

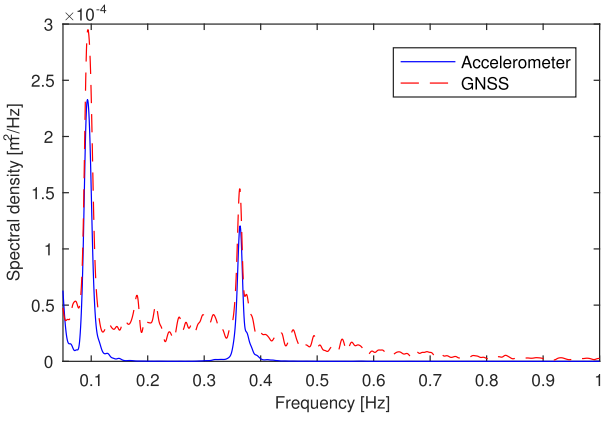

(a) Axial component.

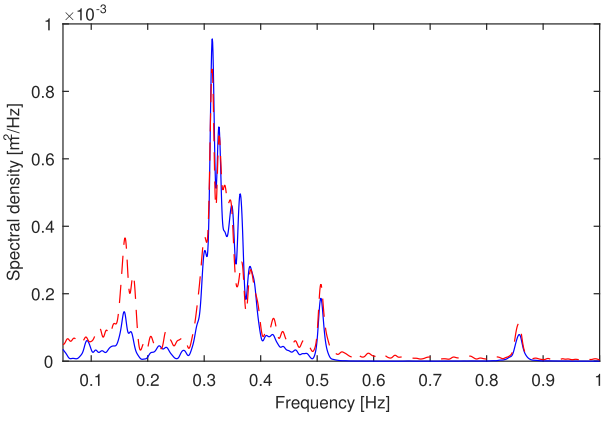

(b) Lateral component.

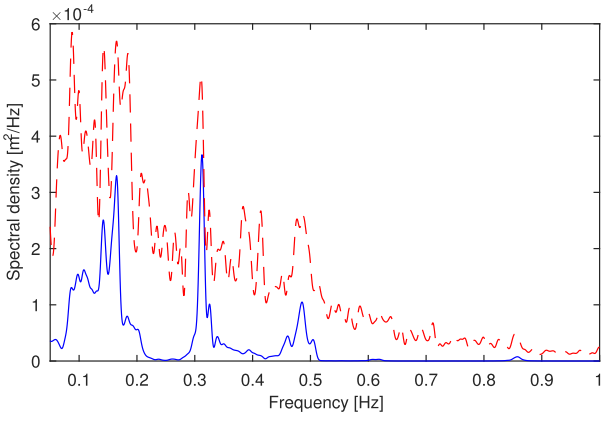

(c) Vertical component.

Fig. 20. Comparison between spectral densities from GNSS recordings and estimated displacement spectral densities from accelerations recorded with sensors 4S and 4N, corresponding to recording no. 3.

Note that the accelerometer recordings are referring to the deformed configuration, whereas the coordinates of the GNSS sensor are referring to undeformed coordinates. This will particularly affect recordings with large torsional motion. The spectral density corresponding to the acceleration, $S_{\ddot{u}\ddot{u},f,g}(f)$ in g^2/Hz, was transformed to correspond to displacement, $S_{uu,f}(f)$ in m^2/Hz, as follows:

$$S_{uu,f}(f) = g^2(2\pi f)^{-4} S_{\ddot{u}\ddot{u},f,g}(f) \tag{6}$$

Figs. 19 and 20 show the resulting plots for recordings 2 and 3, introduced in the previous section. To avoid possible issues with the amplification at low frequencies from the large negative exponent in the transfer function, the plots' frequency axes do not extend below 0.05 Hz, which is safely below the first natural frequency of the bridge. As expected, the accuracy appears to improve when the displacements are higher. The performance of the GNSS sensor is poorer for vertical displacements than for horizontal displacements, which is a well-known characteristic of the GNSS technology. The lateral displacements are fairly consistent between the spectral densities established from the accelerometers and the GNSS sensor for both benchmarked time series. It is also possible that there are differences in the fit for the two time series due to the fact that there is larger torsional motion, which will affect how well the sensor data correspond. Because the largest response contributions are lateral for the bridge, this bodes well for the application of the sensor. Caution should, however, be taken, particularly in low-excitation situations.

4. Concluding remarks

A comprehensive measurement system set up on the Bergsøysund Bridge is described in detail, including the exact sensor positions and some preliminary analyses of the collected data. The measurement system provides highly valuable data for obtaining broad insights into the dynamic behaviour of a unique bridge structure. The data are used to assess how the environmental parameters influence each other and the response of the bridge.

From a reliability perspective, a good understanding of the effect of environmental parameters on the response is essential. ULS design checks are most accurately performed using the full long-term approach, which requires a PDF that represents the environmental parameters. This is outside the scope of the current paper, but a qualitative investigation has been conducted.

As expected, the wave action is the dominating response-inducing process. A distinct relation between the SWH and the global response of the bridge was observed. However, some variations are still present; this is primarily explained by the lack of information regarding the mean wave direction. A somewhat less distinct correlation between the mean wind speed and SWH was observed; this is explained by the complexity of the surrounding geography and the large inertia of the wave process, which both lead to inconsistencies in the transfer of energy from the wind process to the wave process. Most of the wave energy is observed above the natural frequencies corresponding to the first ten fundamental modes of the bridge, which is highly beneficial for its performance, due to reduced strains and displacements.

The RTK-GNSS sensor performs well for relatively large motion when benchmarked against acceleration spectral densities converted such that they correspond to displacements. The sensor should be used with care when the response is low and particularly for vertical motion.

4.1. Future work

Verification of the calculation models for floating bridge behaviour through field measurements should be conducted. A system identification survey should also be performed. Furthermore, the effects of environmental parameters on the system identification results will provide useful insights into how the behaviour depends on weather and external factors.

Acknowledgements

The authors are grateful for the financial support from the Norwegian Public Roads Administration.

References

[1] Watanabe E. Floating bridges: past and present. Struct Eng Int 2003;13(2):128–32.
[2] Wang CM, Watanabe E, Utsunomiya T. Very large floating structures. CRC Press; 2007.
[3] Wang CM, Wang BT. Large floating structures: technological advances, vol. 3. Springer; 2014.
[4] Worden K, Farrar CR, Manson G, Park G. The fundamental axioms of structural health monitoring, Proceedings of the Royal Society of London A: Mathematical. Phys Eng Sci 2007;463(2082):1639–64. http://rspa.royalsocietypublishing.org/content/463/2082/1639.abstract.
[5] Brownjohn JMW. Structural health monitoring of civil infrastructure, philosophical transactions of the royal society of london a: mathematical. Phys Eng Sci 2007;365(1851):589–622. http://rsta.royalsocietypublishing.org/content/365/1851/589.abstract.
[6] Abdel-Ghaffar A, Scanlan R. Ambient vibration studies of golden gate bridge: I. Suspended structure. J Eng Mech 1985;111(4):463–82. http://dx.doi.org/10.1061/(ASCE0733-9399(1985)111:4(463)). http://dx.doi.org/10.1061/(ASCE)0733-9399(1985)111:4(463).
[7] Salawu O, Williams C. Review of full-scale dynamic testing of bridge structures. Eng Struct 1995;17(2):113–21. http://dx.doi.org/10.1016/0141-0296(95)92642-L. http://www.sciencedirect.com/science/article/pii/014102969592642L.
[8] Magalhães F, Cunha Á, Caetano E. Dynamic monitoring of a long span arch bridge. Eng Struct 2008;30(11):3034–44. http://dx.doi.org/10.1016/j.engstruct.2008.04.020. http://www.sciencedirect.com/science/article/pii/S0141029608001405.
[9] Langen I, Skjåstad O, Haver S. Measured and predicted dynamic behaviour of an offshore gravity platform. Appl Ocean Res 1998;20(1–2):15–26. http://dx.doi.org/10.1016/S0141-1187(98)00010-8. http://www.sciencedirect.com/science/article/pii/S0141118798000108.
[10] Naess A, Moan T. Stochastic dynamics of marine structures. New York: Cambridge University Press; 2012.
[11] Naess A, Moan T. Handbook of offshore engineering. Elsevier; 2005. http://dx.doi.org/10.1016/B978-008044381-2.50008-4. http://www.sciencedirect.com/science/article/pii/B9780080443812500084.
[12] NORSOK STANDARD N-003. Actions and action effects. 2007.

[13] Kvåle KA, Sigbjörnsson R, Øiseth O. Modelling the stochastic dynamic behaviour of a pontoon bridge: a case study. Comput Struct 2016;165:123–35. http://dx.doi.org/10.1016/j.compstruc.2015.12.009. http://www.sciencedirect.com/science/article/pii/S004579491500334X.
[14] Pierson WJ, Moskowitz L. A proposed spectral form for fully developed wind seas based on the similarity theory of S. A. Kitaigorodskii. J Geophys Res 1964;69(24):5181–90. http://dx.doi.org/10.1029/JZ069i024p05181. http://dx.doi.org/10.1029/JZ069i024p05181.
[15] Stansberg CT, Contento G, Won Hong S, Irani M, Ishida S, Mercier R, et al. The specialist committee on waves: final report and recommendations to the 23rd ITTC. In: Proceedings of the 23rd ITTC; 2002. p. 505–736. URL http://ittc.info/downloads/Proceedings/23rd_ConferenceΩ(Venice_2002)/Waves.pdf.
[16] Moschas F, Stiros S. Measurement of the dynamic displacements and of the modal frequencies of a short-span pedestrian bridge using GPS and an accelerometer. Eng Struct 2011;33(1):10–7. http://dx.doi.org/10.1016/j.engstruct.2010.09.013. http://www.sciencedirect.com/science/article/pii/S0141029610003500.
[17] Nickitopoulou A, Protopsalti K, Stiros S. Monitoring dynamic and quasi-static deformations of large flexible engineering structures with GPS: accuracy, limitations and promises. Eng Struct 2006;28(10):1471–82. http://dx.doi.org/10.1016/j.engstruct.2006.02.001. http://www.sciencedirect.com/science/article/pii/S0141029606000691.
[18] Meng X, Dodson AH, Roberts GW. Detecting bridge dynamics with GPS and triaxial accelerometers. Eng Struct 2007;29(11):3178–84. http://dx.doi.org/10.1016/j.engstruct.2007.03.012. http://www.sciencedirect.com/science/article/pii/S0141029607001320.
[19] Tamura Y, Matsui M, Pagnini L-C, Ishibashi R, Yoshida A. Measurement of wind-induced response of buildings using RTK-GPS. Journal of Wind Engineering and Industrial Aerodynamics 2002;90(12–15):1783–93. http://www.sciencedirect.com/science/article/pii/S0167610502002878.

Paper 3

Knut Andreas Kvåle, Ole Øiseth, Anders Rønnquist

"Operational modal analysis of an end-supported pontoon bridge"

Engineering Structures, vol. 148, pp. 410–423, Oct. 2017.

Engineering Structures 148 (2017) 410–423

Contents lists available at ScienceDirect

Engineering Structures

journal homepage: www.elsevier.com/locate/engstruct

Operational modal analysis of an end-supported pontoon bridge

Knut Andreas Kvåle *, Ole Øiseth, Anders Rønnquist

Department of Structural Engineering, Faculty of Engineering Science and Technology, NTNU, Norwegian University of Science and Technology, Trondheim, Norway

ARTICLE INFO

Article history:
Received 28 September 2016
Revised 23 June 2017
Accepted 27 June 2017

Keywords:
Bergsøysund Bridge
Floating bridge
Stochastic subspace identification
High damping

ABSTRACT

A comprehensive monitoring system is installed and currently in operation on the Bergsøysund Bridge, an end-supported floating pontoon bridge, collecting data on accelerations, displacements, waves, and wind. Using covariance-driven stochastic subspace identification (Cov-SSI), data-driven stochastic subspace identification, and frequency domain decomposition, the modal parameters of the structure are estimated to investigate its dynamic behaviour. Aspects regarding the selection of good parameters for the Cov-SSI analyses are highlighted, and the clarifying effect of applying stabilization criteria on multiple orders of output is discussed. The effects of the significant wave height on the modal parameters are investigated based on an automatic selection of stable poles from stabilization plots produced by the Cov-SSI method.

1. Introduction

Floating bridges of various designs have existed for approximately four millennia, according to [1]. However, only in recent decades have such bridges been used in modern infrastructure applications. More crossings may potentially take advantage of floating bridges.

In an international context, the continuous pontoon girder is by far the most common type of floating bridge. Such bridges are generally side supported by anchoring to the seabed, which drastically reduces their flexibility. For some crossings, bridges based on continuous pontoon girders or anchoring are not feasible or beneficial. The crossings planned for the ferry-free Coastal Highway E39, located on the northwestern coast of Norway, are examples of such crossings. The deep fjords make side anchoring to the seabed practically impossible. Furthermore, the requirement that ships should be able to pass through makes a discretely distributed pontoon solution more obvious. Worldwide, only two long-span end-supported floating bridges exist: the Bergsøysund Bridge and the Nordhordland Bridge. Both of these bridges are located on the western coast of Norway, and both rely on discretely distributed pontoons.

The traditional method for dynamic testing is based on estimating the frequency response function matrix, which requires monitoring of both the force and the response quantities. Structures under operation are, however, more commonly studied based on ambient vibrations alone, referred to as operational modal analysis (OMA) or output-only system identification. Since the crude, yet effective, peak-picking study performed on the Golden Gate Bridge by McLamore et al. [2], the research field concerning the OMA of civil structures has experienced significant development. The number of available methods for OMA is continuously increasing, with the acronyms FDD, SSI, ARMA, SOBI and NExT representing some of the most well-known methods. In the works by [3–9], system identification techniques are applied on civil structures, and the performances of the methods are compared. Generally, OMA methods are applied to lightly damped structures. When system identification is to be attempted on a floating bridge, which due to the fluid-structure interaction observes high damping levels, the following question emerges: are the modal analysis methods suitable for a floating bridge?

Answering the above question is the main objective of this paper. Using a state-of-the-art measurement system, the dynamic behaviour of the Bergsøysund Bridge is studied. Both environmental actions, in terms of wind and wave excitation, and global response, in terms of accelerations and displacements, are recorded, and their relationship is investigated. In this regard, the effects of wave and wind conditions on modal parameters are of particular interest. Temperature effects are considered to be beyond the scope of the current paper. The effect of changing temperature has been thoroughly investigated in the literature [6,10,11].

Modal identification using covariance-driven stochastic subspace identification (Cov-SSI) on recordings from the Bergsøysund Bridge was also the topic of the conference paper by Kvåle et al. [12]. It was concluded that the identified parameters, corresponding to the lowest modes of the structure, were in decent agreement

* Corresponding author.
E-mail address: knut.a.kvale@ntnu.no (K.A. Kvåle).

http://dx.doi.org/10.1016/j.engstruct.2017.06.069
0141-0296/

with the initial numerical predictions of frequency and damping and below satisfactory for mode shapes. The sensitivity of the input parameters to the results, particularly the number of time lags, was very large, and considerable tweaking of the selected values was required. This situation is also known and well reported in literature, see e.g., [13,11].

The current study addresses many of the above highlighted issues and is also far more extensive than the mentioned conference paper. Furthermore, this study relies on an extended monitoring system, including environmental monitoring. The stabilization criterion is required to be fulfilled for multiple preceding poles, to clarify the stabilization plots such that the selection of stable and physical poles is more robust. By automating the selection of modal parameters, the effects of environmental parameters on the modal quantities are studied based on a large pool of recordings.

2. Theoretical outline

2.1. Numerical prediction of modal parameters

For comparison with the predicted modal quantities of the floating bridge, some operations on the system model matrices are needed. The mathematical and numerical model is identical to the one presented in Kvåle et al. [14]. For the convenience of the reader, the most important details are repeated in the following. The goal is to establish a frequency-domain equation of motion to obtain an easily solvable eigenvalue problem. The starting point is the time-domain generic equation of motion, written as follows within the framework of the finite element method (FEM):

$$[M_s]\{\ddot{u}(t)\} + [C_s]\{\dot{u}(t)\} + [K_s]\{u(t)\} = \{p_h(t)\} \tag{1}$$

Here, t represents the time; $[M_s]$, $[C_s]$, and $[K_s]$ are the structural mass, damping and stiffness matrices, respectively; $\{u(t)\}$ is the displacement vector; and $\{p_h(t)\}$ is the total hydrodynamic action, which includes both wave excitation and fluid-structure interaction. The fluid-structure interaction can be treated as frequency-dependent contributions to the system mass and damping and as a constant contribution to the system stiffness. This treatment results in the following equation of motion, represented in the hybrid frequency-time domain:

$$[M(\omega)]\{\ddot{u}(t)\} + [C(\omega)]\{\dot{u}(t)\} + [K]\{u(t)\} = \{p(t)\} \tag{2}$$

Here, the total system matrices, including the fluid-structure interaction contributions, namely, $[M(\omega)]$, $[C(\omega)]$, and $[K]$, are used. The wave excitation vector is denoted as $\{p(t)\}$. From this, the following complex eigenvalue problem is established:

$$(\lambda^2[M(\omega)] + \lambda[C(\omega)] + [K])\{u\} = \{0\} \tag{3}$$

where the eigenvalue λ is introduced. The general complex eigenvalue problem is typically solved using a state-space formulation, as in this work. Clearly, cf. Eq. (3), the eigenvalue problem is frequency dependent. To accommodate this, an iterative algorithm, represented by the pseudo-code in Table 1, is used.

Note that the estimated numerical solutions to the eigenvalue problem presented in [14] have been re-estimated due to a model update in [15]. The latter estimates are used as a reference in this paper.

2.2. Modal identification

2.2.1. Frequency domain decomposition

The simple and effective improvement of the peak-picking method, based on singular value decomposition (SVD), was presented, in its current form, by Brincker et al. [16,17]: the frequency domain decomposition (FDD). To some extent, this can remedy difficulties from closely spaced modes but stays true to the simple and tangible interpretation that follows the peak-picking method. This makes it an ideal method to supplement more sophisticated methods that often suffer from less graspable interpretations.

Table 1
Pseudo-code of the iterative algorithm used to solve the eigenvalue problem [14].

INPUT N, *tolerance*

FOR n = 1 to 2 N
  $\omega = 0$
  $\Delta =$ tolerance $+ 1$
  WHILE $\Delta >$ tolerance
    Solve eigenvalue problem for chosen $\omega \Rightarrow \lambda_r$ and $\{q_r\}$
    Sort λ_r, and correspondingly sort $\{q_r\}$
    $\omega_0 = \omega$
    $\omega = |\lambda_n| \quad (n = r)$
    $\Delta = |\omega_0 - \omega|$
  END
  Store eigenvalue $\lambda_n = \lambda_r$ and eigenvector $\{q_n\} = \{q_r\}$
END

2.2.2. Covariance-driven stochastic subspace identification

The stochastic subspace identification methods are highly sophisticated techniques and are considered to be among the most robust and accurate methods available [3,4]. The Cov-SSI method enables the identification of a stochastic state-space model based on response measurements only. The following presentation, which summarizes the main elements of the algorithm, is based on Hermans and van Der Auweraer [18].

First, assume the following stochastic and discrete state-space model representing the considered dynamical system:

$$\{z_{k+1}\} = [A]\{z_k\} + \{w_k\} \tag{4}$$

$$\{y_k\} = [C]\{z_k\} + \{v_k\} \tag{5}$$

where $\{z_k\}$ and $\{y_k\}$ are the state vector and output vector, respectively, and $\{w_k\}$ and $\{v_k\}$ are noise terms. The sub-indices correspond to discrete time sample numbering, related to the time through $t = (k-1)f_s^{-1}$, where f_s is the sampling frequency. Furthermore, $[A]$ is the state matrix and $[C]$ is the output matrix.

The recorded data are arranged in a matrix $[Y]$ as follows:

$$[Y] = \begin{bmatrix} \{y_1\}^T \\ \{y_2\}^T \\ \vdots \\ \{y_N\}^T \end{bmatrix} \tag{6}$$

The data have l channels and N samples, such that $[Y]$ has dimensions Nxl. In Cov-SSI, the discrete correlation matrix is an essential starting point. The discrete correlation matrix at time lag $\Delta t = kf_s^{-1}$ is defined as follows:

$$[R_k] = E\left(\{y_{n+k}\}\{y_n\}^T\right) \tag{7}$$

The discrete cross-correlation matrix is estimated by employing FFT and IFFT transforms, as implemented in the MATLAB function `xcorr`, without normalisation.

The correlation matrices are subsequently arranged as submatrices in a block-Hankel matrix, where $2i-1$ is the maximum number of time lags, as follows:

$$[H_i] = \begin{bmatrix} [R_1] & [R_2] & \dots & [R_i] \\ [R_2] & [R_3] & \dots & [R_{i+1}] \\ \vdots & \vdots & \ddots & \vdots \\ [R_i] & [R_{i+1}] & \dots & [R_{2i-1}] \end{bmatrix} \tag{8}$$

As an alternative to the block-Hankel matrix, a matrix with correlation matrices stacked in a block-Toeplitz manner can be used, as is the case in, e.g. [19]. The following expressions are equally valid for both choices, but the block-Hankel stacking is used in the current paper. The block-Hankel matrix shown in Eq. (8) can be decomposed into its observability matrix, $[\mathcal{O}_i]$, and controllability matrix, $[\mathcal{C}_i]$:

$$[H_i] = [\mathcal{O}_i][\mathcal{C}_i] \tag{9}$$

which are defined as:

$$[\mathcal{O}_i] = \begin{bmatrix} [C] \\ [C][A] \\ [C][A]^2 \\ \vdots \\ [C][A]^{i-1} \end{bmatrix}, \quad [\mathcal{C}_i] = \begin{bmatrix} [G] & [A][G] \dots [A]^{i-1}[G] \end{bmatrix} \tag{10}$$

The matrix $[G]$ is the cross-correlation matrix between the one-sample-shifted state vector and the output vector, defined as follows:

$$[G] = E\left(\{z_{n+1}\}\{y_n\}^T\right) \tag{11}$$

The block-Hankel matrix is pre- and post-multiplied with weighting matrices and decomposed using SVD, as follows:

$$\begin{aligned}[W_1][H_i][W_2]^T &= \begin{bmatrix} [U_1] & [U_2] \end{bmatrix} \begin{bmatrix} [\Sigma_1] & [0] \\ [0] & [0] \end{bmatrix} \begin{bmatrix} [V_1]^T \\ [V_2]^T \end{bmatrix} \\ &= [U_1][\Sigma_1][V_1]^T \end{aligned} \tag{12}$$

In practical cases, there will be more non-zero singular values than what is expected for the value of the system order, and thus, input orders have to be specified manually, corresponding to the number of singular values to include in $[\Sigma_1]$. This selection directly affects the resulting eigenvalues and eigenvectors. The selection of an appropriate order is difficult, and therefore, a *stabilization plot* is used to separate physical eigenvalues from spurious ones by estimating the modal parameters for a range of orders. A pole is deemed stable when some criteria for maximum deviance of damping, frequency and mode shape between different values for the system order are fulfilled. This process is described in detail in Section 2.3.

The matrices $[W_1]$ and $[W_2]$ are introduced to improve the identification of poorly excited modes. If the weights are set to identity matrices, this implies no weighting or balanced realisation (BR) weighting. The other weighting considered herein is the canonical variate analysis (CVA) weighting. For a mathematical description of the functioning of the CVA weighting, the reader is referred to [18].

Finally, the state matrix is computed as follows:

$$[A] = [\mathcal{O}_{\text{down}}]^{\dagger}[\mathcal{O}_{\text{up}}] \tag{13}$$

where $[\mathcal{O}_{\text{down}}]$ and $[\mathcal{O}_{\text{up}}]$ are obtained by removing the first or last l rows from $[\mathcal{O}_i]$, respectively, and $\dagger$ denotes the pseudo-inverse. The output matrix $[C]$ is obtained by extracting the first l rows from $[\mathcal{O}_i]$, as follows:

$$[C] = [\mathcal{O}_i]_{1:l} \tag{14}$$

The estimated state matrix, $[A]$, then undergoes an eigenvalue decomposition to yield the discrete system poles, $\hat{\lambda}_r$, and system eigenvectors $\{\psi\}$. These are converted to continuous system poles, λ_r, and eigenvectors corresponding to the sensor coordinates, $\{\phi\}$, as follows:

$$\lambda_r = \exp\left(\hat{\lambda}_r f_s^{-1}\right) \tag{15}$$

$$\{\phi\} = [C]\{\psi\} \tag{16}$$

2.2.3. Data-driven stochastic subspace identification

The reader is referred to Van Overschee and de Moor [20] for a comprehensive description of the aspects of the data-driven stochastic subspace identification (Data-SSI) method. For all analyses with the Data-SSI method performed in the current paper, *UPC* weighting is utilized in conjunction with *Algorithm 2* [20].

As concluded in the following sections of the paper, the Cov-SSI method is found to be the most robust and accurate method for the purpose of this paper. The mathematical foundation underlying the Data-SSI method is therefore not presented here, and the reader is referred to the cited literature.

2.3. Stabilization criteria and selection of poles

The poles estimated from the SSI algorithms undergo scrutiny from stabilization criteria to assist in distinguishing between physical and spurious modal estimates.

For the order n^*, the resulting poles m^* are compared to all the poles from preceding orders $n = n^* - \sigma$, where $\sigma = 1, 2, \dots, s$ and s is an integer defining the required stability level. The pole m from order n that maximizes the value of a modal indicator, the modal assurance criterion (MAC) number here, is then assumed to correspond to pole m^* in order n^*. The MAC number between complex-valued poles m^* and m is defined as follows [21,22]:

$$\text{MAC}_{m,m^*} = \frac{|\{\phi_{m^*}\}^T\overline{\{\phi_m\}}|^2}{\{\phi_{m^*}\}^T\overline{\{\phi_{m^*}\}} \cdot \{\phi_m\}^T\overline{\{\phi_m\}}} \tag{17}$$

where $\overline{\{\phi\}}$ corresponds to the complex conjugate of $\{\phi\}$. In simple cases, the natural frequency may be used as a modal indicator, but for cases where the modes are closely spaced in frequency, such as for this case study, the MAC number is considered to be a better choice.

The deviance of certain target quantities between the poles in orders $n = n^* - \sigma$ and the corresponding poles for order n^* are used to check the stability of pole n^* up to the required stability level s by requiring that the following criteria are satisfied:

- $|f_{n^*,m^*} - f_{n,m}|/f_{n^*,m^*} \leqslant C_f$
- $|\xi_{n^*,m^*} - \xi_{n,m}|/\xi_{n^*,m^*} \leqslant C_\xi$
- $\text{MAC}(\{\phi_{n^*,m^*}\}, \{\phi_{n,m}\}) \geqslant C_{\text{MAC}}$

In the current study, the criterion values and the stability level were selected as indicated in Table 2. Traditionally, the poles deemed as stable are then plotted in a stabilization plot to separate the spurious modes from the physical ones.

3. The Bergs⊘ysund Bridge

The Bergsøysund Bridge is a 931 m long, curved floating bridge that stretches between Aspøya and Bergsøya on the northwestern coast of Norway (see Fig. 1). Seven separate light-weight concrete pontoons support the steel superstructure, as is depicted by the photograph in Fig. 2. Rubber bearings support the bridge vertically and horizontally at the abutments, and a steel rod on each of the

Table 2
Parameters used for the selection of stable poles.

Parameter	Value
Frequency deviance, C_f	1%
Damping deviance, C_ξ	5%
MAC threshold, C_{MAC}	95%
Stability level, s	8

Fig. 1. Map section showing the geography around the bridge site. ©Kartverket.

Fig. 2. The Bergsøysund Bridge. Photograph by NTNU/K.A. Kvåle.

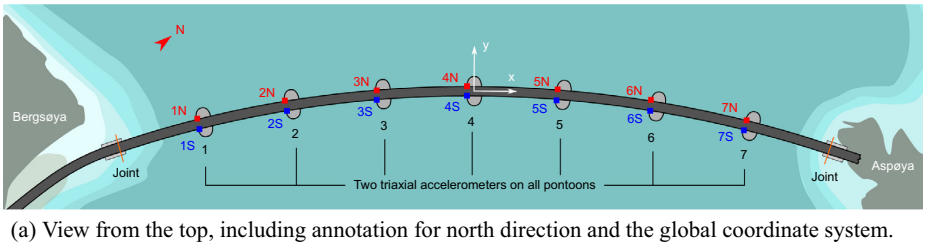

(a) View from the top, including annotation for north direction and the global coordinate system.

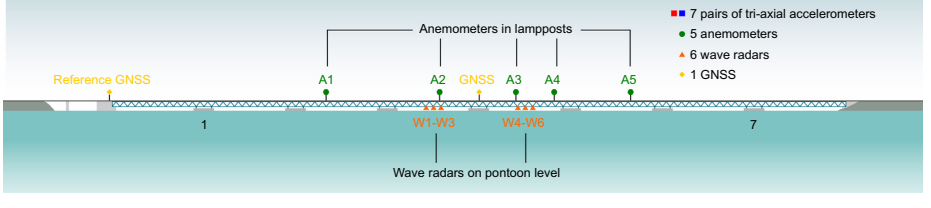

(b) View from the side.

Fig. 3. Test set-up on the Bergsøysund Bridge. Reproduced from [23] with permission from Elsevier.

Table 3
Thirty-minute statistics of the selected recordings. The reported accelerations are standard deviations. SWH refers to the significant wave height around pontoon 4 based on an average from wave radars W3 and W4, U is the horizontal mean wind speed close to the centre of the bridge based on an average from anemometers A2 and A3, and θ is the direction of origin of the mean wind. All quantities are based on data low-pass filtered at 2 Hz (see [23] for filter specifics). The recording time is reported in local time. TI is used as an abbreviation for the traffic indicator, which indicates the relative high-frequency content of all accelerations.

			Accelerations of pontoon 4, [mg]						
Characteristic	Recording date	Recording time [hh:mm]	Longitudinal (x)	Lateral (y)	Vertical (z)	SWH [cm]	U [m/s]	θ [°]	TI
Low-level response	May 5, 2015	03:14 (GMT + 2)	0.01	0.14	0.04	2.0	2.1	109	0.04
Traffic-induced response	May 18, 2015	07:03 (GMT + 2)	0.17	0.12	0.31	2.4	1.3	87	0.64
Wave-induced response	December 30, 2015	04:20 (GMT + 1)	1.10	7.12	4.26	82.3	14.6	94	0.03

ends absorbs axial forces. No mooring is supporting the bridge, which makes it a particularly interesting case study.

3.1. Structural monitoring system

The monitoring system is described in detail in [23], but the most important details are repeated below for the convenience of the reader. Five anemometers distributed in lampposts on the top of the bridge deck and 6 wave radars distributed close to the centre of the bridge are monitoring the environmental action, while two triaxial accelerometers on each pontoon (14 in total), supplemented with a global navigation satellite system (GNSS) sensor at the centre of the bridge, are monitoring the response of the bridge. The sensor layout is depicted in Fig. 3.

4. Analysis

In this section, the modal identification techniques are applied to selected acceleration recordings. There are a total of 6210 recordings made in the time span between November 2014 and January 2017, of which 1679 include sensors for environmental monitoring and all 14 accelerometers. All of these recordings had durations of approximately 30 min. The recordings were resampled to 2 Hz after applying a suitable low-pass filter, prior to the identification. Three different characteristics are sought in the pool of recordings to be selected for modal analysis:

1. Low-level response (and excitation)
2. Traffic-induced response
3. Wave-induced response

By investigating these three principally different scenarios, a better understanding of how different loading situations affect the results will hopefully be obtained. Therefore, the starting point was some assessment of the overall statistics of the recordings made to identify such recordings. The wind direction is close to constant at a lateral angle for all three cases. The tools and results presented in Kvåle et al. [23] are used to isolate selected recordings. The traffic indicator (TI) introduced in that work is utilized to indicate the level of traffic proportion of the response, which is defined as follows:

$$\mathrm{TI} = \sqrt{\frac{\sum_{r=1}^{l} \sigma_{\mathrm{hp},r}^2}{\sum_{r=1}^{l} \sigma_r^2}} \tag{18}$$

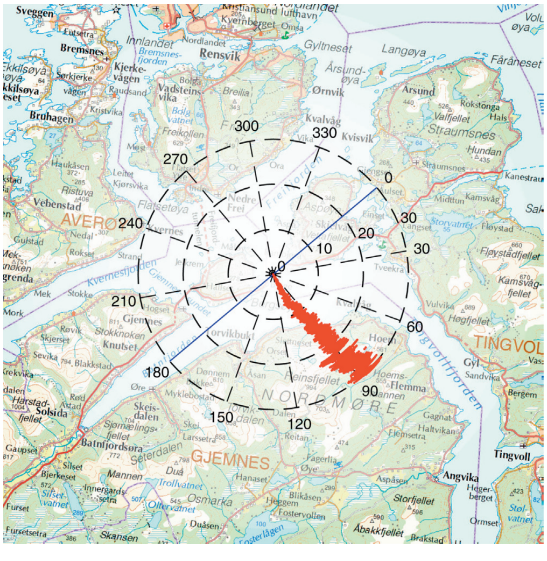

Fig. 4. Wind direction time evolution for wave-driven recording. The blue line indicates the tangent at the midspan of the bridge. The plotted wind direction corresponds to the average of anemometers A2 and A3, and indicates the origin of the wind. The amplitude axis corresponds to the time in minutes. (For interpretation of the references to colour in this figure legend, the reader is referred to the web version of this article.)

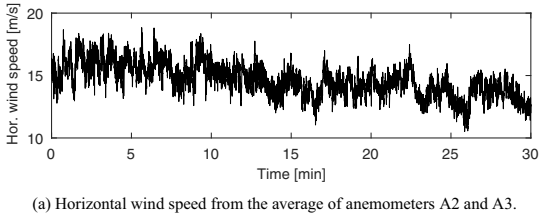

(a) Horizontal wind speed from the average of anemometers A2 and A3.

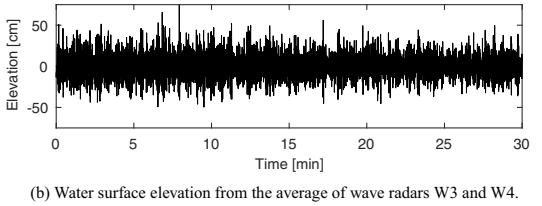

(b) Water surface elevation from the average of wave radars W3 and W4.

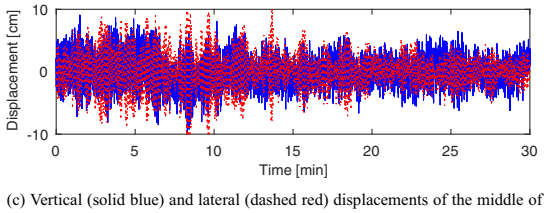

(c) Vertical (solid blue) and lateral (dashed red) displacements of the middle of the bridge obtained from the GNSS sensor.

Fig. 5. Time series from the selected wave-driven recording.

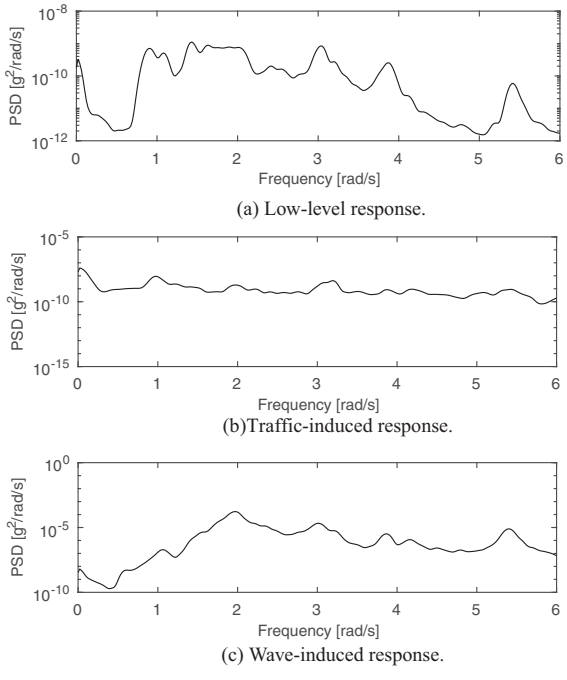

Fig. 6. Welch estimates of power spectral densities of the lateral acceleration of the midmost pontoon for the three chosen recordings. 20 divisions, which are padded by zeros on both sides such that the total length is tripled, are used for the estimates. For reference, the signal-to-noise ratio of the sensor is specified as 130 dB, the dynamic range as 114 dB, and the range as ±4 g.

where σ_r^2 is the variance of channel r and $\sigma_{\text{hp},r}^2$ is the corresponding variance from accelerations high-pass filtered at 2 Hz. Table 3 presents the vital information about the three selected recordings, to illustrate the differences between the selected recordings.

The *significant wave height* (SWH) is used as a characteristic measure of the wave height. The SWH is defined as the mean wave height of the highest third of the recorded waves, and it is estimated using the following well-known assumption:

$$H_s = 4\sigma_\eta \tag{19}$$

where σ_η is the standard deviation of the water surface elevation $\eta(t)$. This is valid when the wave height is assumed to be a Gaussian process, which is assumed for all analyses presented in the current paper.

The wind direction of the wave-driven recording is close to perpendicular to the bridge throughout the duration (Fig. 4). Fig. 5 shows the time histories of the horizontal wind speed, the water surface elevation and the displacements at the mid-span of the recording. This figure indicates that the excitation and response recordings are of good quality and that it is sufficiently stationary. The power spectral densities (PSDs) of the lateral acceleration of the midmost pontoon are estimated using Welch's method for assessing the frequency content of the response in the recordings (Fig. 6). This figure illustrates that the degree of high-frequency content is much larger in the traffic-driven recording.

4.1. Case-specific identification challenges

The success of a modal identification on the case structure is considered to be challenging due to the following aspects:

- modes are very closely spaced in frequency
- modes have high damping levels
- high degree of influence from external factors

This type of modal analysis therefore requires much from both the identification algorithm and from the operator. The algorithm has to address closely spaced modes, which at the same time have large damping, at least in the context of traditional OMA of civil structures. In addition, a floating bridge will be highly prone to external influences, making the modal parameters dependent on the environmental conditions.

4.2. Identification of modal parameters

The three selected recordings (see Table 3) were used as the basis for modal identification with the following three algorithms:

Table 4
Modal parameters identified from the wave-driven recording by manual selection. The following abbreviations are used: H (horizontal), V (vertical), and T (torsional). Note that the analytic values are obtained using the methodology presented in [14] but with an updated model [15].

	Frequency [rad/s]				Damping ratio [%]			MAC (with analytic)		
	Analytic	Cov-SSI	Data-SSI	FDD	Analytic	Cov-SSI	Data-SSI	Cov-SSI	Data-SSI	FDD
1 (H)	0.58	0.59	0.59	0.61	1.63	1.73	1.58	1.00	0.99	0.99
2 (V)	0.99	1.03	–	–	12.25	6.67	–	0.80	–	–
3 (V)	1.03	1.00	–	–	11.24	14.35	–	0.82	–	–
4 (H)	1.05	1.09	–	–	5.00	3.84	–	0.78	–	–
5 (V/H)	1.17	1.22	–	–	7.67	5.43	–	0.92	–	–
6 (H/T)	1.38	–	1.49	–	5.91	–	3.17	–	0.76	–
7 (V)	1.44	1.49	–	–	3.28	2.41	–	0.72	–	–
8 (V)	1.87	–	–	–	1.07	–	–	–	–	–
9 (T/H)	1.95	1.99	–	–	3.62	2.49	–	0.91	–	–
10 (H/T)	2.23	2.31	2.31	–	0.43	2.43	2.17	0.88	0.81	–
11 (T/H)	2.24	–	–	–	3.98	–	–	–	–	–
12 (V)	2.40	2.48	2.48	–	0.35	0.56	0.35	0.92	0.90	–
13 (V)	2.75	2.87	2.86	–	0.29	0.52	0.45	0.74	0.76	–
14 (T/H)	3.10	3.19	3.20	–	0.38	0.90	0.55	0.97	0.89	–
15 (H/T)	3.15	3.03	3.04	3.04	1.29	1.92	1.53	0.97	0.97	0.94
16 (H/T)	3.84	3.63	3.63	3.66	0.72	1.15	1.01	0.99	0.99	0.99
17 (T/H)	4.02	4.17	4.14	4.20	0.29	0.53	0.86	0.98	0.99	0.98
18 (H/T)	4.09	3.86	3.85	3.88	0.59	0.82	0.81	0.99	0.98	0.99
19 (H/T)	5.22	5.40	5.37	5.42	0.35	0.77	0.71	0.99	0.99	0.99
20 (H/T)	6.70	5.78	5.81	–	0.43	0.70	0.76	0.90	0.91	–

Cov-SSI, Data-SSI, and FDD. The Cov-SSI method outperforms the other two methods in identifying modal parameters from the recording with the wave-driven response (Table 4). Additionally, note that the Cov-SSI algorithm performs better for most recordings with BR weighting, i.e., no weighting, than with CVA weighting. However, the identification of the modal parameters on some recordings is found to benefit from CVA weighting [24]. Data-SSI is found to provide results that are less clear than the Cov-SSI, including multiple clusters of modes that appear stable with similar mode shapes, but different natural frequency and damping estimates. No further efforts are devoted to investigating this result because it is considered beyond the scope. The FDD is not found to be suitable for the application.

The mode shapes obtained from the Cov-SSI analysis are presented in Fig. 7. The abbreviations H (horizontal), V (vertical), and T (torsional) are used to designate the main displacement patterns of the modes. When combined, the first letter corresponds to the main type of motion. The corresponding Argand phase plots are shown in Fig. 8.

Note that the presented mode shapes are in reality snapshots of the mode shapes from the moment where their total real part is at its largest: the mode shapes consist of complex numbers [14], and the components of the mode shapes have phase shifts between them, such that they reach their maximum at different time instances. The Argand vectors shown in Fig. 8 are rotating with the modal frequency, and their projections along the real axis represent the values of the DOFs. Normally, in modal analysis, it is required that the identified mode shapes have small phase differences, resulting in the modal phase colinearity (MPC) index being close to 1. Because the large added hydrodynamic damping makes

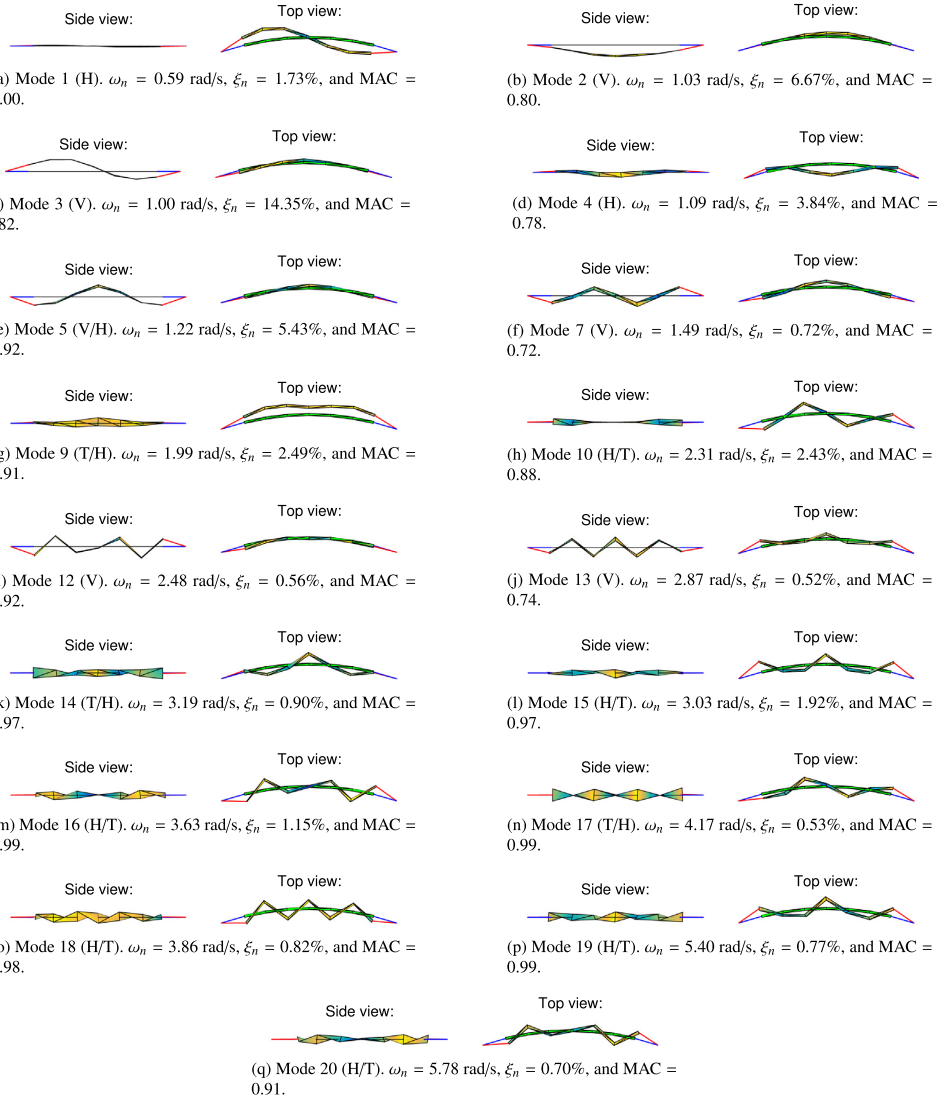

(a) Mode 1 (H). ω_n = 0.59 rad/s, ξ_n = 1.73%, and MAC = 1.00.

(b) Mode 2 (V). ω_n = 1.03 rad/s, ξ_n = 6.67%, and MAC = 0.80.

(c) Mode 3 (V). ω_n = 1.00 rad/s, ξ_n = 14.35%, and MAC = 0.82.

(d) Mode 4 (H). ω_n = 1.09 rad/s, ξ_n = 3.84%, and MAC = 0.78.

(e) Mode 5 (V/H). ω_n = 1.22 rad/s, ξ_n = 5.43%, and MAC = 0.92.

(f) Mode 7 (V). ω_n = 1.49 rad/s, ξ_n = 0.72%, and MAC = 0.72.

(g) Mode 9 (T/H). ω_n = 1.99 rad/s, ξ_n = 2.49%, and MAC = 0.91.

(h) Mode 10 (H/T). ω_n = 2.31 rad/s, ξ_n = 2.43%, and MAC = 0.88.

(i) Mode 12 (V). ω_n = 2.48 rad/s, ξ_n = 0.56%, and MAC = 0.92.

(j) Mode 13 (V). ω_n = 2.87 rad/s, ξ_n = 0.52%, and MAC = 0.74.

(k) Mode 14 (T/H). ω_n = 3.19 rad/s, ξ_n = 0.90%, and MAC = 0.97.

(l) Mode 15 (H/T). ω_n = 3.03 rad/s, ξ_n = 1.92%, and MAC = 0.97.

(m) Mode 16 (H/T). ω_n = 3.63 rad/s, ξ_n = 1.15%, and MAC = 0.99.

(n) Mode 17 (T/H). ω_n = 4.17 rad/s, ξ_n = 0.53%, and MAC = 0.99.

(o) Mode 18 (H/T). ω_n = 3.86 rad/s, ξ_n = 0.82%, and MAC = 0.98.

(p) Mode 19 (H/T). ω_n = 5.40 rad/s, ξ_n = 0.77%, and MAC = 0.99.

(q) Mode 20 (H/T). ω_n = 5.78 rad/s, ξ_n = 0.70%, and MAC = 0.91.

Fig. 7. Identified mode shapes corresponding to the modal parameters shown in Table 4 from the wave-driven recording and using the Cov-SSI method. The following abbreviations are used: H (horizontal), V (vertical), and T (torsional). The numbering refers to the modes obtained from the eigenvalue solution of the numerical prediction model.

the eigenvectors complex, this approach is unsuitable. Moreover, the arc shape of the bridge results in the mode shapes being more coupled in their appearance, including both horizontal, vertical, and torsional motions. The Argand plots shown in Fig. 8 reveal that there are significant phase shifts present between the DOFs for single modes. Because the hydrodynamic damping contributions are dependent on the direction, the phase shifts are also prone to be dependent on the motion pattern of the mode under investigation.

For the selected wave-driven recording, the performance of the Cov-SSI method is satisfactory. Most of the first 20 mode shapes from the numerical model are identified, with the only exceptions being modes 6, 8, and 11. Their mode shapes generally have decent

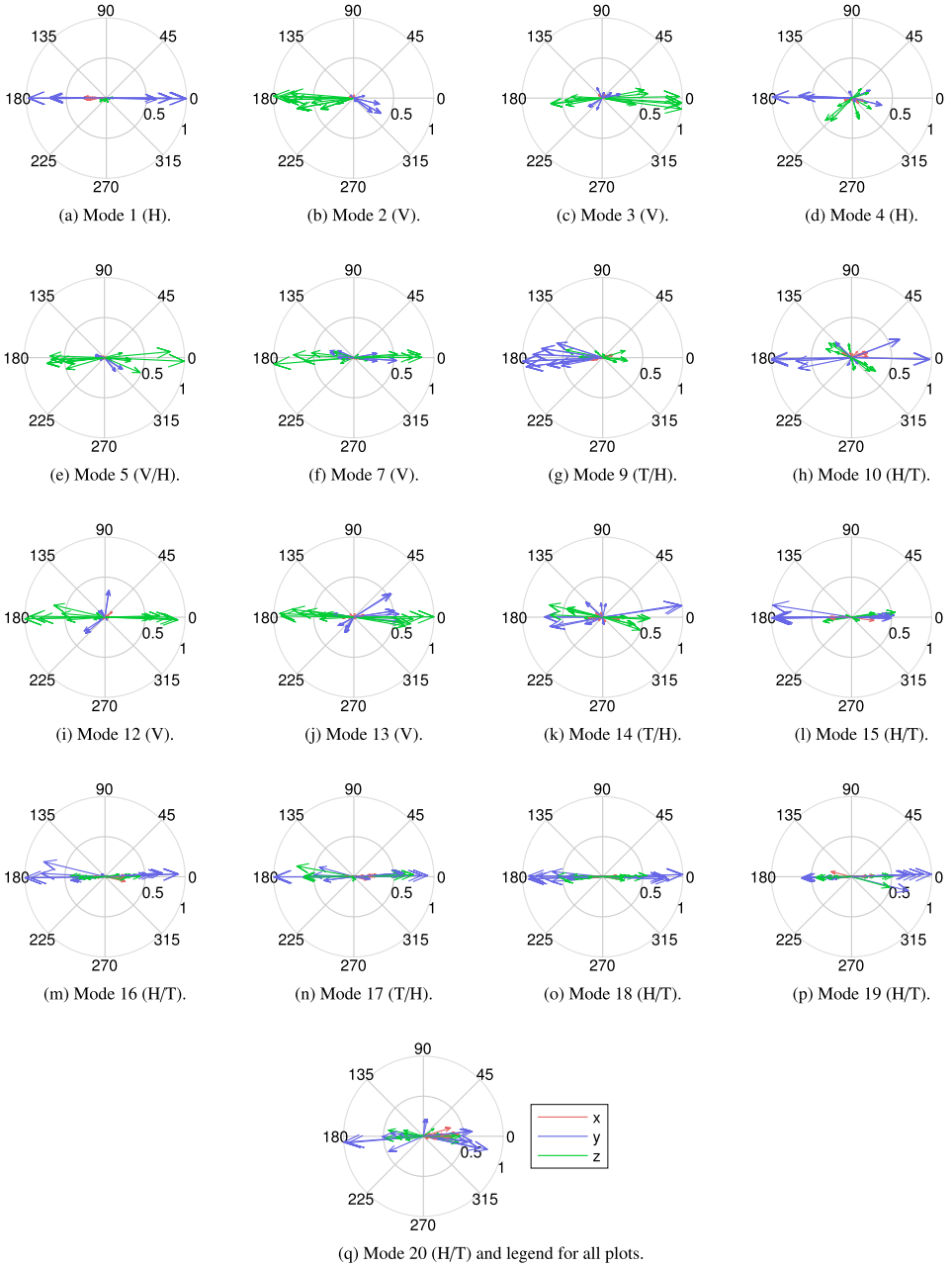

(a) Mode 1 (H). (b) Mode 2 (V). (c) Mode 3 (V). (d) Mode 4 (H).

(e) Mode 5 (V/H). (f) Mode 7 (V). (g) Mode 9 (T/H). (h) Mode 10 (H/T).

(i) Mode 12 (V). (j) Mode 13 (V). (k) Mode 14 (T/H). (l) Mode 15 (H/T).

(m) Mode 16 (H/T). (n) Mode 17 (T/H). (o) Mode 18 (H/T). (p) Mode 19 (H/T).

(q) Mode 20 (H/T) and legend for all plots.

Fig. 8. Argand plots of mode shapes corresponding to the modes in Table 4 and Fig. 7. from the wave-driven recording and using the Cov-SSI method. The numbering refers to the modes obtained from the eigenvalue solution of the numerical prediction model. All global degrees of freedom (DOFs), originating from all the accelerometer channels are plotted in all plots. The components are presented in different colours depending on whether they are longitudinal (x), lateral (y) or vertical (z).

Table 5
Modal parameters identified from the low-level recording by manual selection. The following abbreviations are used: H (horizontal), V (vertical), and T (torsional). Note that the analytic values are obtained using the methodology presented in [14] but with an updated model [15].

	Frequency [rad/s]		Damping ratio [%]		
	Analytic	Cov-SSI	Analytic	Cov-SSI	MAC (with analytic)
12 (V)	2.40	2.48	0.35	0.60	0.93
14 (T/H)	3.10	3.18	0.38	0.87	0.94
15 (H/T)	3.15	3.04	1.29	1.40	0.96
16 (H/T)	3.84	3.63	0.72	0.92	0.99
17 (T/H)	4.02	4.16	0.29	0.56	0.99
18 (H/T)	4.09	3.87	0.59	1.03	0.97
19 (H/T)	5.22	5.41	0.35	0.67	0.98

Table 6
Modal parameters identified from the traffic-driven recording by manual selection. The following abbreviations are used: H (horizontal), V (vertical), and T (torsional). Note that the analytic values are obtained using the methodology presented in [14] but with an updated model [15].

	Frequency [rad/s]		Damping ratio [%]		
	Analytic	Cov-SSI	Analytic	Cov-SSI	MAC (with analytic)
4 (H)	1.05	0.97	5.00	2.92	0.47
7 (V)	1.44	1.48	3.28	1.90	0.88
8 (V)	1.87	1.94	1.07	0.91	0.84
11 (T/H)	2.24	2.26	3.98	0.73	0.57
12 (V)	2.40	2.49	0.35	0.38	0.98
13 (V)	2.75	2.87	0.29	0.64	0.68
14 (T/H)	3.10	3.19	0.38	0.62	0.81
15 (H/T)	3.15	3.07	1.29	0.76	0.39
17 (T/H)	4.02	4.16	0.29	0.46	0.63
18 (H/T)	4.09	3.88	0.59	0.80	0.50

MAC values, ranging between 0.72 and 1, and frequency values close to the estimated numerical values. The damping identification is, as expected, the most challenging sub-task. Large variations in the damping ratios are observed (Table 4), with the largest absolute discrepancy observed for mode 2, which is much lower than the predicted value (6.67% versus 12.25%). The critical damping ratio for mode 3, however, is consistently higher than the predicted value (14.35% versus 11.24%). Considering all the identified damping ratios, the total damping level is in agreement with the estimates from the eigenvalue solution of the numerical prediction model.

A manual identification with the Cov-SSI was also performed for the selected low-level and traffic-driven recordings, yielding the results shown in Tables 5 and 6, respectively. Both cases provide below-satisfactory results; in the low-level recording the bridge is only sufficiently excited to reliably identify 7 of the first 20 modes, whereas the response measurements in the traffic-driven recording results in mode shapes with poor MAC values relative to the numerical predictions.

4.3. On the selection of parameters for the SSI analyses

The results from the SSI analyses are highly dependent on the chosen parameters, and a proper selection of these parameters will therefore vary from application to application. The most important aspects observed in the current case study are presented in the following sub-sections.

4.3.1. Duration

The durations of the recordings were kept fixed at approximately 30 min. For practical reasons, when subdividing long recordings, the duration was allowed to range between 29 and 30 min, i.e., $T \in [29\ \text{min}, 30\ \text{min}]$. For a structure that is heavily influenced by a single environmental process, it is not beneficial with a very long recording, contrary to the case for structures less controlled by a single process. The stationarity of the process, and thus the response of the structure, is an important concern. The durations of the recordings are therefore a compromise between keeping the recordings near stationary while simultaneously increasing the durations to acceptable levels. The optimum length will be dependent on the level of non-stationarity of the loading process. No stationarity checks were conducted in the following study. However, visual inspections of the recorded time histories were performed to ensure that no abrupt changes occured in the excitation or response.

4.3.2. Blockrows

The number of blockrows is the main input parameter of SSI analyses, and its selection affects the solution to a large extent. The number of blockrows should be chosen to be large enough such that the time lags represented in the covariance matrix have sufficient length to be able to describe the lowest frequencies of interest in the data. If the number of chosen blockrows is too low, these

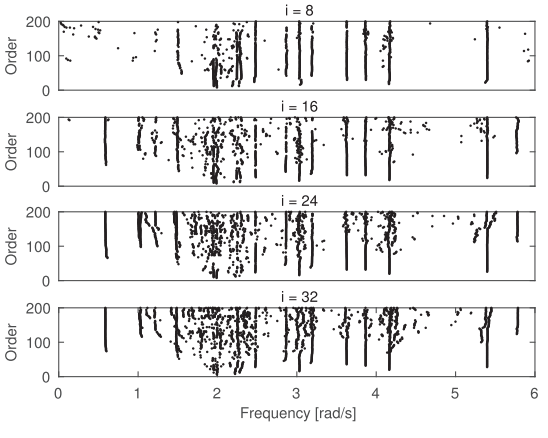

(a) Stability level, $s = 2$.

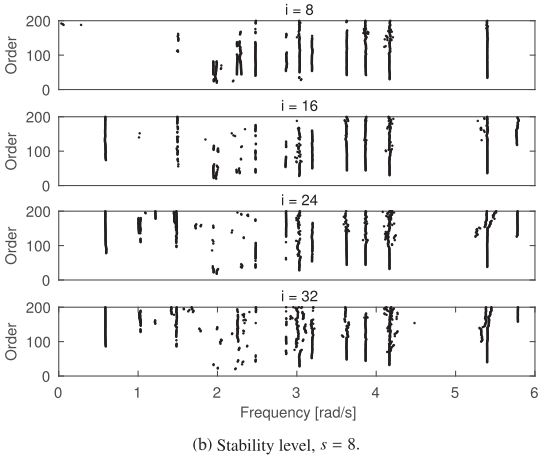

(b) Stability level, $s = 8$.

Fig. 9. Stabilization plots with different blockrows, i, for Cov-SSI analyses of the wave-driven recording.

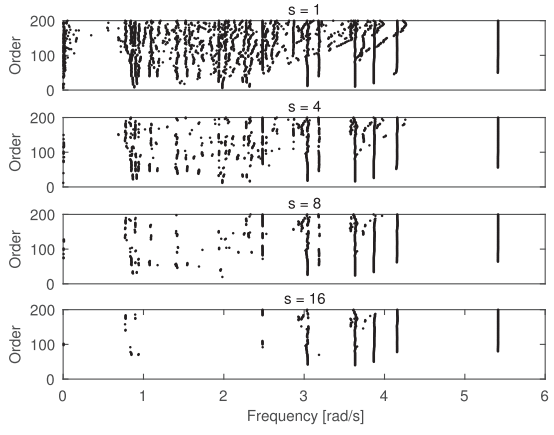

(a) Low-level recording.

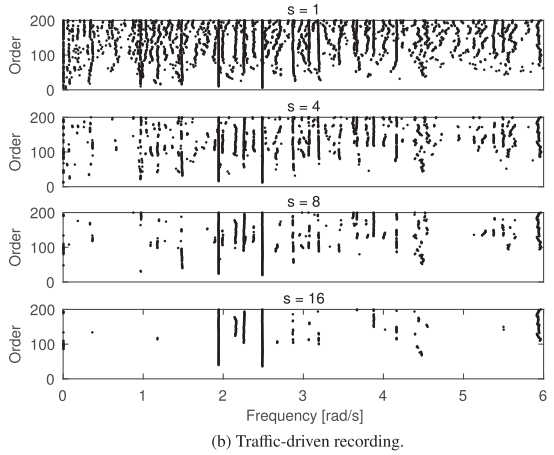

(b) Traffic-driven recording.

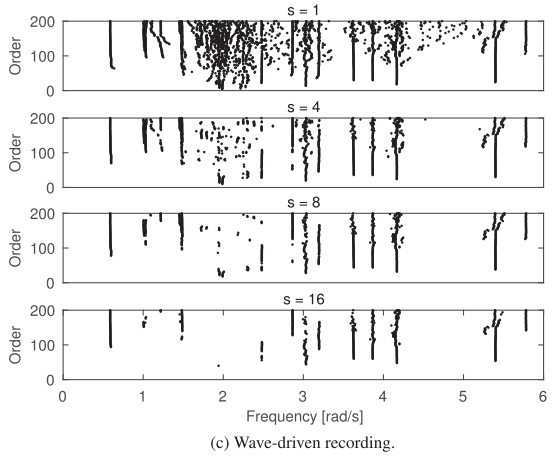

(c) Wave-driven recording.

Fig. 10. Stabilization plots with different stability levels, s, for Cov-SSI analyses with blockrows, $i = 24$.

components will simply not be identified with confidence. If the number of chosen blockrows is too high, the amount of spurious modes will increase. For the wave-driven recording, $i = 24$, corresponding to a maximum time lag of $\tau = 2 \cdot 24 \cdot 2^{-1} = 24$ s or a minimum frequency of $f = \frac{1}{24} \approx 0.04$ Hz, was found to be a good compromise between clear stabilization plots and the number of modes visible for various stability levels (Fig. 9). The sample rate, which was 2 Hz in the current application, is a critical quantity to consider together with the number of blockrows. The effects that changes of blockrows have on the modal parameters are not considered in the current paper.

Table 7
Slack allowance and MAC requirement (to analytical modes).

Parameter	Value
Frequency slack, S_f	10%
Damping slack, S_ξ	50%
MAC slack, S_{MAC}	10%
MAC requirement, MAC_{ref}	0.7

4.3.3. Stabilization level

The selection of the stabilization level in the plotting of the stabilization plots is powerful for tweaking the results. A low stabilization level in combination with a high number of blockrows results in a very cluttered stabilization plot, which is a difficult starting point for separating the physical poles from the spurious ones (Fig. 10). Thus, the stability level should be selected with consideration of the blockrows. In the following, a stability level of $s = 8$ is found to be suitable in combination with $i = 24$. The clutter in the stabilization plots for the three cases, shown in Fig. 10, is located at different frequencies. By comparing with the spectral densities of the lateral accelerations of the midmost pontoon, estimated using Welch's method and plotted in Fig. 6, there is a striking resemblance: the loading processes acting on the structure differing from a white noise process result in false poles, which are only identified as unstable when the stability level is increased.

4.3.4. Orders

The maximum of the range of orders is simply selected based on visual inspection of the stabilization plot, with the requirement that no new straightly aligned (stable) poles are developed for increasing order. A reasonable selection of orders, based on the other parameters set above and visual inspection of the stabilization plots, is $n = 2, 4, \ldots, 200$.

4.4. Environmental influence and automatic OMA

By automating the selection of modal parameters from each recording, the effects of weather and environment on the modal parameters can be investigated. The eigenvalue solution of the numerical prediction model was used as a reference to ensure a consistent numbering of the identified modes. Due to the combination of efficiency and accuracy of the Cov-SSI method, this was selected for the automatic OMA. The Cov-SSI parameters for all analyses were set according to the findings in the preceding section ($i = 24, s = 8, T \in [29\text{ min}, 30\text{ min}]$, and $n = 2, 4, \ldots, 200$). First, the stabilization criteria have to be fulfilled, as described in Section 2.3. Second, the MAC values between the poles and the modes from the eigenvalue solution have to be above a predefined value MAC_{ref} for them to be considered. The pole with the largest MAC value with the corresponding mode from the numerical prediction model is used as a reference, and all modes within certain slacks in frequency (S_f), damping (S_ξ) and MAC (S_{MAC}) from this are chosen. Finally, the means and standard deviations of all the chosen frequencies, damping ratios and MACs are calculated. The allowed slack and the required MAC value are presented in Table 7.

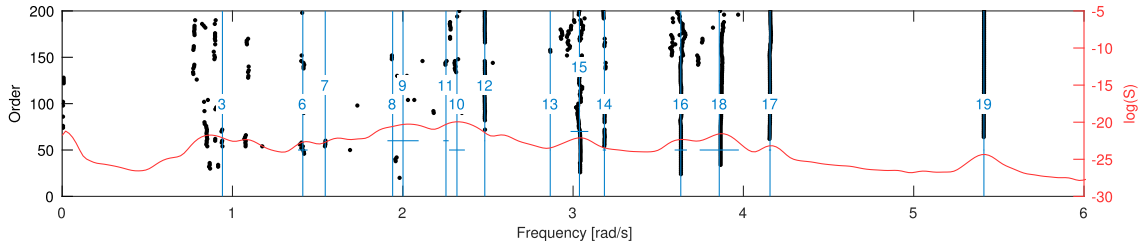

(a) Low-level response.

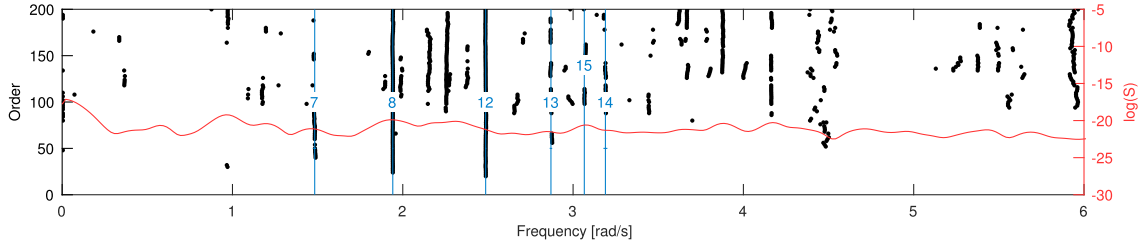

(b) Traffic-induced response.

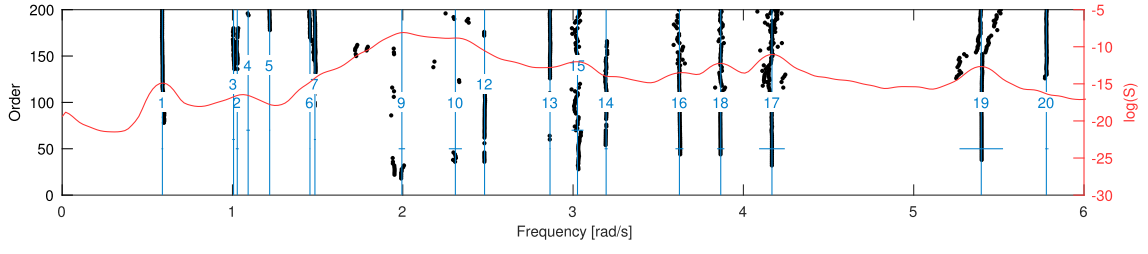

(c) Wave-induced response.

Fig. 11. Stabilization plots for the automatic Cov-SSI analyses of the three selected recordings. Only the poles deemed stable are shown here, in agreement with the requirements stated in Table 2. Vertical lines indicate the modes identified, and horizontal lines denote $\pm 3\sigma_{\omega}$, corresponding to the stable poles within the predefined slack and above the MAC requirement presented in Table 7. The numbers refer to the numbers of analytical modes. The red lines show the power spectral density estimate from the lateral acceleration of pontoon 3, corresponding to the indicated recording.

Table 8
Automatically identified modes from the wave-driven recording. Three standard deviations are used as the measure for accuracy. *Damping* refers to the critical damping ratio [%], while *frequency* refers to the undamped natural frequency [rad/s]. The following abbreviations are used: H (horizontal), V (vertical), and T (torsional).

	Analytic		Cov-SSI		
Mode	Frequency	Damping	Frequency	Damping	MAC
1 (H)	0.58	1.63	0.59 ± 0.00	1.9 ± 0.56	0.99 ± 0.00
2 (V)	0.99	12.25	1.03 ± 0.01	6.5 ± 0.50	0.76 ± 0.13
3 (V)	1.03	11.24	1.01 ± 0.01	14.5 ± 1.08	0.84 ± 0.05
4 (H)	1.05	5.00	1.09 ± 0.01	3.8 ± 0.31	0.78 ± 0.02
5 (V/H)	1.17	7.67	1.22 ± 0.00	5.5 ± 0.37	0.92 ± 0.01
6 (H/T)	1.38	5.91	1.45 ± 0.00	6.5 ± 0.47	0.71 ± 0.01
7 (V)	1.44	3.28	1.48 ± 0.01	2.3 ± 0.27	0.71 ± 0.02
8 (V)	1.87	1.07	–	–	–
9 (T/H)	1.95	3.62	1.99 ± 0.02	2.4 ± 0.56	0.90 ± 0.05
10 (H/T)	2.23	0.43	2.31 ± 0.04	2.7 ± 1.39	0.88 ± 0.18
11 (T/H)	2.24	3.98	–	–	–
12 (V)	2.40	0.35	2.48 ± 0.00	0.6 ± 0.06	0.91 ± 0.06
13 (V)	2.75	0.29	2.86 ± 0.00	0.5 ± 0.13	0.75 ± 0.07
14 (T/H)	3.10	0.38	3.19 ± 0.01	0.9 ± 0.33	0.97 ± 0.02
15 (H/T)	3.15	1.29	3.03 ± 0.03	2.1 ± 1.29	0.96 ± 0.04
16 (H/T)	3.84	0.72	3.62 ± 0.02	1.1 ± 0.58	0.98 ± 0.02
17 (T/H)	4.02	0.29	4.17 ± 0.08	0.6 ± 0.52	0.98 ± 0.03
18 (H/T)	4.09	0.59	3.87 ± 0.02	0.8 ± 0.41	0.98 ± 0.01
19 (H/T)	5.22	0.35	5.40 ± 0.13	0.7 ± 0.34	0.98 ± 0.04
20 (H/T)	6.70	0.43	5.78 ± 0.01	0.9 ± 0.36	0.91 ± 0.03

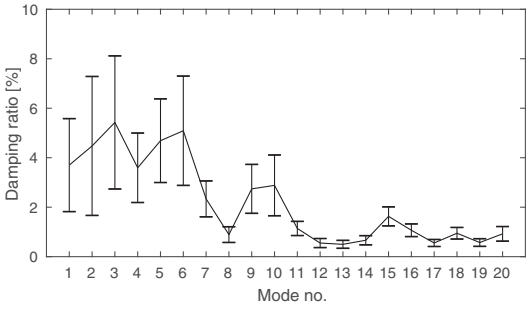

Fig. 12. Average estimated damping ratios for the first 20 modes, based on all recordings. The error bars represent one standard deviation ($\pm\sigma$).

The presented values were used for the entire period under investigation. Fig. 11 shows the resulting identified modes overlaid on the stabilization plots for the three selected recordings. This figure is supported by the numerical data in Table 8. The automatic algorithm works well for the wave-driven recording and performs decently for the low-level response recording. The selected traffic-driven recording performs poorly and appears to contain spurious modes from harmonics at multiple frequencies, represented by several scattered poles in Fig. 11b. The only reason that these are not erroneously interpreted as modes is because the predicted mode shapes, obtained from the eigenvalue solution of the numerical prediction model, are used as a reference. Our general preference has been placed on the quality rather than the quantity of the data; thus both data and modal results suspected of being of poor quality are rejected automatically. The disadvantage is that the number of data points for statistical analyses may be smaller than preferred.

The procedure is dependent on a well-tuned numerical prediction model, and it will not handle changes in mode shape very well. Furthermore, for higher modes, the number of accelerometers installed will not be sufficient to capture the motion between the pontoons, and the MAC numbers will erroneously tend to large values. However, the authors believe that the simple procedure presented herein will capture the main aspects of the bridge's behaviour in a robust manner.

The averaged identified damping estimates from all recordings are illustrated for the first 20 modes in Fig. 12. The error bars indicate one standard deviation above and below the mean value.

Fig. 13 shows the *coefficient of variation* of the natural frequency, $C_{v,\omega}$, and damping ratio, $C_{v,\xi}$, for the first 20 modes. The coefficient of variation is defined as the mean-normalized standard deviation, i.e., $C_v = \sigma/\mu$. The figure reveals a decent level of variation in the identified natural frequencies. It also reveals that there are large variations in the identified damping ratios, as expected. Some modes are only identified in a small selection of the pool of recordings, resulting in a very low number of samples and thus a poor starting point for estimating statistical derivatives.

The identified natural frequencies and damping ratios for the first six modes are illustrated in Fig. 14. This figure reveals a clear reduction in scatter for increased excitation levels, represented by SWH here. This effect is believed to primarily arise from the uncertainty in the identification, which is far larger for small excitation levels. The reduced excitation levels also result in the fact that the uncertain and unaccounted excitation sources, such as traffic, accounts for far more of the total load and consequently increases the scatter. The damping levels show an increasing tendency to increasing excitation levels, which is reasonable. A similar study was performed on the effect of changing wind speeds. The results of that study were very similar but more scattered. This is explained by the fact that the wind controls the waves, but the bridge response and hence the modal analysis results are mainly affected by the waves. Consequently, no such results are reported herein. The effect of changes in the tidal levels, which normally vary by approximately 2 m on site, on the modal parameters was found to be insignificant. No relation between the traffic level, characterized by the TI, and the damping level was visible. Note that no rejection criterion based on the stationarity level is applied, and that non-stationarity in the recordings might cause more scatter.

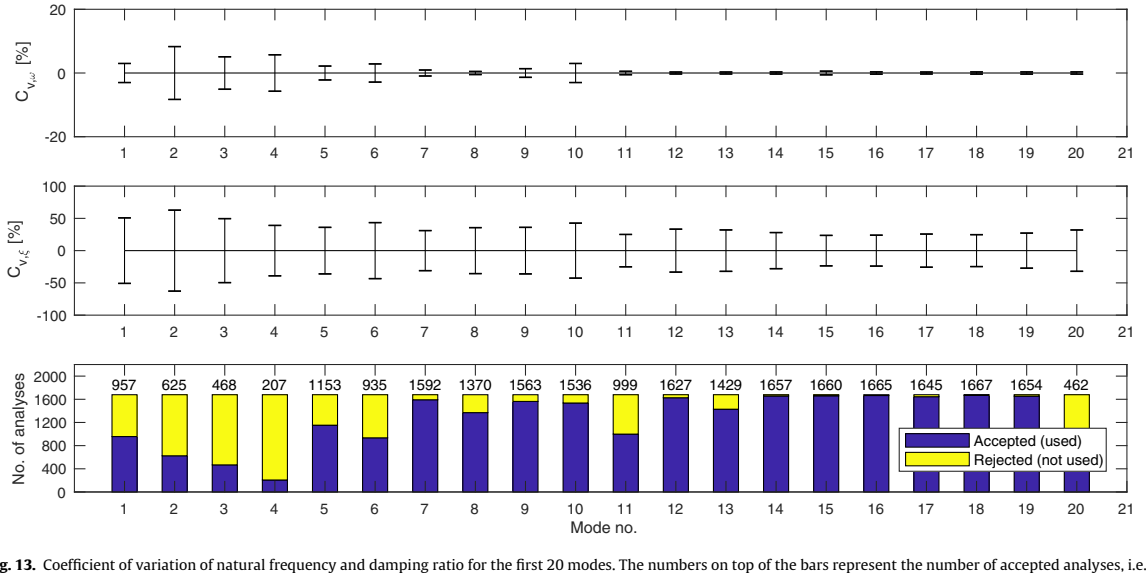

Fig. 13. Coefficient of variation of natural frequency and damping ratio for the first 20 modes. The numbers on top of the bars represent the number of accepted analyses, i.e., the number of samples used for the estimate of the coefficient of variation.

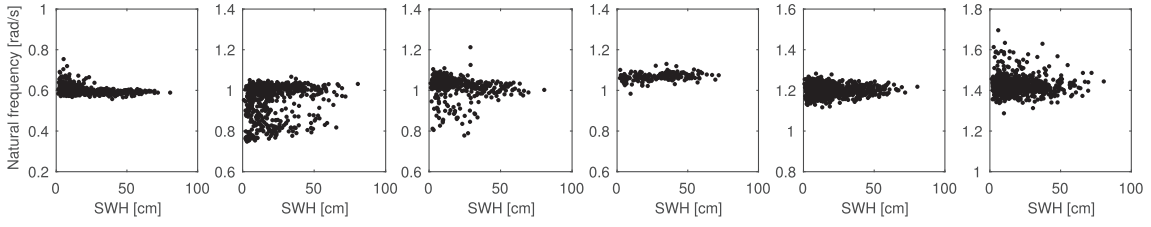

(a) Natural frequency.

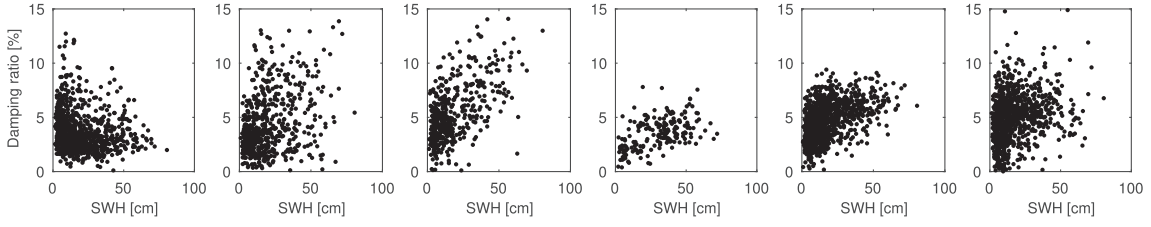

(b) Damping ratio.

Fig. 14. The effect of the SWH on the identified modal parameters, arranged ascending from mode 1 to mode 6 (left to right).

5. Concluding remarks

Based on recordings from the state-of-the-art monitoring system installed on the Bergsøysund Bridge, measuring both response (accelerations and displacements) and environmental actions (wind and waves), system identification has been successfully performed on the acceleration recordings and are interpreted in light of the recorded environmental factors. The Cov-SSI, Data-SSI and FDD methods have been applied for manual identification surveys, and the resulting identified modes have been compared with the modal quantities obtained from the solution of the eigenvalue problem from a comprehensive numerical model set-up. The Cov-SSI method shows the most promise among the methods. The Data-SSI method also provides decent results, whereas the FDD method is insufficient for this application. Natural frequencies and mode shapes are very well identified, whereas there are relatively large uncertainties in the identification of the damping ratios. However, the overall damping levels are consistent with the estimates from the eigenvalue solution of the numerical prediction model. Large damping levels, closely spaced modes, and a geometric design resulting in coupled motion, make the identification procedure challenging. Due to scattered stabilization plots, the interpretation and manual selection are tasks that add additional uncertainties to the results.

Due to the complexity of the problem, effort has to be placed on the selection of the analysis parameters. The number of blockrows is a parameter that directly affects the results of the algorithm, and it should be chosen with care. By producing stabilization plots with different numbers of blockrows, a reasonable value was chosen based on visual inspection of the plots. To reduce clutter in the stabilization plots, a rather large stabilization level is recommended. A stabilization level of $s = 8$ was utilized, with a good result, in the current paper.

By automating the selection of stable poles, relying on the mode shapes from the eigenvalue solution of the numerical prediction model, a study on the effect of the wave excitation on the natural frequency and damping was performed. This study revealed that the uncertainties in the identified modal quantities are generally reduced when the excitation level increases. This is believed to be a consequence of a larger proportion of the excitation being known, as well as the identification algorithms performing better for larger response levels. Furthermore, the damping levels tend to increase for increasing SWH.

5.1. Future work

The selection of the system identification technique is a difficult task, and other methods should also be considered for the task. In particular, methods better suited for problems with loading processes that considerably differ from white noise, such as blind source separation (BSS) methods, should be considered. Furthermore, more sophisticated techniques for the automatic selection of poles should be applied. This may enable stronger conclusions about the effect from the environmental parameters to be drawn.

Acknowledgements

This research was conducted with financial support from the Norwegian Public Roads Administration. The authors gratefully acknowledge this support.

References

[1] Watanabe E, Utsunomiya T. Analysis and design of floating bridges. Prog Struct Mat Eng 2003;5(3):127–44. http://dx.doi.org/10.1002/pse.151.
[2] McLamore VR, Hart GC, Stubbs IR. Ambient vibration of two suspension bridges. J Struct Division 1971;97(10):2567–82.
[3] Brownjohn JMW, Magalhaes F, Caetano E, Cunha A. Ambient vibration re-testing and operational modal analysis of the Humber Bridge. Eng Struct 2010;32(8):2003–18. http://dx.doi.org/10.1016/j.engstruct.2010.02.034. <http://linkinghub.elsevier.com/retrieve/pii/S0141029610000878>.
[4] Peeters B, De Roeck G. One-year monitoring of the Z24-Bridge: environmental effects versus damage events. Earthq Eng Struct Dyn 2001;30(2):149–71. http://dx.doi.org/10.1002/1096-9845(200102)30:2<149::AID-EQE1>3.0.CO;2-Z.
[5] Farrar C, James G. System identification from ambient vibration measurements on a bridge. J Sound Vib 1997;205(1):1–18. http://dx.doi.org/10.1006/jsvi.1997.0977. <http://www.sciencedirect.com/science/article/pii/S0022460X97909779>.
[6] Magalhães F, Cunha Á, Caetano E. Dynamic monitoring of a long span arch bridge. Eng Struct 2008;30(11):3034–44. http://dx.doi.org/10.1016/j.engstruct.2008.04.020. <http://www.sciencedirect.com/science/article/pii/S0141029608001405>.

[7] Brownjohn JMW, Moyo P, Omenzetter P, Lu Y. Assessment of highway bridge upgrading by dynamic testing and finite-element model updating. J Bridge Eng 2003;8(3):162–72. http://dx.doi.org/10.1061/(ASCE)1084-0702(2003)8:3(162).
[8] Andersen P, Brincker R, Peeters B, De Roeck G, Hermans L, Krämer C. Comparison of system identification methods using ambient bridge test data. In: Proc. of the 17th international modal analysis conference, Kissimee, Florida; 1999. p. 7–10.
[9] Peeters B, Ventura C. Comparative study of modal analysis techniques for bridge dynamic characteristics. Mech Syst Signal Process 2003;17:965–88. http://dx.doi.org/10.1006/mssp.2002.1568. <http://www.sciencedirect.com/science/article/pii/S0888327002915682>.
[10] Brownjohn JMW, Carden E.P. Tracking the effects of changing environmental conditions on the modal parameters of Tamar Bridge. In: 3rd international conference on structural health monitoring and intelligent infrastructure; 2007.
[11] Cabboi A, Magalhães F, Gentile C, Cunha Á. Automated modal identification and tracking: application to an iron arch bridge. Struct Control Health Monit 44:44. doi:http://dx.doi.org/10.1002/stc.1854.
[12] Kvåle KA, Øiseth O, Rønnquist A, Sigbjörnsson R. Modal analysis of a floating bridge without side-mooring. Dynamics of civil structures, vol. 2. Springer; 2015. p. 127–36. http://dx.doi.org/10.1007/978-3-319-15248-6_14. <http://link.springer.com/10.1007/978-3-319-15248-6_14>.
[13] Rainieri C, Fabbrocino G, Cosenza E. Some remarks on experimental estimation of damping for seismic design of civil constructions. Shock Vib 2010;17(4,5):383–95.
[14] Kvåle KA, Sigbjörnsson R, Øiseth O. Modelling the stochastic dynamic behaviour of a pontoon bridge: a case study. Comput Struct 2016;165:123–35. http://dx.doi.org/10.1016/j.compstruc.2015.12.009. <http://linkinghub.elsevier.com/retrieve/pii/S004579491500334X>.
[15] Petersen ØW, Øiseth O. Sensitivity-based finite element model updating of a pontoon bridge. Eng Struct, submitted for publication.
[16] Brincker R, Zhang L, Andersen P. Modal identication from ambient responses using frequency domain decomposition. In: Proceedings of 18th international modal analysis conference; 2000. p. 625–30.
[17] Brincker R, Zhang L, Andersen P. Modal identification of output-only systems using frequency domain decomposition. Smart Mater Struct 2001;10(3):441.
[18] Hermans L, van der Auweraer H. Modal testing and analysis of structures under operational conditions: industrial applications. Mech Syst Signal Process 1999;13(2):193–216. http://dx.doi.org/10.1006/mssp.1998.1211. <http://www.sciencedirect.com/science/article/pii/S0888327098912110>.
[19] Rainieri C, Fabbrocino G. Operational modal analysis of civil engineering structures. New York: Springer; 2014.
[20] Van Overschee P, De Moor B. Subspace identification for linear systems: theory, implementation, applications. Boston/London/Dordrecht: Kluwer Academic Publishers.; 1996.
[21] Allemang RJ, Brown DL. A correlation coefficient for modal vector analysis. Proceedings of the 1st international modal analysis conference, vol. 1. Orlando: SEM; 1982. p. 110–6.
[22] Allemang RJ. The modal assurance criteriontwenty years of use and abuse. Sound Vib 2003;37(8):14–23.
[23] Kvåle KA, Øiseth O. Structural monitoring of an end-supported pontoon bridge. Marine Struct 2017;52:188–207. http://dx.doi.org/10.1016/j.marstruc.2016.12.004. <http://linkinghub.elsevier.com/retrieve/pii/S0951833916300284>.
[24] Kvåle KA, Øiseth O, Rönnquist A. Covariance-driven stochastic subspace identification of an end-supported pontoon bridge under varying environmental conditions. In: Caicedo J, Pakzad S, editors. Dynamics of civil structures, Conference proceedings of the society for experimental mechanics series, vol. 2. Cham: Springer; 2017.

Paper 4

Knut Andreas Kvåle, Ole Øiseth

"Dynamic response of an end-supported pontoon bridge due to wave excitation: numerical predictions versus measurements"

Manuscript submitted for journal publication, 2017.

Dynamic response of an end-supported pontoon bridge due to wave excitation: numerical predictions versus measurements

Knut Andreas Kvåle[a,*], Ole Øiseth[a]

[a]*Department of Structural Engineering, Faculty of Engineering, NTNU, Norwegian University of Science and Technology, Trondheim, Norway*

Abstract

Herein, numerical predictions of the dynamic response of an existing floating pontoon bridge are compared with the measured dynamic response. Hydrodynamic coefficients that describe the fluid-structure interaction and the wave transfer functions are obtained by applying linear potential theory. The results obtained from the hydrodynamic analysis are combined with a beam model of the bridge in a finite element method (FEM) framework to enable stochastic response prediction through the power spectral density method. Predictions of the response power spectral density due to excitation characterized by the recorded sea surface elevation are compared with those obtained from the corresponding response measurements. Furthermore, the standard deviations of the predicted accelerations are compared with the standard deviations of the measured accelerations, and the overall quality of the prediction model is discussed. The measured and predicted responses compare well for the lateral components, decent for the vertical components and poorly for the torsional components.

Keywords: Bergsøysund Bridge, floating bridge, high damping, stochastic response prediction

1. Introduction

The Norwegian Public Roads Administration (NPRA) is currently conducting a large-scale project to make Coastal Highway E39, which is the highway located along the industry-dense Norwegian west coast, ferry free. By replacing ferries with permanent road links, travel times may be reduced by several hours. Many of the straits to cross are deep and wide fjords, which will require an extension of the current bridge technology. Among the possible options are various types of floating bridges, particularly end-supported solutions with multiple separate pontoons.

There are limited numbers of long-span floating road bridges, and such bridges are primarily located in the United States, Canada, Japan and Norway. Among these bridges, there are two that are end-supported only, namely, the Nordhordland Bridge and the Bergsøysund Bridge, which are both located on the western coast of Norway. Additionally, these two bridges are both based on separate pontoons rather than on a continuous floating pontoon girder. Because these bridges are not supported by side-mooring, they are more flexible and thus susceptible to large displacements and dynamic behaviour. It follows from the above that the available experience regarding the performance of similar structures is very scarce. Some case studies investigating the response of floating bridges exist, e.g., for the Nordhordland Bridge [1], the Bergsøysund Bridge [2, 3], the Hood Canal Bridge [4], the William R. Bennett Floating Bridge [5], and the Yumemai Bridge [6, 7]. However, available studies that compare the response of an existing floating bridge with numerical predictions are very limited. The original Hood Canal Bridge in the state of Washington was instrumented with sensors to monitor its response, and these measurements were compared with predictions by Georgiadis [8]. Furthermore, Peterson [9] investigated the performance of mooring cables on the original Evergreen Point Floating Bridge, which is also located in the state of Washington. Thanks to modern sensor technology and a drastic increase in data processing power, it is currently practically possible to handle considerably larger and more accurate sensor networks. The current paper relies on a comprehensive state-of-the-art monitoring system; consequently, this work is able to be more detailed in the comparison of the predicted and measured responses.

The accuracy of the prediction methodology is one of the main concerns for ensuring a safe, reliable and cost-efficient design of new floating bridges. The current paper addresses this concern using a comprehensive model set-up [2] of and an extensive monitoring system on the Bergsøysund Bridge [10]. Recorded acceleration quantities are compared to predictions from a numerical model set-up in a finite element method (FEM) framework. The bridge is instrumented with sensors that record the response and the excitation, thus making it possible to verify and scrutinize the model and methodology used for the response prediction. Fluid-structure interaction terms and wave excitation transfer functions are estimated by applying linear potential theory. Through the common assumptions of deep water, linear waves, and a stationary and homogeneous wave field, the power spectral density method is applied to predict the response spectral density matrix from a one-point wave spec-

*Corresponding author

tral density and a directional distribution.

1.1. The Bergsøysund Bridge

The Bergsøysund Bridge is a 930-meter-long end-supported pontoon bridge (Fig. 1) that is located on the western coast of Norway. The truss superstructure is supported by seven lightweight concrete pontoons. The anchor-free design makes this bridge highly flexible and an interesting case study for dynamic analysis. Furthermore, this bridge is the second largest of its kind in existence.

The excitation and response of the Bergsøysund Bridge are monitored using wave radars, anemometers, accelerometers, and a single global navigation satellite system (GNSS) displacement sensor (Fig. 2). For more details regarding the monitoring system, the reader is referred to [10].

Because the wave radar arrangement used in the majority of the recordings is not optimized for characterizing the directional distribution [11], the wave spreading and wave direction are not estimated. The effect that the wave spreading has on the response is not considered to be crucial [2].

2. Numerical prediction model

The dynamics of floating bridges exposed to first-order wave excitation can be represented using an FEM framework, as follows:

$$[M_s]\{\ddot{u}(t)\} + [C_s]\{\dot{u}(t)\} + [K_s]\{u(t)\} = \{p_h(t)\}, \quad (1)$$

where $[M_s]$ is the structural mass matrix, $[C_s]$ is the structural damping matrix, $[K_s]$ is the structural stiffness matrix, t is the time variable, $\{u(t)\}$ is the time-dependent displacement vector, $\{p_h(t)\}$ is the time-dependent total hydrodynamic action, and the dot notation is used to denote time differentiation. As a consequence of a single harmonic wave proportional to $e^{i\omega t}$, the total hydrodynamic action $\{p_h(t)\}$ can be written as follows:

$$\begin{aligned}\{p_h(t)\} =& \{P(\omega)\}e^{i\omega t} - [M_h(\omega)]\{\ddot{u}(t)\} \\ & - [C_h(\omega)]\{\dot{u}(t)\} - [K_h]\{u(t)\}. \end{aligned} \quad (2)$$

Here, $[M_h(\omega)]$, $[C_h(\omega)]$ and $[K_h]$ are the added hydrodynamic mass, hydrodynamic damping, and hydrodynamic stiffness, respectively, giving rise to self-exciting forces; ω is the frequency variable; and $\{P(\omega)\}e^{i\omega t}$ is the wave excitation due to the monochromatic wave. Through the superposition principle, this is directly interpretable as a general frequency-domain description for irregular stochastic waves. Second-order wave effects and wind excitation are not considered herein because the first-order wave excitation is considered to be the dominant excitation source.

2.1. Wave modelling

The cross-spectral density of the wave elevations at points r and s is described as follows [12]:

$$\begin{aligned} S_{\eta_r\eta_s}(\omega) = & \int_{-\pi}^{\pi} S_\eta(\omega) D(\theta) \dots \\ & \times \exp\left(i \frac{|\omega|\omega}{g} (\Delta x_{rs} \cos\theta + \Delta y_{rs} \sin\theta) \right) d\theta, \end{aligned} \quad (3)$$

where $S_\eta(\omega)$ is the one-point auto-spectral density and $D(\theta)$ is the directional distribution, both of which are equal everywhere under the assumption of homogeneity; i is the imaginary unit; ω is the frequency variable; g is the gravitational constant; $\Delta x_{rs} = x_s - x_r$; $\Delta y_{rs} = y_s - y_r$; and θ is the angular variable. In the above equation, it is assumed that the two-dimensional wave spectral density is decomposed as $S_\eta(\omega,\theta) = S_\eta(\omega)D(\theta)$. Furthermore, the cross-spectral densities of the wave excitations on pontoons r and s (located at points r and s) are given as follows:

$$[S_{p_r,p_s}(\omega)] = \int_{-\pi}^{\pi} \{q_r(\omega,\theta)\} S_{\eta_r\eta_s}(\omega,\theta) \{q_s(\omega,\theta)\}^H d\theta. \quad (4)$$

Here, $\{q_r(\omega,\theta)\}$ is the hydrodynamic transfer function relating the wave elevation to three forces and three moments acting on pontoon r; $S_{\eta_r\eta_s}(\omega,\theta)$ is the two-dimensional cross-wave spectral density, which is equal to the integrand in Eq. 3; and ^{H} is the Hermitian operator, which is defined as the complex conjugate and matrix transpose. Because there are 7 pontoons in total, there are 7x7 of these matrices to be computed, which are arranged in a global wave excitation spectral density matrix, $[S_p(\omega)]$.

In this model setup, there are two products that affect the final excitation: the one-dimensional wave spectral density and the directional distribution. Models for these two products are described in the following two sub-sections.

2.1.1. One-dimensional wave spectral density

The JONSWAP spectrum is defined as follows [13, 14]:

$$\begin{aligned} S(f) = & \alpha g^2 (2\pi)^{-4} f^{-5} \exp\left(-\frac{5}{4} \left(\frac{f}{f_p} \right)^{-4} \right) \\ & \times \gamma^{\exp\left(-\frac{(f-f_p)^2}{2\sigma^2 f_p^2} \right)} d\theta, \end{aligned} \quad (5)$$

where f is the frequency; f_p is the peak frequency; γ is the peakedness parameter; α is the Philips parameter; $\sigma = 0.07$ for $f < f_p$ and $\sigma = 0.09$ for $f \geq f_p$. This model is highly adjustable, and it is able to describe most monomodal wave spectral densities. However, this ability comes at the cost of needing to determine more parameters, which in principle are co-dependent and vary between excitation situations. The level of peakedness of the spectrum is given by γ. The value of α reflects the fetch characteristics of the wind-wave energy transfer at the site.

Fig. 1. Photograph of the Bergsøysund Bridge. Photograph by NTNU/K.A. Kvåle.

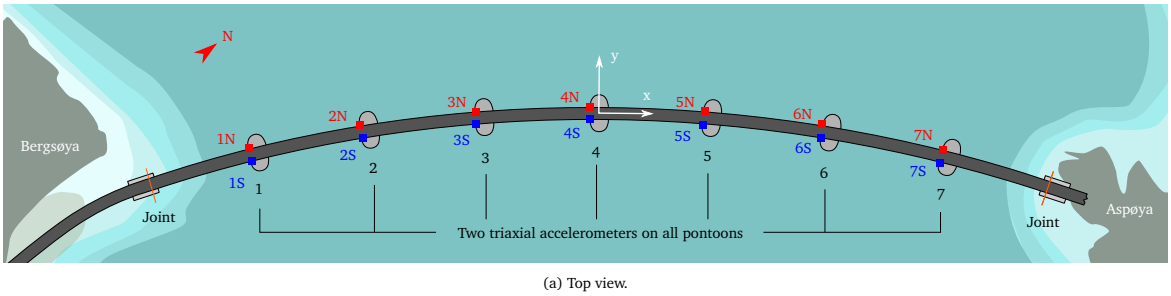

(a) Top view.

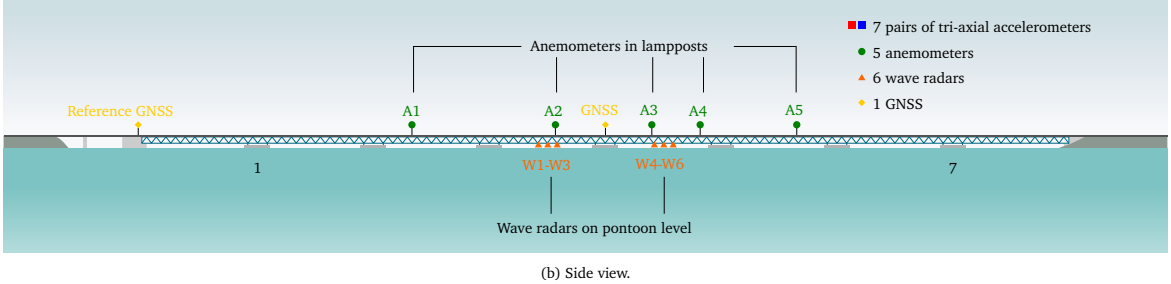

(b) Side view.

Fig. 2. Monitoring system operating on the Bergsøysund Bridge. Reproduced from [10] with permission from Elsevier.

2.1.2. Directional distribution

The $\cos^{2s}$ distribution is assumed in all the response predictions in the current paper, and it is defined as follows [15]:

$$D(\theta) = C\cos\left(\frac{\theta-\theta_0}{2}\right)^{2s}. \quad (6)$$

Here, C is a normalization factor introduced to ensure that $\int_0^{2\pi} D(\theta)d\theta = 1$, s is the spreading parameter, and θ_0 is the mean wave direction. Other distributions might be relevant for this application, but the authors believe that the effects caused by other uncontrollable error sources outweigh the effects of possible discrepancies in the model describing the directional distribution. The results in [2] also indicate that the directional distribution does not critically influence the response. A very similar distribution is used in the design basis, and it is defined as follows:

$$D(\theta) = C\cos(\theta-\theta_0)^n, \quad (7)$$

where, again, C ensures that $\int_0^{2\pi} D(\theta)d\theta = 1$ and n is the new spreading parameter. This model is only valid within the angle range $-\pi/2 \leq \theta-\theta_0 \leq \pi/2$, and it is assumed to be zero elsewhere. This model is therefore considered to be less robust and elegant than the model in Eq. 6 and is therefore not used for any predictions in this paper.

2.2. Response prediction

The power spectral density method (see, e.g., [1]) is a highly efficient approach for solving the frequency-dependent equation of motion presented above. The frequency-domain transfer function matrix, $[H(\omega)]$, is easily determined from the total mass, damping and stiffness matrices. Finally, the spectral density of the response is computed as follows:

$$[S_u(\omega)] = [H(\omega)][S_p(\omega)][H(\omega)]^H. \quad (8)$$

3. Results and discussion

Note that all response values are presented relative to a local coordinate system of each pontoon, where the x-axis is specified as along the tangent of the bridge main axis.

3.1. Design basis

The design rules for the Bergsøysund Bridge, which were provided by the Directorate of Public Roads, instructed applying a load with a $\cos^n$ directional distribution (Eq. 7) and a JONSWAP one-dimensional wave spectral density (Eq. 5)[16], with sea states specified by the parameters presented in Table 1.

The serviceability limit state (SLS) was based on wave conditions with a 1-year return period, whereas the ultimate limit state (ULS) was based on wave conditions with a 100-year return period. The provided table specifies ranges for the parameters T_p, γ and n. It is reasonable that an excitation peak period closer to the lowest modes, which for the current case study implies large peak periods, is conservative. However, caution should be taken with regard to resonant behaviour; excitation with periods close to periods corresponding to modes of the structure may lead to a large amplification of the response. For the peak periods that provide the largest response, it is reasonable that a more peaked spectral density, represented by a larger γ, is a conservative choice.

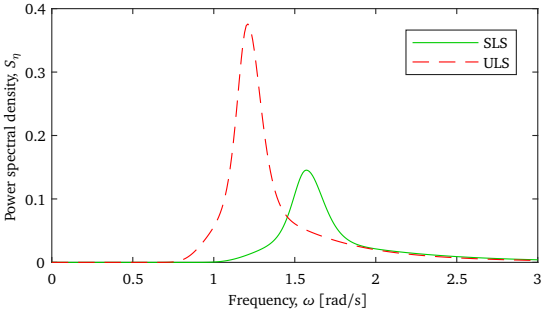

Fig. 3. JONSWAP spectral densities corresponding to SLS and ULS.

To assist in selecting appropriate parameters, a multivariate parameter study was conducted. This is exemplified in Fig. 5, which depicts the lateral acceleration standard deviation of pontoon 2, predicted with parameters γ and T_p varying within the ranges specified in Table 1. The selected degree of freedom (DOF) revealed the most interesting parameter dependency: a mode with a large contribution in the horizontal response results in a local peak in the response for $T_p = 3.3$ s. Note that the lateral component of pontoon 5 exhibits identical behaviour due to the symmetry of the model. All other important DOFs, i.e., the lateral, vertical and torsional responses of all other pontoons, did not have this pronounced mode-sensitive behaviour. The largest listed peak period for the 1-year sea state (4.6 s) was therefore selected, but the parameter study serves as a reminder of how dynamic problems may behave erratically. γ is chosen as the maximum value within the specified range, resulting in the following parameter sets for SLS $\{H_s = 1.00$ m, $T_p = 4.6$ s, $\gamma = 4.5\}$ and ULS $\{H_s = 1.41$ m, $T_p = 5.2$ s, $\gamma = 4.5\}$. The one-dimensional wave spectral densities corresponding to these two cases are depicted in Fig. 3. Note that the above argument is merely based on the standard deviation of the response. In reality, large standard deviation values do not necessarily describe the worst-case situation structurally; the frequency content of the response is also an important consideration because both the number of cycles in a fatigue consideration and the internal forces are dependent on which vibration modes are excited.

The largest listed spreading parameter is used for all cases, i.e., $n = 8$, which is approximately equivalent to a spreading parameter of $s = 17$ for the $\cos^{2s}$ distribution used in this study. Fig. 4 shows the directional distribution used in conjunction with both sea states, and it also confirms that the two distributions are equal in practice.

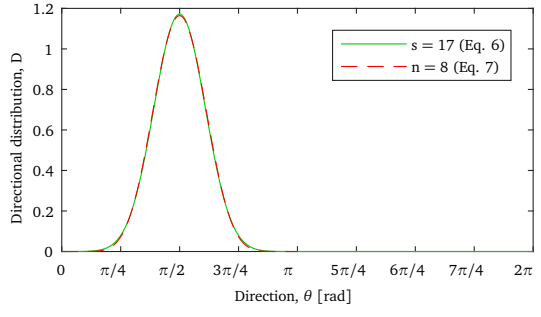

Fig. 4. Directional distribution with spreading $s = 17$ and mean wave direction $\theta_0 = \pi/2$.

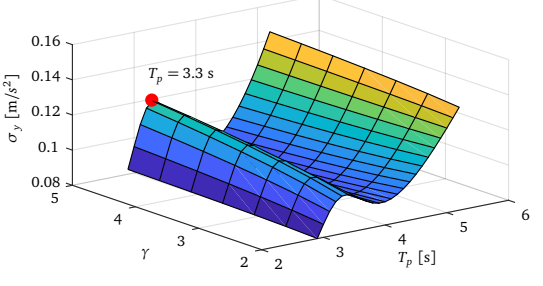

Fig. 5. Effect on response standard deviation on lateral acceleration on pontoon 2 due to varying γ and T_p. The spreading parameter $s = 17$. The parameters are set according to the ranges specified in Table 1. A local peak is located at approximately $T_p = 3.3$ s, which corresponds to the natural period of mode 10, as shown in Figure 6.

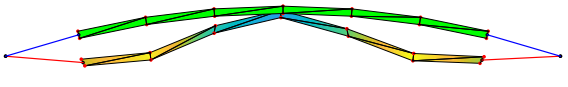

Fig. 6. Mode shape of mode 10, with damped natural period, $T_d = 3.28$ s.

3.2. Fitting of JONSWAP model

Spectral density estimates were established from all six wave radars for all recordings, and their average was used to fit the JONSWAP spectrum presented in Eq. 5. Welch's method, with 20 divisions enveloped by Hanning windows and 50% overlap, was used for all spectral estimates [17]. Curve fitting was based on minimizing the sum of square errors between a JONSWAP spectrum and the spectral density estimated from the wave measurement by applying the Nelder-Mead method, where γ and α were considered as the two free variables. The peak period T_p was directly determined from the spectral density estimate such that the minimization became more robust. The fitted JONSWAP spectra are used as one-dimensional wave spectral densities for all the numerical response predictions. Predictions were only performed if $R^2 > 0.8$ between the average wave spectrum and the JONSWAP fit, excluding cases where the JONSWAP spectrum was a poor fit. The R^2-value is used to describe the goodness of fit, and for the present work, the following definition is used [18]:

$$R^2 = 1 - \frac{\sum_{i=1}^{N}(f_i - y_i)^2}{\sum_{i=1}^{N}(y_i - \bar{y})^2}, \tag{9}$$

where f_i is the predicted or fitted value and y_i is the measured value, for numerical value i out of N in total, and $\bar{y}$ is the average of the measured value. R^2 measures the relative amount of variability that can be explained by the prediction or fit.

3.3. Specific case

The chosen recording was initiated on December 30, 2015, 18:25 (local time), and it has a duration of 30 minutes. Fundamental statistics from this recording are presented in Table 2. Winds were approaching the bridge nearly laterally, and a head sea is therefore a reasonable assumption. The directional distribution shown in Fig. 4 is used for the numerical predictions of the response. To justify the selection of a spreading parameter value s without any recordings to support it, the effect of changing spreading parameter on the acceleration response is illustrated in Fig. 7. This figure is consistent with the findings of a low sensitivity to changing spreading parameter in [2]. The mean wave direction is assumed to be lateral to the bridge, i.e., $\theta_0 = 90°$, which is considered to be a conservative choice. Furthermore, due to the geography surrounding the bridge, it is unlikely that large waves are approaching the bridge with mean wave directions that considerably deviate from lateral to the bridge.

Table 1. Design sea states [16].

Sea state	H_s [m]	T_p [s]	γ	n
1-year	1.00	2.9 – 4.6	2 – 4.5	2 – 8
10-year	1.23	3.1 – 4.9	2 – 4.5	2 – 8
100-year	1.41	3.3 – 5.2	2 – 4.5	2 – 8
100-year swell	0.16	6.7 – 16.0	7	10 – 20
Abnormal sea state	1.41	5.2 – 6.7	2 – 4.5	2 – 8

Table 2. Fundamental statistics from the selected recording. Listed acceleration and displacement values refer to standard deviations. Acceleration and displacement values describe the local motion of pontoon 3. Wind direction is defined as clock-wise increasing with 0° along the tangent at midspan.

	Wave height [cm]		Wind		Acceleration [mg]		Displacement [mm]	
Time segment	Significant	Maximum	Speed [m/s]	Direction [°]	Lateral	Vertical	Lateral	Vertical
0 - 10 minutes	59.2	105.4	16.6	104.1	3.9	1.4	7.9	6.5
10 - 20 minutes	70.2	129.8	17.8	104.2	6.2	1.5	12.8	5.7
20 - 30 minutes	72.6	130.3	17.3	105.1	8.5	1.7	16.7	6.9

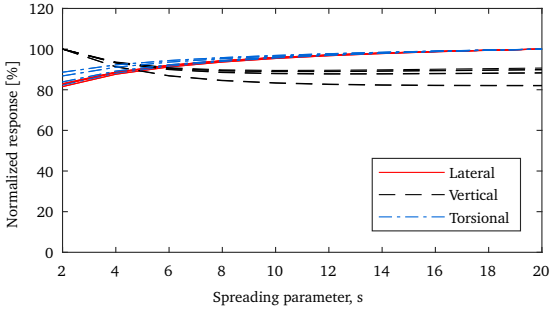

Fig. 7. Effect of spreading parameter on the standard deviations of lateral, vertical, and torsional accelerations. The standard deviations are normalized such that they are unity for the spreading parameter value of which they are at their maximum.

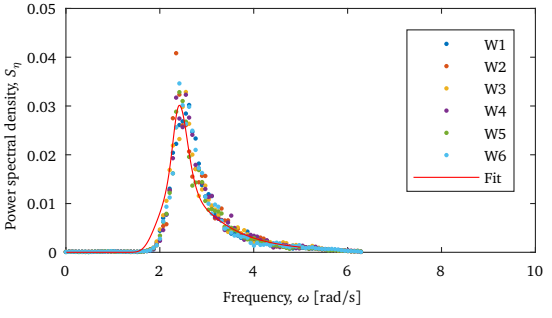

Fig. 8. Fitting of JONSWAP spectrum to the average of the power spectral density estimates obtained from the wave radars. The fitted curve corresponds to the values $\alpha = 0.0228$, $\gamma = 2.0885$, and $\omega_p = 2.0714$ rad/s. The spectral estimates are obtained by applying Welch's method with 20 divisions, Hanning window, and 50% overlap.

The JONSWAP spectrum obtained from fitting to the average of the estimates of the wave spectral densities is shown in Fig. 8. It would have also been reasonable to apply the estimated spectral densities directly, but to ensure a smooth spectrum and avoid a possible spurious resonant response, the use of a fitted spectrum was considered to be more robust.

Figs. 9-11 show the predicted and measured lateral, vertical and torsional response spectral densities of pontoons 2-4. Note that the y-axes in the three figures have different scalings. A good agreement is observed for the lateral acceleration, whereas the vertical acceleration prediction is decent with regard to integral area (variance) and shape but misses on the peak frequencies. The torsional acceleration is predicted with an accuracy that is far below satisfactory.

3.4. Global statistical assessment

The significant wave height, H_s, is the most important input parameter in the model for the wave excitation, and it is assumed to be the controlling parameter for the global statistical assessment of the response prediction. Because H_s does not sufficiently describe the sea state by itself, it is reasonable that variability in the measured response is observed for a given value. Variability in important factors, such as the peakedness of wave spectral density, the spreading and direction of the waves, and the inhomogeneity in the wave field, will all tend to increase the variability observed in the measured response. Furthermore, other excitation sources, such as wind and traffic, will produce excitation that is unaccounted for and that is in turn observed as variability.

It can be shown that the response of the bridge predicted using a first-order model set-up is linearly dependent on the significant wave height, given that the shape of the wave spectral density otherwise remains the same. However, in real life, the shape and peak period of the wave spectral density are dependent on the excitation level, which is characterized by the significant wave height.

The responses from the ULS and SLS design sea states specified in Section 3.1 were predicted only for the specified values of H_s.

The spectral estimates of all the recorded wave elevation time series were fitted to a JONSWAP spectrum to enable a statistical study of the parameters involved in the spectral description of the wave elevation. H_s-conditional probability density functions (PDFs) for T_p and γ were estimated by fitting lognormal PDFs to the histograms of the two parameters for specified ranges of H_s. The results are shown in Fig. 12. The data points for H_s and T_p are overlaid on the plot in Fig. 12a to indicate the appearance of the raw data. The effect of changing γ on the spectrum is illustrated in Fig. 13, where $H_s = 1.0$ m and $\omega_p = 2.07$ rad/s for all the plots. To justify the lognormal fitting, a single fit for all significant wave height values is shown in Fig. 14. This figure shows a very good fit to the lognormal distribution. A similarly good fit is obtained for T_p. By performing linear curve fits to the ridges of these PDFs, functions that relate the two parameters to the significant wave height were established such that the wave spectral density could be fully described by the significant wave height. The value of α in the JONSWAP spectrum is

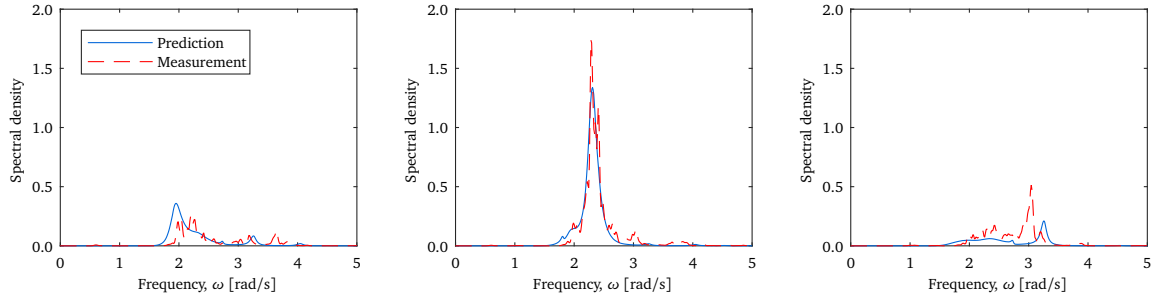

(a) Pontoon 2. (b) Pontoon 3. (c) Pontoon 4.

Fig. 9. Comparison between the measured and predicted lateral acceleration spectral densities from the selected recording, corresponding to the wave spectral density presented in Fig. 8.

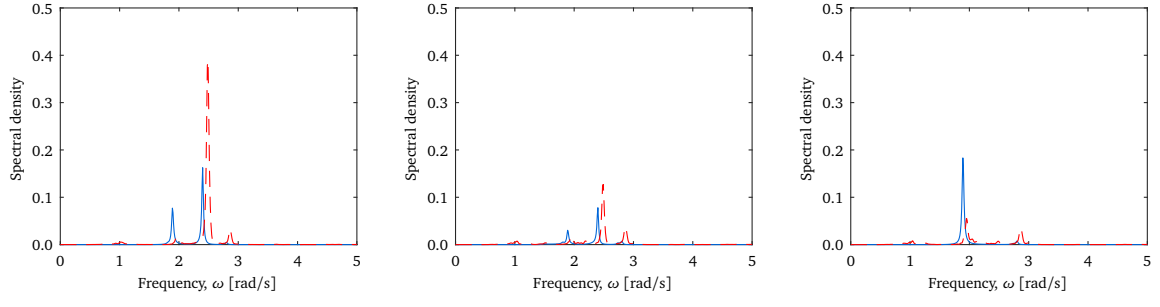

(a) Pontoon 2. (b) Pontoon 3. (c) Pontoon 4.

Fig. 10. Comparison between the measured and predicted vertical acceleration spectral densities from the selected recording, corresponding to the wave spectral density presented in Fig. 8. The legend is shown in Fig. 9.

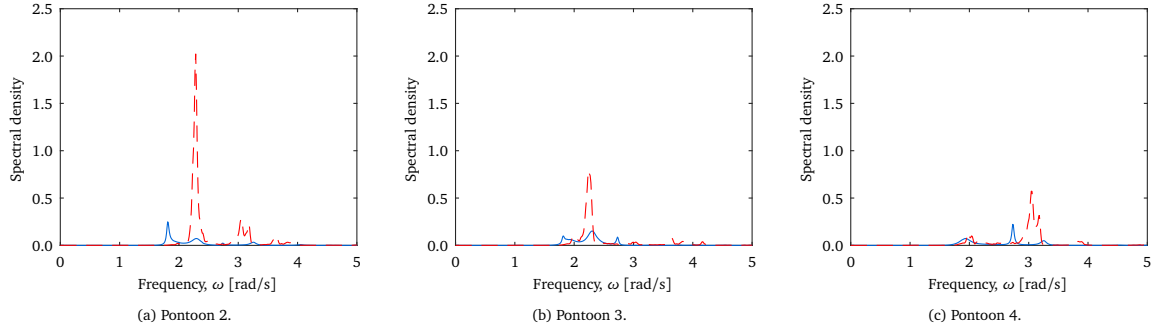

(a) Pontoon 2. (b) Pontoon 3. (c) Pontoon 4.

Fig. 11. Comparison between the measured and predicted torsional acceleration spectral densities from the selected recording, corresponding to the wave spectral density presented in Fig. 8. The legend is shown in Fig. 9.

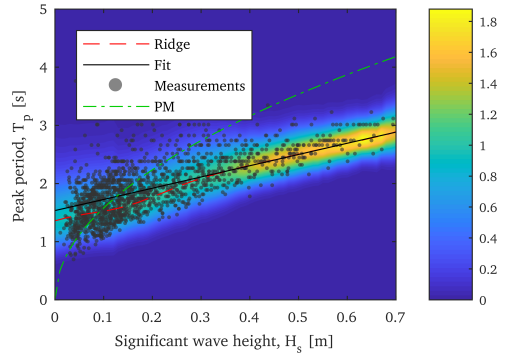

(a) $f_{T_p|H_s}(t_p,h_s)$. The fitted equation reads out $T_p = 1.53 + 1.93H_s$. The Pierson-Moskowitz (denoted PM) relation between peak period and significant wave height is also given. The data points are indicated by dots.

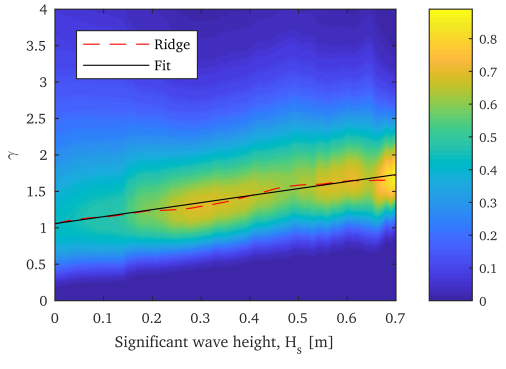

(b) $f_{\gamma|H_s}(\gamma,h_s)$. The fitted equation reads out $\gamma = 1.32 + 0.61H_s$.

Fig. 12. Estimated H_s-conditional probability density functions for peak period and peakedness factor. Both plots are based on fitting a lognormal distribution to data points with a significant wave height equal to $H_s \pm 0.1$ m, where H_s is represented by the x-axis. The data used are restricted to having a good fit to the JONSWAP spectrum, i.e., with $R^2 > 0.8$. Furthermore, a linear fit to the ridge of the probability density function is computed and shown in the plots. This fit is based on the sub-domain of the probability density function where $H_s > 0.4$ m.

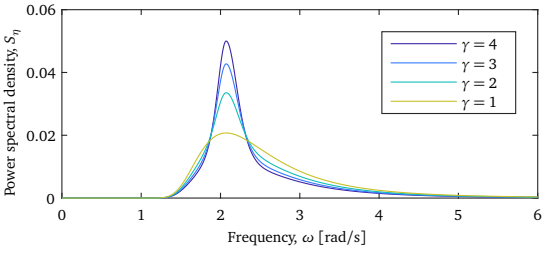

Fig. 13. JONSWAP spectrum for varying γ values. H_s and ω_p are set equal to those corresponding to the spectrum presented in Fig. 8.

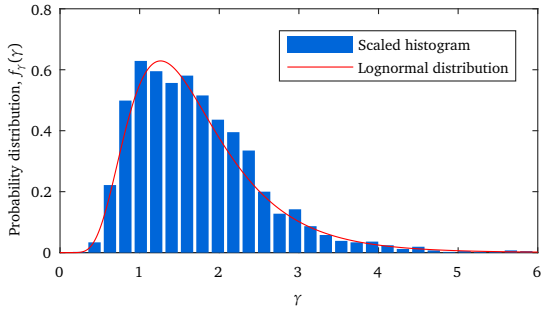

Fig. 14. Fit of γ from the JONSWAP spectra to a lognormal distribution. The set of obtained JONSWAP parameters used for the fitting were restricted to $\gamma < 6$ and $R^2 > 0.8$.

computed directly from the values of H_s and γ [14]. The plot also shows the relation between H_s and T_p specified in the one-parameter Pierson-Moskowitz spectrum [19]. This was used in conjunction with $\gamma = 1.7184$, which is the mean of the estimated γ values.

In essence, the following four different parameter sets were used for the predictions:

a. SLS design parameters, 1-year sea state
   $T_p = 4.6$ s, $\gamma = 4.5$, $H_s = 1.0$ m
b. ULS design parameters, 100-year sea state
   $T_p = 5.2$ s, $\gamma = 4.5$, $H_s = 1.41$ m
c. Parameters as functions of H_s
   $T_p = 1.53 + 1.93H_s$, $\gamma = 1.32 + 0.61H_s$
d. T_p as a function of H_s based on Pierson-Moskowitz (PM)
   $T_p = \left(\frac{5}{4}\frac{(2\pi)^4}{4\alpha g^2}\right)^{1/4} H_s^{1/2}$, $\gamma = 1.7184$ (mean of all γ)

All predictions are based on a directional distribution characterized by spreading parameter $s = 17$ and head sea, i.e., $\theta_0 = 90°$ (see Fig. 4).

Figs. 15-17 show the resulting predicted standard deviations of the lateral, vertical, and torsional accelerations, respectively, of pontoons 2–4 compared to the measured equivalents. The data points that correspond to the measurements are based on 30-minute-long time segments. The figure shows both the predictions performed with the JONSWAP spectrum used directly on all recordings, represented by blue dots, and for the four JONSWAP parameter sets denoted *a*-*d*.

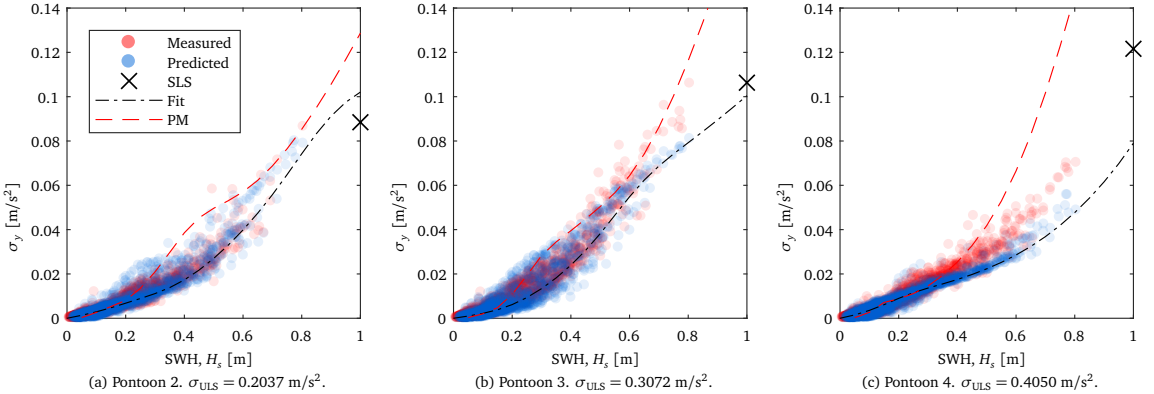

(a) Pontoon 2. $\sigma_{\text{ULS}} = 0.2037$ m/s^2. (b) Pontoon 3. $\sigma_{\text{ULS}} = 0.3072$ m/s^2. (c) Pontoon 4. $\sigma_{\text{ULS}} = 0.4050$ m/s^2.

Fig. 15. Comparison between the measured and predicted standard deviations of lateral accelerations. The points corresponding to the ULS ($H_s = 1.41$ m) are located outside the limits of the plots and are therefore indicated in the captions of the sub-figures.

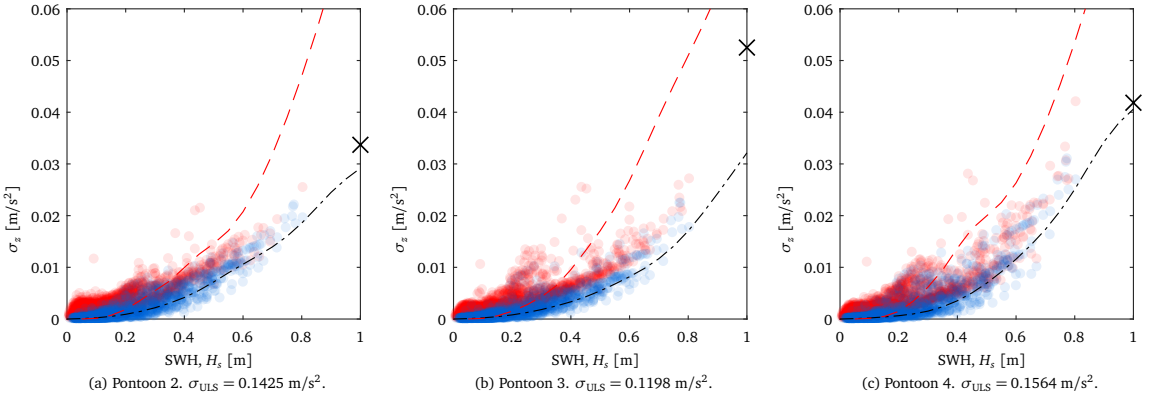

(a) Pontoon 2. $\sigma_{\text{ULS}} = 0.1425$ m/s^2. (b) Pontoon 3. $\sigma_{\text{ULS}} = 0.1198$ m/s^2. (c) Pontoon 4. $\sigma_{\text{ULS}} = 0.1564$ m/s^2.

Fig. 16. Comparison between the measured and predicted standard deviations of vertical accelerations. The points corresponding to the ULS ($H_s = 1.41$ m) are located outside the limits of the plots and are therefore indicated in the captions of the sub-figures. The legend is shown in Fig. 15.

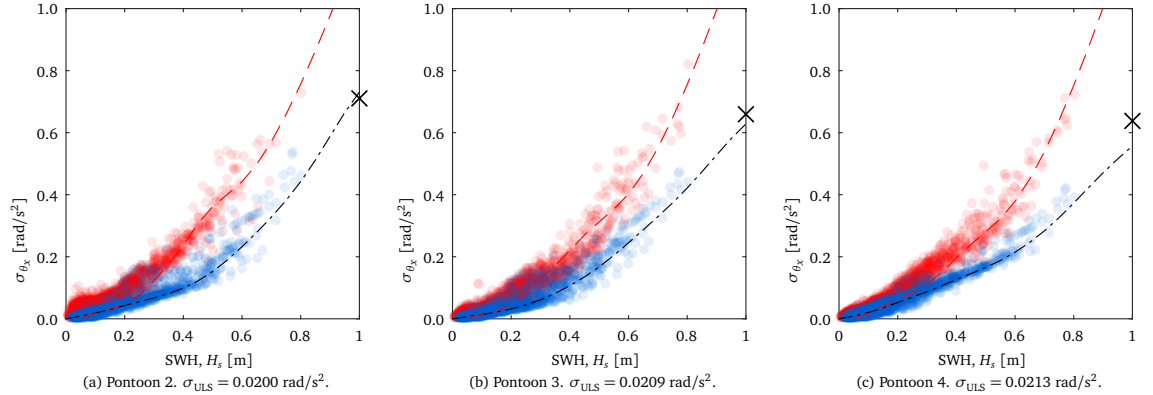

(a) Pontoon 2. $\sigma_{\text{ULS}} = 0.0200$ rad/s^2. (b) Pontoon 3. $\sigma_{\text{ULS}} = 0.0209$ rad/s^2. (c) Pontoon 4. $\sigma_{\text{ULS}} = 0.0213$ rad/s^2.

Fig. 17. Comparison between the measured and predicted standard deviations of torsional accelerations. The points corresponding to the ULS ($H_s = 1.41$ m) are located outside the limits of the plots and are therefore indicated in the captions of the sub-figures. The legend is shown in Fig. 15.

The plots reveal that the predictions based on the fitted γ and T_p values generally produce response values that are very close to those from the prediction based on the full parameter set. This general variability is assumed to be a direct consequence of the variability in the two parameters γ and T_p. Note that error sources explaining the discrepancy between the predictions and the measurements, such as model errors, possible nonlinearities, other excitation sources, errors in the directional distribution, and inhomogeneities, will not affect the goodness of fit between the responses computed using the simplified and full parameter sets.

The response prediction based on parameters taken from the SLS sea state (a), which is specified for $H_s = 1.0$ m, agrees well with the response for this excitation level based on both the fitted parameters and the full parameter set (blue dots) for most DOFs. The quality of the ULS (b) prediction is more difficult to assess because the specified excitation level, i.e., $H_s = 1.41$ m, is far above what is observed for any of the recordings. By using the specified fitted functions for γ and T_p (c), both the lateral and the vertical responses are predicted with a relatively high accuracy. The torsional response, however, is underpredicted. Because the predicted torsional response matches the predictions from the full parameter set very well, it is believed that the underestimation error is due to model inaccuracies rather than inaccuracies in the description of the wave excitation. The response predictions obtained from applying the Pierson-Moskowitz relation between H_s and T_p (d) do not match those from the full parameter set and are therefore considered to be inappropriate for an accurate prediction scheme. However, for this case study, it does serve as a conservative approach to simplify the probabilistic nature of the true sea state.

The R^2 value between the measured and predicted responses is computed for all measured DOFs and is presented in Fig. 18. Because many recordings exist in the low-excitation regime, which would heavily influence the results, the significant wave height is restricted to be above 0.15 m in the R^2 computation. This figure can be used to draw the same conclusion as from the other comparisons: the lateral acceleration is fairly well predicted, the vertical acceleration is decently predicted, and the torsional acceleration is predicted with an accuracy that is below satisfactory. This figure reveals that the predictions of the most important acceleration components, namely, the lateral, vertical and torsional accelerations, are close to symmetrical in their quality. This result implies that there are no systematic asymmetric inhomogeneities across the strait. If systematic inhomogeneities exist, they are therefore likely to be symmetric. It is also observed that the R^2 value that corresponds to the fourth pontoon is negative, which is a consequence of how R^2 is defined in Eq. 9: negative values simply imply that the average of the measurements is a better fit to the data than the prediction is.

4. Concluding remarks

The acceleration response of an existing floating pontoon bridge was predicted and compared with the corresponding measured acceleration response. For each recording, a JONSWAP spectrum was fitted to the average of the spectral density estimates from all wave radars. A $\cos^{2s}$ directional distribution with $s = 17$ and head sea was applied for all cases, which is justified by the fact that the spreading parameter affects the response to a relatively low extent.

A decent agreement was observed for the lateral and vertical responses, whereas the torsional acceleration is largely underpredicted, both when comparing the response spectral densities of a selected recording and when comparing the acceleration standard deviations within the range of the measured significant wave heights.

By fitting linear functions to describe the H_s relation to T_p and γ, H_s may be used as the only characterizing excitation parameter. This approach produced plots between the significant wave height and the standard deviation of the acceleration that for most DOFs were, on average, in agreement with the predictions performed using the full parameter set from the JONSWAP fit.

When retaining the full parameter set from the JONSWAP fitting and predicting the response for all recordings with a goodness of fit for the wave spectral density characterized by $R^2 > 0.8$, the overall fit of the predictions was assessed for each DOF. The analysis supported the results from the specific case comparison and the visual inspection: the accuracy of the prediction is good for the lateral component, decent for the vertical component, and poor for the torsional component.

ACKNOWLEDGEMENTS

This research was conducted with financial support from the Norwegian Public Roads Administration. The authors gratefully acknowledge this support.

REFERENCES

[1] I. Langen, R. Sigbjörnsson, On stochastic dynamics of floating bridges, Engineering Structures 2 (4) (1980) 209–216. doi:10.1016/0141-0296(80)90002-4.
URL http://www.sciencedirect.com/science/article/pii/0141029680900024

[2] K. A. Kvåle, R. Sigbjörnsson, O. Øiseth, Modelling the stochastic dynamic behaviour of a pontoon bridge: A case study, Computers & Structures 165 (2016) 123–135. doi:10.1016/j.compstruc.2015.12.009.
URL http://linkinghub.elsevier.com/retrieve/pii/S004579491500334X

[3] M. S. Seif, Y. Inoue, Dynamic analysis of floating bridges, Marine Structures 11 (1âĂŞ2) (1998) 29–46. doi:http://dx.doi.org/10.1016/S0951-8339(97)00012-9.
URL http://www.sciencedirect.com/science/article/pii/S0951833997000129

[4] B. J. Hartz, Dynamic Response of the Hood Canal Floating Bridge, in: Proceedings Second ASCE/EMD Specialty Conference on Dynamic Response of Structures, Atlanta, GA, 1981.

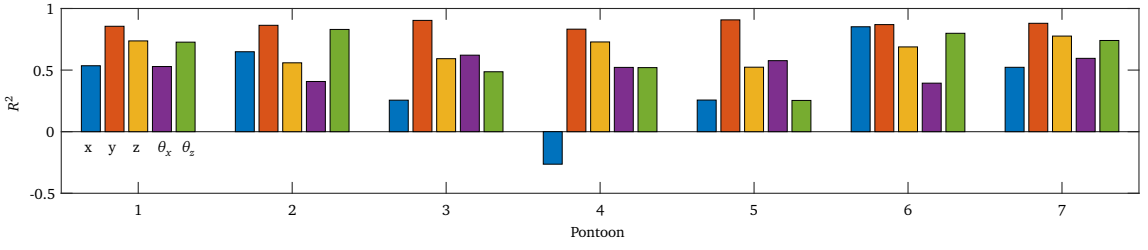

Fig. 18. Coefficient of determination between the standard deviations of the measured accelerations and the corresponding predictions based on a JONSWAP fit. Only recordings with $H_s > 0.15$ m are used to avoid the large cluster of low-excitation recordings from corrupting the result. The components are indicated under the bars corresponding to the first pontoon.

[5] E. R. Morris, A dynamic analysis of the Okanagan Lake floating bridge, Doctoral dissertation, University of British Columbia (1999).

[6] N. Kumamoto, T. Maruyama, Elastic response analysis method for floating bridges in waves (1999).

[7] E. Watanabe, T. Maruyama, H. Tanaka, S. Takeda, Design and construction of a floating swing bridge in Osaka, Marine Structures 13 (4-5) (2000) 437–458. doi:10.1016/S0951-8339(00)00016-2.
URL http://www.sciencedirect.com/science/article/pii/S0951833900000162

[8] C. Georgiadis, Wave Induced Vibrations of Continuous Floating Structures, Doctoral dissertation, University of Washington (1981).

[9] S. T. Peterson, Experimental response and analysis of the Evergreen Point floating bridge, Doctoral dissertation, Washington State University (2002).

[10] K. A. Kvåle, O. Øiseth, Structural monitoring of an end-supported pontoon bridge, Marine Structures 52 (2017) 188–207. doi:10.1016/j.marstruc.2016.12.004.
URL http://linkinghub.elsevier.com/retrieve/pii/S0951833916300284

[11] K. A. Kvåle, O. Øiseth, Characterization of the wave field around an existing end-supported pontoon bridge from simulated data, in: Proocedings of the International Conference on Earthquake engineering and Structural Dynamics, Reykjavik, Iceland, 2017.

[12] R. Sigbjörnsson, Stochastic theory of wave loading processes, Engineering Structures 1 (2) (1979) 58–64. doi:10.1016/0141-0296(79)90014-2.
URL http://www.sciencedirect.com/science/article/pii/0141029679900142

[13] K. Hasselmann, T. P. Barnett, E. Bouws, H. Carlson, D. E. Cartwright, K. Enke, J. A. Ewing, H. Gienapp, D. E. Hasselmann, P. Kruseman, Measurements of wind-wave growth and swell decay during the Joint North Sea Wave Project (JONSWAP), Tech. rep. (1973).

[14] C. T. Stansberg, G. Contento, S. Won Hong, M. Irani, S. Ishida, R. Mercier, Y. Wang, J. Wolfram, The Specialist Committee on Waves: Final Report and Recommendations to the 23rd ITTC, in: Proceedings of the 23rd ITTC, 2002, pp. 505–736.
URL http://ittc.info/media/1469/waves.pdf

[15] M. S. Longuet-Higgins, D. E. Cartwright, N. D. Smith, Observations of the directional spectrum of sea waves using the motions of a floating buoy, in: Proc. Conf. Ocean Wave Spectra, Prentice-Hall, 1963, pp. 111–132.

[16] Bruavdelingen, Vegdirektoratet, Prosjekteringsregler for anbudsfasen, Bergsøysundet bru, Møre og Romsdal fylke (1989).

[17] P. D. Welch, The use of fast Fourier transform for the estimation of power spectra: A method based on time averaging over short, modified periodograms (1967). doi:10.1109/TAU.1967.1161901.

[18] R. E. Walpole, R. H. Myers, S. L. Myers, K. Ye, Probability and statistics for engineers and scientists, 8th Edition, Pearson, 2007.

[19] W. J. Pierson, L. Moskowitz, A proposed spectral form for fully developed wind seas based on the similarity theory of S. A. Kitaigorodskii, Journal of Geophysical Research 69 (24) (1964) 5181–5190. doi:10.1029/JZ069i024p05181.
URL http://dx.doi.org/10.1029/JZ069i024p05181

Paper 5

Knut Andreas Kvåle, Ole Øiseth

"Characterization of the wave field around an existing end-supported pontoon bridge from simulated data"

Proocedings of the International Conference on Earthquake engineering and Structural Dynamics, Reykjavik, Iceland, 2017.

International Conference on Earthquake engineering and Structural Dynamics
in honour of late Prof. Ragnar Sigbjörnsson
12-14 June 2017, Reykjavik, Iceland

Characterization of the wave field around an existing end-supported pontoon bridge from simulated data

K.A. Kvåle & O. Øiseth
Department of Structural Engineering, Faculty of Engineering Science and Technology, NTNU, Norwegian University of Science and Technology, Trondheim, Norway

knut.a.kvale@ntnu.no
ole.oiseth@ntnu.no

ABSTRACT:

The environmental excitation and the dynamic response are currently being monitored on the Bergsøysund Bridge, an existing end-supported pontoon bridge. Wave radars are monitoring the one-point sea surface elevation at six different locations. As the wave excitation is considered the main concern for vibration-based design of similar bridges, an appropriate description of the sea state characterizing the wave excitation is crucial. Furthermore, it is considered a necessity for an assessment of the quality of response predictions by comparison with measurements. In the current paper, time simulations of wave elevation are used to identify the already-known sea states. The Fourier Expansion Method (FEM) and Extended Maximum Entropy Principle (EMEP) are applied for this purpose. The results provide valuable insights about both the identification methods and the sensor layout.

Keywords: wave modelling, floating bridge, wave field, wave spreading

1. INTRODUCTION

Pontoon bridges may help to overcome the ever-increasing challenges of modern bridge engineering, by utilizing the buoyancy of the water. The subject of water waves is well-described and thoroughly discussed in the scientific world, but the vast knowledge is not necessarily accessible to the bridge engineer society. The simulation techniques available are mainly verified on structures of limited physical reach, and studies attempting to verify simulated floating bridge behaviour are very scarce. The waves will in most cases represent the main excitation source for low pontoon bridges, even though traffic and wind excitation also will play significant roles for certain structures. To be able to verify the simulated behaviour of a floating bridge, the identification of the wave excitation is a crucial sub-task to solve. The wave excitation is commonly assumed directly dependent on the sea surface elevation, such that a successful characterization of the wave field surrounding the investigated structure will be sufficient for this purpose.

The Bergsøysund Bridge is an existing end-supported pontoon bridge, and is the structure under consideration in the current paper. The bridge is currently extensively instrumented to capture the environmental excitation sources acting on it and its dynamic response. In the current paper, no data from the monitoring system will be analysed. However, the geometry and positions of the wave radars will be used in conjunction with simulated realistic sea states, to assess how well the methods can capture the parameters of the simulated sea state with the current sensor set-up. Should they fail to identify the benchmark cases, a revision of the layout would have to be considered. The experience drawn from this will be highly valuable when later comparing response predictions with monitored response. The two-dimensional directional wave spectral density is the quantity that is attempted identified in the current paper. Aspects regarding the simulation of wave data important for a realistic benchmark situation are discussed.

2. THE BERGSØYSUND BRIDGE

The Bergsøysund Bridge is a pontoon bridge that links the islands Aspøya and Bergsøya on the west-coast of Norway (62°59'12.8"N, 7°52'26.5"E). The 931 meters long bridge (Figure 1), constructed by a steel truss which is supported on 7 lightweight concrete pontoons, has been in operation for nearly 25 years.

Lack of side support makes the bridge particularly interesting. The bridge is extensively monitored by means of accelerometers, anemometers, wave radars, and a single global navigation satellite system (GNSS) displacement sensor. Wave radars are monitoring the single-point wave elevation at 6 locations, as indicated in Figure 2 and Table 1. The monitoring system is extensively described in zKvåle and Øiseth (2017). Other work on the Bergsøysund Bridge include simulation studies (Kvåle et al., 2016) and identification of the modal parameters (Kvåle et al., 2017; Kvåle et al., 2017b; Kvåle et al., 2015).

Figure 1. The Bergsøysund Bridge. Photograph by NTNU/K.A. Kvåle.

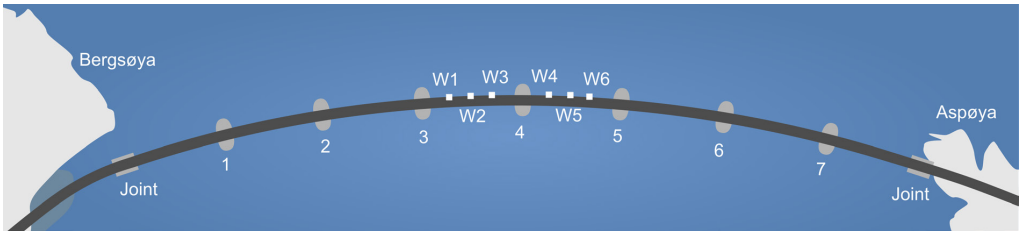

Figure 2. Wave radar layout.

Table 1. Coordinates of wave radars. The origin is located on top of the bridge deck, midspan, with positive x pointing tangential to the bridge and towards Aspøya.

Sensor	x [m]	y [m]	z [m]
W1	-73.0	-1.1	-6.2
W2	-53.0	-0.1	-6.2
W3	-33.0	0.6	-6.2
W4	33.0	0.6	-6.2
W5	53.0	-0.1	-6.2
W6	73.0	-1.1	-6.2

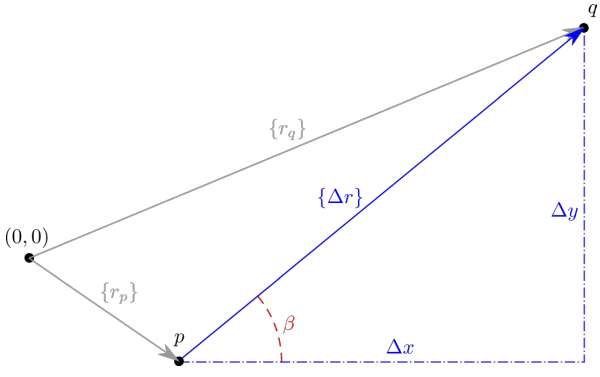

Figure 3. Points p and q on the sea surface.

3. DESCRIBING IRREGULAR SEA SURFACE ELEVATION

3.1 Stochastic description of irregular sea surface elevation

A thorough review of relevant theory of stochastic modelling of irregular sea surfaces is given by Hauser et al. (2005), but the details required to illustrate how the methods work are repeated in the following. More details can be found in, e.g., Longuet-Higgins et al. (1963) and Sigbjörnsson (1979).

The random sea surface elevation is modelled as a function of location in space $\{r\}$ and time t, and can be expressed mathematically as follows:

$$\eta(\{r\},t) = \int e^{i\{\kappa\}\cdot\{r\}-i\omega t} dZ_\eta(\{\kappa\},\omega) \tag{1}$$

where the wave number vector $\{\kappa\}$, the circular frequency ω, and the spectral process corresponding to the sea surface elevation Z_η, are introduced. For stationary and homogeneous random wave fields, this spectral process is related to the wave spectral density in the following manner:

$$E\left(dZ_{\eta_p}(\{\kappa\},\omega)dZ_{\eta_q}(\{\kappa\},\omega)^H\right) = S_{pq}(\{\kappa\},\omega)d\kappa_x d\kappa_y d\omega \tag{2}$$

The cross-spectral density between the wave elevations at the probing locations p and q, separated by the distance vector $\{\Delta r\}$, as depicted in Figure 3, is written as follows:

$$S_{pq}(\omega) = \int_{-\pi}^{\pi} S_\eta(\omega,\theta)\gamma_{pq}(\omega,\theta)d\theta = \int_{-\pi}^{\pi} S_\eta(\omega,\theta)e^{i\{\kappa\}\cdot\{\Delta r\}}d\theta \tag{3}$$

where $\gamma_{pq}(\omega,\theta)$ is introduced as a 2D coherence function distributed over directions, and the following definitions are introduced:

$$\{\Delta r\} = \begin{Bmatrix}\Delta x\\ \Delta y\end{Bmatrix},\ \{\kappa\} = \kappa\begin{Bmatrix}\cos\theta\\ sin\theta\end{Bmatrix} \tag{4}$$

Here, $\{\Delta r\} = \{r_q\} - \{r_p\}$, such that Δx and Δy give the distances in x- and y-direction between the points under investigation. Under the assumption of the dispersion relation and deep-water waves, the wave number κ can be written as follows for $\omega > 0$:

$$\kappa = \frac{\omega^2}{g} \tag{5}$$

Equation 2 can be rewritten using angle and frequency (2D) rather than frequency and wave number vector (3D), as follows:

$$E\left(dZ_{\eta_p}(\omega,\theta)dZ_{\eta_q}(\omega,\theta)^H\right) = S_{pq}(\omega,\theta)d\theta d\omega \tag{6}$$

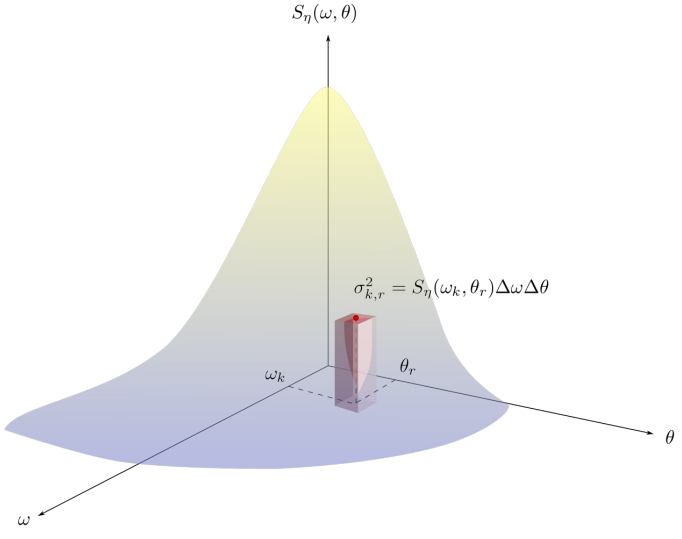

Figure 4. Simulation amplitude sampling.

3.2 Time simulation of sea surface elevations from a stochastic description

The starting point for the simulation is the mathematical expression of the sea surface elevation given in Equation 1. From Equation 6, the amplitude corresponding to the contribution to the total wave elevation, from a regular wave with frequency ω and direction of propagation θ, within the region defined by $\Delta\omega$ and $\Delta\theta$, is found as follows:

$$a(\omega,\theta) = \sqrt{2S_\eta(\omega,\theta)\Delta\omega\Delta\theta} \tag{7}$$

This is illustrated in Figure 4. Relying on this, a realization of the sea state can be simulated as follows:

$$\eta(\{x\},t) = \sum_{k=1}^{N}\sum_{r=1}^{R}\sqrt{2S_\eta(\omega,\theta)\Delta\omega\Delta\theta}\, e^{i\kappa\{\sin\theta,\cos\theta\}\cdot\{x\}+i\alpha} e^{-i\omega t} \tag{8}$$

where the following decomposition is usually applied: $S\eta(\omega,\theta) = S\eta(\omega)D(\omega,\theta)$. Furthermore, the expression inside the sum can be discretized, as follows:

$$\eta(\{x\},t) = \sum_{k=1}^{N}\left[\sum_{r=1}^{R}\sqrt{2S_\eta(\omega,\theta)\Delta\omega\Delta\theta}\,\exp(i\kappa\{\sin\theta_r,\cos\theta_r\}\cdot\{x\}+i\alpha_r)\right] e^{-i2\pi(k-1)n/N} \tag{9}$$

This is simply the FFT of the following expression:

$$B_k = \left[\sum_{r=1}^{R}\sqrt{2S_\eta(\omega,\theta)\Delta\omega\Delta\theta}\,\exp(i\kappa\{\sin\theta_r,\cos\theta_r\}\cdot\{x\}+i\alpha_r)\right] \tag{10}$$

The approach described above is commonly referred to as the double summation method. The method results in a non-ergodic simulated wave elevation (Jefferys, 1987; Nwogu, 1989). The method is, however, very efficient due to the utilization of the FFT algorithm, and is considered sufficient for the current case study. The time domain simulations in the current study have durations of 30 minutes, and are simulated with a sampling rate of 2 Hz.

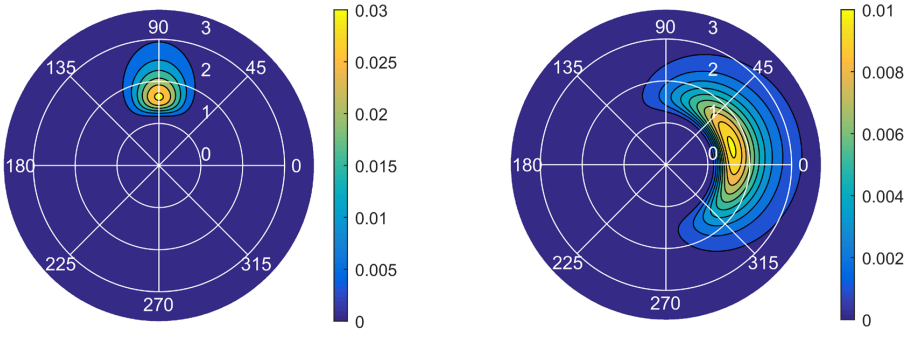

(a) Case 1: $H_s = 0.6m,\ s = 30,\ \theta_0 = 90°$.

(b) Case 2: $H_s = 0.6m,\ s = 3,\ \theta_0 = 15°$.

Figure 5. Modelled two-dimensional wave spectral density.

4. IDENTIFICATION OF WAVE PARAMETERS FROM SINGLE-POINT ELEVATIONS

Both applied methods rely on the estimation of the cross-spectral densities between pairs of wave elevations, a task considered as relatively uncertain for finite length time series. To estimate the spectral density, Welch's method, with 60 sub-divisions combined with a zero-padding factor of 8, was used.

4.1 Modelled sea state

The directional wave spectral density is assumed to be characterized by the one-parameter Pierson-Moskowitz wave spectral density (Pierson and Moskowitz, 1964) and the cos2s directional distribution (Longuet-Higgins et al., 1963), as follows:

$$S_\eta(\omega) = \frac{A}{\omega^5} e^{-B/\omega^4} \tag{11}$$

$$\mathrm{D}(\theta) = \mathrm{C}\cos^{2s}\left(\frac{\theta-\theta_0}{2}\right) \tag{12}$$

where $A = \alpha g^2$; $B = 3.11/H_s^2$; $\alpha = 0.0081$; H_s is the significant wave height (SWH), the mean wave height of the highest third of the waves; C is a constant ensuring that the integral of the distribution is 1; s is the spreading parameter, describing the spreading of the waves; and θ_0 is the mean wave direction. Two different cases were modelled, characterized by the following parameters:

1. $H_s = 0.6m,\ s = 30,\ \theta_0 = 90°$
2. $H_s = 0.6m,\ s = 3,\ \theta_0 = 15°$

The resulting directional wave spectral densities are illustrated in Figure 5.

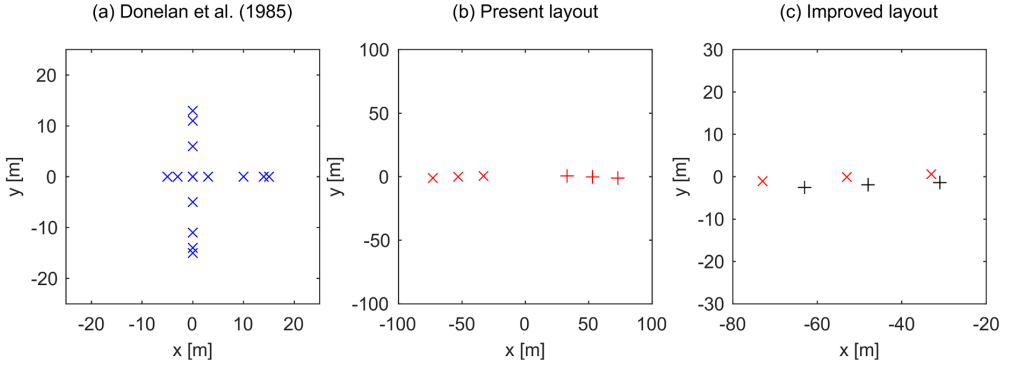

Figure 6. Sensor layout.

4.2 Initial assessment of the current sensor layout

According to Goda (1981) and Massel and Brinkman (1998), the layout of a spatial array can be optimized by cohering to the following guidelines:

1. No wave radar pair should have the same distance vector $\{\Delta r\}$.
2. The distance vectors should be distributed uniformly in the widest possible range.
3. The minimum distance between a pair of wave radars should be below one quarter of the shortest wave component to consider. This implies that the largest distance between a wave radar pair should be $|\{\Delta r\}| < l_{\max} = \frac{1}{4}\lambda_{\min} = \frac{1}{4}\frac{2\pi}{\kappa_{\max}} = \frac{\pi g}{2\omega_{\max}^2}$, where $\lambda_{\min}$ is the minimum relevant wave length, $\kappa_{\max}$ (via. Airy wave theory) and $\omega_{\max}$ (via. the dispersion relation for deep-water waves) the corresponding maximum peak wave number and maximum peak frequency, respectively.

Due to the circular pattern of the sensor layout, guideline 1 is strictly speaking fulfilled, even though many of the distance vectors are very similar. Guideline 2 is not fulfilled: the distance vectors are all close to being solely along the x-direction, and many have equal lengths. The largest peak frequency is close to $1.6\frac{rad}{s}$, implying that the distance between wave radar pairs should be constrained by $6m$, per guideline 3, something the layout does not fulfil.

Both a reference layout suggested by Donelan et al. (1985), the existing sensor layout, and a modified sensor layout will be considered. All layouts are depicted in Figure 6. The cited reference layout was originally designed for common deep-water waves with peak periods less than 4s, and consists of 14 sensors in total. A comparison with a 6-sensor layout is therefore not fair, but is merely included to illustrate the possibilities of the methods.

4.3 Fourier Expansion Method

The Fourier Expansion Method (FEM) was first introduced as a method for the characterization of the directional wave spectral density by Longuet-Higgins et al. (1963), and has been discussed, reformulated and applied in numerous cases since then (Barber, 1963; Ochi, 2005; Panicker and Borgman, 1970; Young, 1994). Normally, it is written using the Fourier series defined as sums of sines and cosines. Below, an approach based on the Fourier series as a sum of complex exponentials is presented. The success of this modified procedure relies on proper handling of complex numbers in the numerical pseudo-inverse procedure, but has the benefit that it yields more elegant mathematical expressions.

4.3.1 Theoretical outline

The 2D spectral density is first expressed as a truncated Fourier series, as follows:

$$S(\omega,\theta) = \sum_{n=-N}^{N} c_n(\omega) e^{in\theta} \tag{13}$$

By combination with the cross-spectral density between elevations at points p and q found in Eq. 3, this gives the following:

$$S_{pq}(\omega) = \int_{-\pi}^{\pi} \sum_{n=-N}^{N} c_n(\omega) e^{in\theta}\, \mathrm{e}^{i\{\kappa\}\cdot\{\Delta r\}}\, d\theta \tag{14}$$

This is written out explicitly, for factorization, as follows:

$$\begin{aligned} S_{pq}(\omega) &= \int_{-\pi}^{\pi} c_{-N}\cdot e^{i(-N)\theta}\gamma_{pq} + c_{-N+1}\cdot e^{i(-N+1)\theta}\gamma_{pq} + \cdots + c_{N-1}\cdot e^{i(N-1)\theta}\gamma_{pq} + c_N\cdot e^{iN\theta}\gamma_{pq}\, d\theta \\ &= \int_{-\pi}^{\pi} \gamma_{pq} e^{i(-N)\theta} d\theta\, c_{-N} + \int_{-\pi}^{\pi} \gamma_{pq} e^{i(-N+1)\theta} d\theta\, c_{-N+1} + \cdots + \int_{-\pi}^{\pi} \gamma_{pq} e^{iN\theta} d\theta\, c_N \\ &= \sum_{n=-N}^{N} \Big(\int_{-\pi}^{\pi} \gamma_{pq}(\omega,\theta) e^{in\theta} d\theta\, c_n(\omega) \Big) \end{aligned} \tag{15}$$

For illustrational purposes, this is written using matrix notation, with three sensors, and evaluated at the chosen discrete frequency component ω_k:

$$\begin{Bmatrix} S_{12} \\ S_{13} \\ S_{23} \end{Bmatrix}_k = \begin{bmatrix} I_{12,-N}(\omega_k) & I_{12,-N+1}(\omega_k) & \cdots & I_{12,0}(\omega_k) & \cdots & I_{12,N}(\omega_k) \\ I_{13,-N}(\omega_k) & I_{13,-N+1}(\omega_k) & \cdots & I_{13,0}(\omega_k) & \cdots & I_{13,N}(\omega_k) \\ I_{23,-N}(\omega_k) & I_{23,-N+1}(\omega_k) & \cdots & I_{23,0}(\omega_k) & \cdots & I_{23,N}(\omega_k) \end{bmatrix} \begin{Bmatrix} c_{-N} \\ c_{-N+1} \\ \vdots \\ c_0 \\ \vdots \\ c_{N-1} \\ c_N \end{Bmatrix}_k \tag{16}$$

Here, $I_{pq,n}(\omega) = \int_{-\pi}^{\pi} \gamma_{pq}(\omega,\theta) e^{in\theta} d\theta$ is introduced for convenience. This equation system can be solved as a linear least squares problem, using pseudo-inverse when underdetermined. It can be shown that this integral can be solved using Bessel integrals of the first kind $J_n(z)$, as follows:

$$I_{pq,n}(\omega) = e^{in\beta} i^n 2\pi J_n\left(\frac{\omega^2}{g} l\right) \tag{17}$$

where β is the angle and l is the length of the vector $\{\Delta r\}$ between locations p and q, as indicated in Figure 3. This ensures a more robust numerical computation of the integral, avoiding accuracy problems associated with the rapid oscillation of the exponential integrand with respect to the angle, as reported by Giske et al. (2017). The choice of the number of Fourier coefficients included, defined by the constant N, affects the resulting 2D wave spectral density. N was set to 4 for all following applications.

4.3.2 Application of the FEM on simulated data

Figure 7 shows directional wave spectral densities estimated using the FEM, based on cross-spectral densities established from time simulations with the reference layout. When the cross-spectral densities are computed directly, the resulting 2D spectral density match nearly perfectly with the source. Thus, the discrepancies observed in the figure are assumed to be artefacts originating from the spectral estimation. The overall agreement is good, but as reported in the literature, the FEM method yields results with a narrower directional distribution, and thus indicating more spreading, than what is correct.

The current layout proves unable to yield any results when relying on cross-spectral densities estimated from time simulations. In Figure 8, the FEM is therefore applied on the directly computed cross-spectral densities for points corresponding to the current layout. For case 1, the results are very poor, and the only conclusion that can be drawn from it is that the sea state represents a head sea, possibly approaching either from land or sea. For case 2, however, a decent result is obtained.

4.4 Maximum Entropy Principle

The Maximum Entropy Principle (MEP), also commonly referred to as the Maximum Entropy Method (MEM), was first applied for the determination of directional wave spectral density by Kobune and Hashimoto (1986). The MEP, which originally was developed for three-quantity point measurements, was thereafter reformulated for wave sensor arrays by Nwogu (1989). Hashimoto et al. (1994) introduced the Extended MEP (EMEP), which deals with the errors in the cross-spectral densities and thus makes it more robust. The implementation of the EMEP found in the DIWASP toolbox for MATLAB (Johnson, 2002) was used in the current paper, which is based on the mentioned paper by Hashimoto et al. (1994). In the current paper, no further description of the methodology is given.

4.4.1 Application of the EMEP on simulated data

The directional wave spectral densities estimated from simulated data on the current sensor layout with the EMEP algorithm are illustrated in Figure 9. Due to difficulties in proper estimates of the cross-spectral densities of the wave elevations at the sensor locations, which are less smooth for large distances, gaps are observed for certain frequency ranges in the resulting directional wave spectral density. Furthermore, contrary to what is found when applying the FEM, the sea state indicating head sea (case 1) is much more accurately identified than the one characterized by obliquely approaching waves (case 2). It is noted that the EMEP algorithm is superior to the FEM for the identification of both the simulated cases.

As indicated in Section 4.2, the sensor layout may be improved. A suggested new sensor layout is depicted in Figure 6c. In the new layout, three aspects are improved: (1) the distance vectors are more uniformly distributed; (2) the anisotropy of the sensor positioning is reduced as the distance vectors are less purely longitudinal; and (3) the maximum distances between sensor pairs are reduced. The result from the

EMEP algorithm with this layout is depicted in Figure 10. The new layout is in general found to be much more robust for the identification of both simulated test cases. The increased robustness of the spectral estimation, due to shorter distances between the sensors, is believed to be the main cause of this.

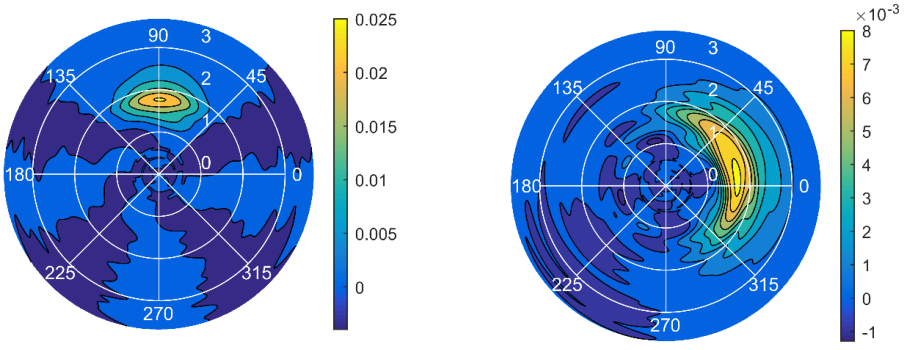

(a) Case 1: $H_s = 0.6m,\ s = 30,\ \theta_0 = 90°$. (b) Case 2: $H_s = 0.6m,\ s = 3,\ \theta_0 = 15°$.

Figure 7. FEM with sensor layout suggested by Donelan et al. (1985).

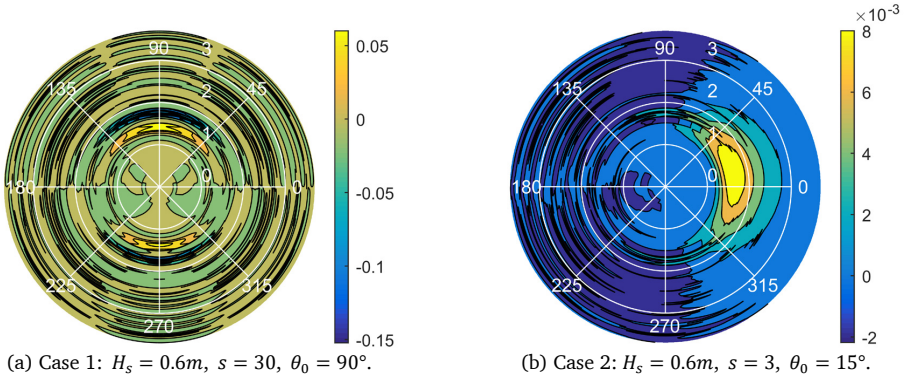

(a) Case 1: $H_s = 0.6m,\ s = 30,\ \theta_0 = 90°$. (b) Case 2: $H_s = 0.6m,\ s = 3,\ \theta_0 = 15°$.

Figure 8. FEM with current sensor layout, based on direct computation of cross-spectral densities.

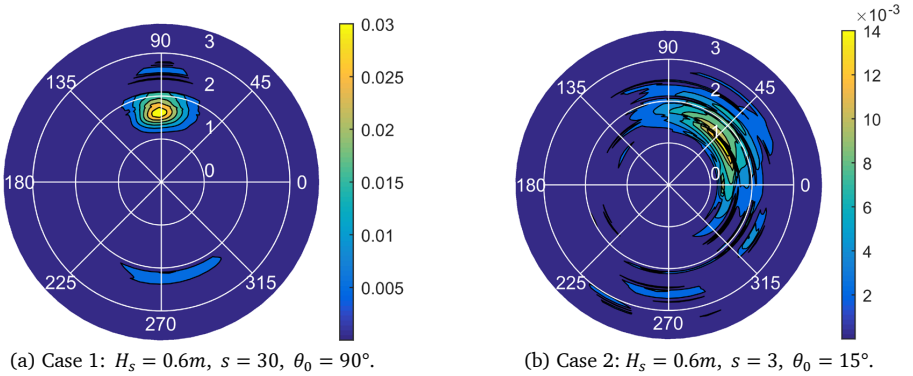

(a) Case 1: $H_s = 0.6m,\ s = 30,\ \theta_0 = 90°$. (b) Case 2: $H_s = 0.6m,\ s = 3,\ \theta_0 = 15°$.

Figure 9. EMEP with current sensor layout.

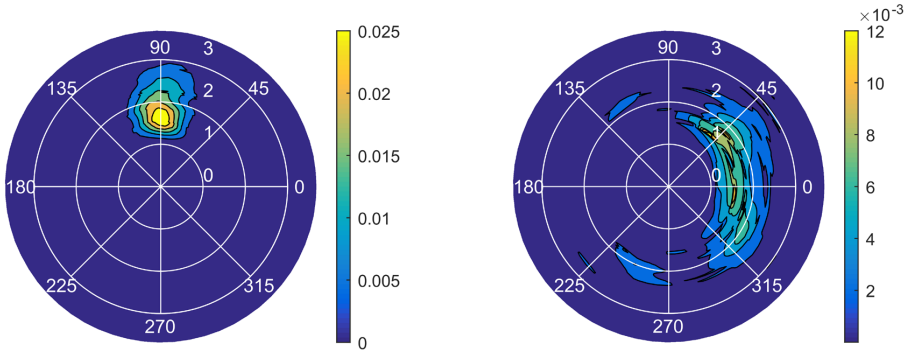

(a) Case 1: $H_s = 0.6m,\ s = 30,\ \theta_0 = 90°$.

(b) Case 2: $H_s = 0.6m,\ s = 3,\ \theta_0 = 15°$.

Figure 10. EMEP with improved sensor layout.

5. CONCLUDING REMARKS

Two well-established methods for determination of the directional wave spectral density, namely the Fourier Expansion Method (FEM) and the Extended Maximum Entropy Principle (EMEP), have been applied on simulated data for the existing wave radar layout on the Bergsøysund Bridge.

The FEM fails to identify the simulated directional spectral density from cross-spectral density estimates based on time simulations, when assuming a sensor layout as is presently installed on the bridge. However, for direct calculation of the cross-spectral densities, the FEM correctly characterizes the sea state when the waves are approaching with an oblique angle to the bridge. This is not the case for a head sea situation, where the method fails also when applying the cross-spectral densities directly. With the selected reference sensor layout, the head sea state (case 1) is estimated as slightly more directionally spread out than correct, an artefact commonly observed with the FEM. The EMEP successfully identifies the head sea state (case 1), but does not reliably identify the sea state characterized by obliquely approaching waves (case 2). However, it performs significantly better than the FEM, also for case 2.

The current layout has a large weakness in its anisotropic distribution, such that mean wave direction plays a major role in the success of the identification. A new layout is suggested to solve this. The suggested new layout results in a more robust estimation of the cross-spectral densities, which in turn improves the quality of the resulting directional spectral densities.

Both methods rely on good estimates of cross-spectral densities, which is a task that requires both experience, skill and sometimes luck. The resulting two-dimensional wave spectral density, and thus directional distribution, is highly dependent on this estimation procedure, i.e., the estimator methods and parameters used.

5.1 Future work

Recordings from the sensors acting on site should be analysed in a similar manner to characterize the wave field on site. The current work represents an important step towards this.

ACKNOWLEDGEMENTS

The research is funded by the Norwegian Public Roads Administration. The authors gratefully acknowledge this. We would also like to thank our dear colleague, the late Prof. Ragnar Sigbjörnsson, for his commitment and inspiration in common scientific endeavours.

REFERENCES

Barber NF (1963) The directional resolving power of an array of wave detectors.

Donelan MA, Hamilton J, Hui WH (1985) Directional Spectra of Wind-Generated Waves. Philosophical Transactions of the Royal Society of London. Series A, Mathematical and Physical Sciences, 315(1534): pp 509–562. https://doi.org/10.1098/rsta.1985.0054

Giske F-IG, Leira BJ, Øiseth O (2017) Efficient computation of cross-spectral densities in the stochastic modelling

of waves and wave loads. Applied Ocean Research, 62 pp 70–88. https://doi.org/10.1016/j.apor.2016.11.007

Goda Y (1981) Simulation in examination of directional resolution. In Proceedings of the Conference on Directional Wave Spectra Applications, (pp. 387–407).

Hashimoto N, Nagai T, Asai T (1994) Extension of the maximum entropy principle method for directional wave spectrum estimation. Coastal Engineering Proceedings, 1(24):.

Hauser D, Kahma K, Krogstad HE (2005) Measuring and analysing the directional spectra of ocean waves. Luxembourg: Publications Office of the European Union.

Jefferys ER (1987) Directional seas should be ergodic. Applied Ocean Research, 9(4): pp 186–191. https://doi.org/http://dx.doi.org/10.1016/0141-1187(87)90001-0

Johnson D (2002) DIWASP, a directional wave spectra toolbox for MATLAB®: User Manual. Center for Water Research, University of Western Australia.

Kobune K, Hashimoto N (1986) Estimation of directional spectra from the maximum entropy principle.

Kvåle KA, Sigbjörnsson R, Øiseth O (2016) Modelling the stochastic dynamic behaviour of a pontoon bridge: A case study. Computers & Structures, 165 pp 123–135. https://doi.org/10.1016/j.compstruc.2015.12.009

Kvåle KA, Øiseth O (2017) Structural monitoring of an end-supported pontoon bridge. Marine Structures, 52 pp 188–207. https://doi.org/10.1016/j.marstruc.2016.12.004

Kvåle KA, Øiseth O, Rønnquist A (2017) Operational modal analysis of an end-supported pontoon bridge. Engineering Structures, 148 pp 410–423. https://doi.org/10.1016/j.engstruct.2017.06.069

Kvåle KA, Øiseth O, Rönnquist A (2017) Covariance-Driven Stochastic Subspace Identification of an End-Supported Pontoon Bridge Under Varying Environmental Conditions. In J. Caicedo & S. Pakzad (Eds.), Dynamics of Civil Structures, Volume 2. Conference Proceedings of the Society for Experimental Mechanics Series. (pp. 107–115). Cham: Springer International Publishing. https://doi.org/10.1007/978-3-319-54777-0_14

Kvåle KA, Øiseth O, Rønnquist A, Sigbjörnsson R (2015) Modal Analysis of a Floating Bridge Without Side-Mooring. In Dynamics of Civil Structures, Volume 2 (Vol. 2, pp. 127–136). Springer. https://doi.org/10.1007/978-3-319-15248-6_14

Longuet-Higgins MS, Cartwright DE, Smith ND (1963) Observations of the directional spectrum of sea waves using the motions of a floating buoy. In Proc. Conf. Ocean Wave Spectra (pp. 111–132). Prentice-Hall.

Massel SR, Brinkman RM (1998) On the determination of directional wave spectra for practical applications. Applied Ocean Research, 20(6): pp 357–374. https://doi.org/10.1016/S0141-1187(98)00026-1

Nwogu O (1989) Maximum entropy estimation of directional wave spectra from an array of wave probes. Applied Ocean Research, 11(4): pp 176–182. https://doi.org/10.1016/0141-1187(89)90016-3

Ochi MK (2005) Ocean waves: the stochastic approach (Vol. 6). Cambridge University Press.

Panicker NN, Borgman LE (1970) DIRECTIONAL SPECTRA FROM WAVE-GAGE ARRAYS. Coastal Engineering Proceedings; No 12 (1970): Proceedings of 12th Conference on Coastal Engineering, Washington, D.C., 1970. Retrieved from https://journals.tdl.org/icce/index.php/icce/article/view/2612

Pierson WJ, Moskowitz L (1964) A proposed spectral form for fully developed wind seas based on the similarity theory of S. A. Kitaigorodskii. Journal of Geophysical Research, 69(24): pp 5181–5190. https://doi.org/10.1029/JZ069i024p05181

Sigbjörnsson R (1979) Stochastic theory of wave loading processes. Engineering Structures, 1(2): pp 58–64. https://doi.org/10.1016/0141-0296(79)90014-2

Young IR (1994) On the measurement of directional wave spectra. Applied Ocean Research, 16(5): pp 283–294. https://doi.org/10.1016/0141-1187(94)90017-5

DEPARTMENT OF STRUCTURAL ENGINEERING
NORWEGIAN UNIVERSITY OF SCIENCE AND TECHNOLOGY

N–7491 TRONDHEIM, NORWAY
Telephone: +47 73 59 47 00 Telefax: +47 73 59 47 01

"Reliability Analysis of Structural Systems using Nonlinear Finite Element Methods",
C. A. Holm, 1990:23, ISBN 82-7119-178-0.

"Uniform Stratified Flow Interaction with a Submerged Horizontal Cylinder",
Ø. Arntsen, 1990:32, ISBN 82-7119-188-8.

"Large Displacement Analysis of Flexible and Rigid Systems Considering Displacement-Dependent Loads and Nonlinear Constraints",
K. M. Mathisen, 1990:33, ISBN 82-7119-189-6.

"Solid Mechanics and Material Models including Large Deformations",
E. Levold, 1990:56, ISBN 82-7119-214-0, ISSN 0802-3271.

"Inelastic Deformation Capacity of Flexurally-Loaded Aluminium Alloy Structures",
T. Welo, 1990:62, ISBN 82-7119-220-5, ISSN 0802-3271.

"Visualization of Results from Mechanical Engineering Analysis",
K. Aamnes, 1990:63, ISBN 82-7119-221-3, ISSN 0802-3271.

"Object-Oriented Product Modeling for Structural Design",
S. I. Dale, 1991:6, ISBN 82-7119-258-2, ISSN 0802-3271.

"Parallel Techniques for Solving Finite Element Problems on Transputer Networks",
T. H. Hansen, 1991:19, ISBN 82-7119-273-6, ISSN 0802-3271.

"Statistical Description and Estimation of Ocean Drift Ice Environments",
R. Korsnes, 1991:24, ISBN 82-7119-278-7, ISSN 0802-3271.

“Properties of concrete related to fatigue damage: with emphasis on high strength concrete”,
G. Petkovic, 1991:35, ISBN 82-7119-290-6, ISSN 0802-3271.

"Turbidity Current Modelling",
B. Brørs, 1991:38, ISBN 82-7119-293-0, ISSN 0802-3271.

"Zero-Slump Concrete: Rheology, Degree of Compaction and Strength. Effects of Fillers as Part Cement-Replacement",
C. Sørensen, 1992:8, ISBN 82-7119-357-0, ISSN 0802-3271.

"Nonlinear Analysis of Reinforced Concrete Structures Exposed to Transient Loading",
K. V. Høiseth, 1992:15, ISBN 82-7119-364-3, ISSN 0802-3271.

"Finite Element Formulations and Solution Algorithms for Buckling and Collapse Analysis of Thin Shells",
R. O. Bjærum, 1992:30, ISBN 82-7119-380-5, ISSN 0802-3271.

"Response Statistics of Nonlinear Dynamic Systems",
J. M. Johnsen, 1992:42, ISBN 82-7119-393-7, ISSN 0802-3271.

"Digital Models in Engineering. A Study on why and how engineers build and operate digital models for decisison support",
J. Høyte, 1992:75, ISBN 82-7119-429-1, ISSN 0802-3271.

"Sparse Solution of Finite Element Equations",
A. C. Damhaug, 1992:76, ISBN 82-7119-430-5, ISSN 0802-3271.

"Some Aspects of Floating Ice Related to Sea Surface Operations in the Barents Sea",
S. Løset, 1992:95, ISBN 82-7119-452-6, ISSN 0802-3271.

"Modelling of Cyclic Plasticity with Application to Steel and Aluminium Structures",
O. S. Hopperstad, 1993:7, ISBN 82-7119-461-5, ISSN 0802-3271.

"The Free Formulation: Linear Theory and Extensions with Applications to Tetrahedral Elements
with Rotational Freedoms",
G. Skeie, 1993:17, ISBN 82-7119-472-0, ISSN 0802-3271.

"Høyfast betongs motstand mot piggdekkslitasje. Analyse av resultater fra prøving i Veisliter'n",
T. Tveter, 1993:62, ISBN 82-7119-522-0, ISSN 0802-3271.

"A Nonlinear Finite Element Based on Free Formulation Theory for Analysis of Sandwich Structures",
O. Aamlid, 1993:72, ISBN 82-7119-534-4, ISSN 0802-3271.

"The Effect of Curing Temperature and Silica Fume on Chloride Migration and Pore Structure of High Strength Concrete",
C. J. Hauck, 1993:90, ISBN 82-7119-553-0, ISSN 0802-3271.

"Failure of Concrete under Compressive Strain Gradients",
G. Markeset, 1993:110, ISBN 82-7119-575-1, ISSN 0802-3271.

"An experimental study of internal tidal amphidromes in Vestfjorden",
J. H. Nilsen, 1994:39, ISBN 82-7119-640-5, ISSN 0802-3271.

"Structural analysis of oil wells with emphasis on conductor design",
H. Larsen, 1994:46, ISBN 82-7119-648-0, ISSN 0802-3271.

"Adaptive methods for non-linear finite element analysis of shell structures",
K. M. Okstad, 1994:66, ISBN 82-7119-670-7, ISSN 0802-3271.

"On constitutive modelling in nonlinear analysis of concrete structures",
O. Fyrileiv, 1994:115, ISBN 82-7119-725-8, ISSN 0802-3271.

"Fluctuating wind load and response of a line-like engineering structure with emphasis on motion-induced wind forces",
J. Bogunovic Jakobsen, 1995:62, ISBN 82-7119-809-2, ISSN 0802-3271.

"An experimental study of beam-columns subjected to combined torsion, bending and axial actions",
A. Aalberg, 1995:66, ISBN 82-7119-813-0, ISSN 0802-3271.

"Scaling and cracking in unsealed freeze/thaw testing of Portland cement and silica fume concretes",
S. Jacobsen, 1995:101, ISBN 82-7119-851-3, ISSN 0802-3271.

"Damping of water waves by submerged vegetation. A case study of laminaria hyperborea",
A. M. Dubi, 1995:108, ISBN 82-7119-859-9, ISSN 0802-3271.

"The dynamics of a slope current in the Barents Sea",
Sheng Li, 1995:109, ISBN 82-7119-860-2, ISSN 0802-3271.

"Modellering av delmaterialenes betydning for betongens konsistens",
Ernst Mørtsell, 1996:12, ISBN 82-7119-894-7, ISSN 0802-3271.

"Bending of thin-walled aluminium extrusions",
Birgit Søvik Opheim, 1996:60, ISBN 82-7119-947-1, ISSN 0802-3271.

"Material modelling of aluminium for crashworthiness analysis",
Torodd Berstad, 1996:89, ISBN 82-7119-980-3, ISSN 0802-3271.

"Estimation of structural parameters from response measurements on submerged floating tunnels",
Rolf Magne Larssen, 1996:119, ISBN 82-471-0014-2, ISSN 0802-3271.

“Numerical modelling of plain and reinforced concrete by damage mechanics”,
Mario A. Polanco-Loria, 1997:20, ISBN 82-471-0049-5, ISSN 0802-3271.

“Nonlinear random vibrations - numerical analysis by path integration methods”,
Vibeke Moe, 1997:26, ISBN 82-471-0056-8, ISSN 0802-3271.

“Numerical prediction of vortex-induced vibration by the finite element method”,
Joar Martin Dalheim, 1997:63, ISBN 82-471-0096-7, ISSN 0802-3271.

“Time domain calculations of buffeting response for wind sensitive structures”,
Ketil Aas-Jakobsen, 1997:148, ISBN 82-471-0189-0, ISSN 0802-3271.

"A numerical study of flow about fixed and flexibly mounted circular cylinders",
Trond Stokka Meling, 1998:48, ISBN 82-471-0244-7, ISSN 0802-3271.

“Estimation of chloride penetration into concrete bridges in coastal areas”,
Per Egil Steen, 1998:89, ISBN 82-471-0290-0, ISSN 0802-3271.

“Stress-resultant material models for reinforced concrete plates and shells”,
Jan Arve Øverli, 1998:95, ISBN 82-471-0297-8, ISSN 0802-3271.

“Chloride binding in concrete. Effect of surrounding environment and concrete composition”,
Claus Kenneth Larsen, 1998:101, ISBN 82-471-0337-0, ISSN 0802-3271.

“Rotational capacity of aluminium alloy beams”,
Lars A. Moen, 1999:1, ISBN 82-471-0365-6, ISSN 0802-3271.

“Stretch Bending of Aluminium Extrusions”,
Arild H. Clausen, 1999:29, ISBN 82-471-0396-6, ISSN 0802-3271.

“Aluminium and Steel Beams under Concentrated Loading”,
Tore Tryland, 1999:30, ISBN 82-471-0397-4, ISSN 0802-3271.

"Engineering Models of Elastoplasticity and Fracture for Aluminium Alloys",
Odd-Geir Lademo, 1999:39, ISBN 82-471-0406-7, ISSN 0802-3271.

"Kapasitet og duktilitet av dybelforbindelser i trekonstruksjoner",
Jan Siem, 1999:46, ISBN 82-471-0414-8, ISSN 0802-3271.

“Etablering av distribuert ingeniørarbeid; Teknologiske og organisatoriske erfaringer fra en norsk ingeniørbedrift”,
Lars Line, 1999:52, ISBN 82-471-0420-2, ISSN 0802-3271.

“Estimation of Earthquake-Induced Response”,
Símon Ólafsson, 1999:73, ISBN 82-471-0443-1, ISSN 0802-3271.

“Coastal Concrete Bridges: Moisture State, Chloride Permeability and Aging Effects”
Ragnhild Holen Relling, 1999:74, ISBN 82-471-0445-8, ISSN 0802-3271.

”Capacity Assessment of Titanium Pipes Subjected to Bending and External Pressure”,
Arve Bjørset, 1999:100, ISBN 82-471-0473-3, ISSN 0802-3271.

“Validation of Numerical Collapse Behaviour of Thin-Walled Corrugated Panels”,
Håvar Ilstad, 1999:101, ISBN 82-471-0474-1, ISSN 0802-3271.

“Strength and Ductility of Welded Structures in Aluminium Alloys”,
Miroslaw Matusiak, 1999:113, ISBN 82-471-0487-3, ISSN 0802-3271.

“Thermal Dilation and Autogenous Deformation as Driving Forces to Self-Induced Stresses in High Performance Concrete”,
Øyvind Bjøntegaard, 1999:121, ISBN 82-7984-002-8, ISSN 0802-3271.

“Some Aspects of Ski Base Sliding Friction and Ski Base Structure”,
Dag Anders Moldestad, 1999:137, ISBN 82-7984-019-2, ISSN 0802-3271.

"Electrode reactions and corrosion resistance for steel in mortar and concrete",
Roy Antonsen, 2000:10, ISBN 82-7984-030-3, ISSN 0802-3271.

"Hydro-Physical Conditions in Kelp Forests and the Effect on Wave Damping and Dune Erosion. A case study on Laminaria Hyperborea",
Stig Magnar Løvås, 2000:28, ISBN 82-7984-050-8, ISSN 0802-3271.

"Random Vibration and the Path Integral Method",
Christian Skaug, 2000:39, ISBN 82-7984-061-3, ISSN 0802-3271.

"Buckling and geometrical nonlinear beam-type analyses of timber structures",
Trond Even Eggen, 2000:56, ISBN 82-7984-081-8, ISSN 0802-3271.

”Structural Crashworthiness of Aluminium Foam-Based Components”,
Arve Grønsund Hanssen, 2000:76, ISBN 82-7984-102-4, ISSN 0809-103X.

“Measurements and simulations of the consolidation in first-year sea ice ridges, and some aspects of mechanical behaviour”,
Knut V. Høyland, 2000:94, ISBN 82-7984-121-0, ISSN 0809-103X.

”Kinematics in Regular and Irregular Waves based on a Lagrangian Formulation”,
Svein Helge Gjøsund, 2000-86, ISBN 82-7984-112-1, ISSN 0809-103X.

”Self-Induced Cracking Problems in Hardening Concrete Structures”,
Daniela Bosnjak, 2000-121, ISBN 82-7984-151-2, ISSN 0809-103X.

"Ballistic Penetration and Perforation of Steel Plates",
Tore Børvik, 2000:124, ISBN 82-7984-154-7, ISSN 0809-103X.

"Freeze-Thaw resistance of Concrete. Effect of: Curing Conditions, Moisture Exchange and Materials",
Terje Finnerup Rønning, 2001:14, ISBN 82-7984-165-2, ISSN 0809-103X

"Structural behaviour of post tensioned concrete structures. Flat slab. Slabs on ground",
Steinar Trygstad, 2001:52, ISBN 82-471-5314-9, ISSN 0809-103X.

"Slipforming of Vertical Concrete Structures. Friction between concrete and slipform panel",
Kjell Tore Fosså, 2001:61, ISBN 82-471-5325-4, ISSN 0809-103X.

"Some numerical methods for the simulation of laminar and turbulent incompressible flows",
Jens Holmen, 2002:6, ISBN 82-471-5396-3, ISSN 0809-103X.

“Improved Fatigue Performance of Threaded Drillstring Connections by Cold Rolling”,
Steinar Kristoffersen, 2002:11, ISBN: 82-421-5402-1, ISSN 0809-103X.

"Deformations in Concrete Cantilever Bridges: Observations and Theoretical Modelling",
Peter F. Takâcs, 2002:23, ISBN 82-471-5415-3, ISSN 0809-103X.

"Stiffened aluminium plates subjected to impact loading",
Hilde Giæver Hildrum, 2002:69, ISBN 82-471-5467-6, ISSN 0809-103X.

"Full- and model scale study of wind effects on a medium-rise building in a built up area",
Jónas Thór Snæbjørnsson, 2002:95, ISBN82-471-5495-1, ISSN 0809-103X.

“Evaluation of Concepts for Loading of Hydrocarbons in Ice-infested water”,
Arnor Jensen, 2002:114, ISBN 82-417-5506-0, ISSN 0809-103X.

”Numerical and Physical Modelling of Oil Spreading in Broken Ice”,
Janne K. Økland Gjøsteen, 2002:130, ISBN 82-471-5523-0, ISSN 0809-103X.

”Diagnosis and protection of corroding steel in concrete”,
Franz Pruckner, 20002:140, ISBN 82-471-5555-4, ISSN 0809-103X.

“Tensile and Compressive Creep of Young Concrete: Testing and Modelling”,
Dawood Atrushi, 2003:17, ISBN 82-471-5565-6, ISSN 0809-103X.

“Rheology of Particle Suspensions. Fresh Concrete, Mortar and Cement Paste with Various Types of Lignosulfonates”,
Jon Elvar Wallevik, 2003:18, ISBN 82-471-5566-4, ISSN 0809-103X.

“Oblique Loading of Aluminium Crash Components”,
Aase Reyes, 2003:15, ISBN 82-471-5562-1, ISSN 0809-103X.

“Utilization of Ethiopian Natural Pozzolans”,
Surafel Ketema Desta, 2003:26, ISSN 82-471-5574-5, ISSN:0809-103X.

“Behaviour and strength prediction of reinforced concrete structures with discontinuity regions”, Helge Brå, 2004:11, ISBN 82-471-6222-9, ISSN 1503-8181.

“High-strength steel plates subjected to projectile impact. An experimental and numerical study”, Sumita Dey, 2004:38, ISBN 82-471-6282-2 (printed version), ISBN 82-471-6281-4 (electronic version), ISSN 1503-8181.

“Alkali-reactive and inert fillers in concrete. Rheology of fresh mixtures and expansive reactions.”
Bård M. Pedersen, 2004:92, ISBN 82-471-6401-9 (printed version), ISBN 82-471-6400-0 (electronic version), ISSN 1503-8181.

“On the Shear Capacity of Steel Girders with Large Web Openings”.
Nils Christian Hagen, 2005:9 ISBN 82-471-6878-2 (printed version), ISBN 82-471-6877-4 (electronic version), ISSN 1503-8181.

”Behaviour of aluminium extrusions subjected to axial loading”.
Østen Jensen, 2005:7, ISBN 82-471-6873-1 (printed version), ISBN 82-471-6872-3 (electronic version), ISSN 1503-8181.

”Thermal Aspects of corrosion of Steel in Concrete”.
Jan-Magnus Østvik, 2005:5, ISBN 82-471-6869-3 (printed version), ISBN 82-471-6868 (electronic version), ISSN 1503-8181.

”Mechanical and adaptive behaviour of bone in relation to hip replacement.” A study of bone remodelling and bone grafting.
Sébastien Muller, 2005:34, ISBN 82-471-6933-9 (printed version), ISBN 82-471-6932-0 (electronic version), ISSN 1503-8181.

“Analysis of geometrical nonlinearities with applications to timber structures”.
Lars Wollebæk, 2005:74, ISBN 82-471-7050-5 (printed version), ISBN 82-471-7019-1 (electronic version), ISSN 1503-8181.

“Pedestrian induced lateral vibrations of slender footbridges”,
Anders Rönnquist, 2005:102, ISBN 82-471-7082-5 (printed version), ISBN 82-471-7081-7 (electronic version), ISSN 1503-8181.

“Initial Strength Development of Fly Ash and Limestone Blended Cements at Various Temperatures Predicted by Ultrasonic Pulse Velocity”,
Tom Ivar Fredvik, 2005:112, ISBN 82-471-7105-8 (printed version), ISBN 82-471-7103-1 (electronic version), ISSN 1503-8181.

“Behaviour and modelling of thin-walled cast components”,
Cato Dørum, 2005:128, ISBN 82-471-7140-6 (printed version), ISBN 82-471-7139-2 (electronic version), ISSN 1503-8181.

“Behaviour and modelling of selfpiercing riveted connections”,
Raffaele Porcaro, 2005:165, ISBN 82-471-7219-4 (printed version), ISBN 82-471-7218-6 (electronic version), ISSN 1503-8181.

”Behaviour and Modelling og Aluminium Plates subjected to Compressive Load”,
Lars Rønning, 2005:154, ISBN 82-471-7169-1 (printed version), ISBN 82-471-7195-3 (electronic version), ISSN 1503-8181.

”Bumper beam-longitudinal system subjected to offset impact loading”,
Satyanarayana Kokkula, 2005:193, ISBN 82-471-7280-1 (printed version), ISBN 82-471-7279-8 (electronic version), ISSN 1503-8181.

“Control of Chloride Penetration into Concrete Structures at Early Age”,
Guofei Liu, 2006:46, ISBN 82-471-7838-9 (printed version), ISBN 82-471-7837-0 (electronic version), ISSN 1503-8181.

“Modelling of Welded Thin-Walled Aluminium Structures”,
Ting Wang, 2006:78, ISBN 82-471-7907-5 (printed version), ISBN 82-471-7906-7 (electronic version), ISSN 1503-8181.

”Time-variant reliability of dynamic systems by importance sampling and probabilistic analysis of ice loads”,
Anna Ivanova Olsen, 2006:139, ISBN 82-471-8041-3 (printed version), ISBN 82-471-8040-5 (electronic version), ISSN 1503-8181.

“Fatigue life prediction of an aluminium alloy automotive component using finite element analysis of surface topography”.
Sigmund Kyrre Ås, 2006:25, ISBN 82-471-7791-9 (printed version), ISBN 82-471-7791-9 (electronic version), ISSN 1503-8181.

”Constitutive models of elastoplasticity and fracture for aluminium alloys under strain path change”,
Dasharatha Achani, 2006:76, ISBN 82-471-7903-2 (printed version), ISBN 82-471-7902-4 (electronic version), ISSN 1503-8181.

“Simulations of 2D dynamic brittle fracture by the Element-free Galerkin method and linear fracture mechanics”,
Tommy Karlsson, 2006:125, ISBN 82-471-8011-1 (printed version), ISBN 82-471-8010-3 (electronic version), ISSN 1503-8181.

“Penetration and Perforation of Granite Targets by Hard Projectiles”,
Chong Chiang Seah, 2006:188, ISBN 82-471-8150-9 (printed version), ISBN 82-471-8149-5 (electronic version), ISSN 1503-8181.

"Deformations, strain capacity and cracking of concrete in plastic and early hardening phases",
Tor Arne Hammer, 2007:234, ISBN 978-82-471-5191-4 (printed version), ISBN 978-82-471-5207-2 (electronic version), ISSN 1503-8181.

"Crashworthiness of dual-phase high-strength steel: Material and Component behaviour", Venkatapathi Tarigopula, 2007:230, ISBN 82-471-5076-4 (printed version), ISBN 82-471-5093-1 (electronic version), ISSN 1503-8181.

"Fibre reinforcement in load carrying concrete structures",
Åse Lyslo Døssland, 2008:50, ISBN 978-82-471-6910-0 (printed version), ISBN 978-82-471-6924-7 (electronic version), ISSN 1503-8181.

"Low-velocity penetration of aluminium plates",
Frode Grytten, 2008:46, ISBN 978-82-471-6826-4 (printed version), ISBN 978-82-471-6843-1 (electronic version), ISSN 1503-8181.

"Robustness studies of structures subjected to large deformations",
Ørjan Fyllingen, 2008:24, ISBN 978-82-471-6339-9 (printed version), ISBN 978-82-471-6342-9 (electronic version), ISSN 1503-8181.

"Constitutive modelling of morsellised bone",
Knut Birger Lunde, 2008:92, ISBN 978-82-471-7829-4 (printed version), ISBN 978-82-471-7832-4 (electronic version), ISSN 1503-8181.

"Experimental Investigations of Wind Loading on a Suspension Bridge Girder",
Bjørn Isaksen, 2008:131, ISBN 978-82-471-8656-5 (printed version), ISBN 978-82-471-8673-2 (electronic version), ISSN 1503-8181.

"Cracking Risk of Concrete Structures in The Hardening Phase",
Guomin Ji, 2008:198, ISBN 978-82-471-1079-9 (printed version), ISBN 978-82-471-1080-5 (electronic version), ISSN 1503-8181.

"Modelling and numerical analysis of the porcine and human mitral apparatus",
Victorien Emile Prot, 2008:249, ISBN 978-82-471-1192-5 (printed version), ISBN 978-82-471-1193-2 (electronic version), ISSN 1503-8181.

"Strength analysis of net structures",
Heidi Moe, 2009:48, ISBN 978-82-471-1468-1 (printed version), ISBN 978-82-471-1469-8 (electronic version), ISSN1503-8181.

"Numerical analysis of ductile fracture in surface cracked shells",
Espen Berg, 2009:80, ISBN 978-82-471-1537-4 (printed version), ISBN 978-82-471-1538-1 (electronic version), ISSN 1503-8181.

"Subject specific finite element analysis of bone – for evaluation of the healing of a leg lengthening and evaluation of femoral stem design",
Sune Hansborg Pettersen, 2009:99, ISBN 978-82-471-1579-4 (printed version), ISBN 978-82-471-1580-0 (electronic version), ISSN 1503-8181.

"Evaluation of fracture parameters for notched multi-layered structures",
Lingyun Shang, 2009:137, ISBN 978-82-471-1662-3 (printed version), ISBN 978-82-471-1663-0 (electronic version), ISSN 1503-8181.

"Modelling of Dynamic Material Behaviour and Fracture of Aluminium Alloys for Structural Applications"
Yan Chen, 2009:69, ISBN 978-82-471-1515-2 (printed version), ISBN 978-82 471-1516-9 (electronic version), ISSN 1503-8181.

"Nanomechanics of polymer and composite particles"
Jianying He 2009:213, ISBN 978-82-471-1828-3 (printed version), ISBN 978-82-471-1829-0 (electronic version), ISSN 1503-8181.

"Mechanical properties of clear wood from Norway spruce"
Kristian Berbom Dahl 2009:250, ISBN 978-82-471-1911-2 (printed version) ISBN 978-82-471-1912-9 (electronic version), ISSN 1503-8181.

"Modeling of the degradation of TiB_2 mechanical properties by residual stresses and liquid Al penetration along grain boundaries"
Micol Pezzotta 2009:254, ISBN 978-82-471-1923-5 (printed version) ISBN 978-82-471-1924-2 (electronic version) ISSN 1503-8181.

"Effect of welding residual stress on fracture"
Xiabo Ren 2010:77, ISBN 978-82-471-2115-3 (printed version) ISBN 978-82-471-2116-0 (electronic version), ISSN 1503-8181.

"Pan-based carbon fiber as anode material in cathodic protection system for concrete structures"
Mahdi Chini 2010:122, ISBN 978-82-471-2210-5 (printed version) ISBN 978-82-471-2213-6 (electronic version), ISSN 1503-8181.

"Structural Behaviour of deteriorated and retrofitted concrete structures"
Irina Vasililjeva Sæther 2010:171, ISBN 978-82-471-2315-7 (printed version) ISBN 978-82-471-2316-4 (electronic version) ISSN 1503-8181.

"Prediction of local snow loads on roofs"
Vivian Meløysund 2010:247, ISBN 978-82-471-2490-1 (printed version) ISBN 978-82-471-2491-8 (electronic version) ISSN 1503-8181.

"Behaviour and modelling of polymers for crash applications"
Virgile Delhaye 2010:251, ISBN 978-82-471-2501-4 (printed version) ISBN 978-82-471-2502-1 (electronic version) ISSN 1503-8181.

"Blended cement with reducted CO_2 emission – Utilizing the Fly Ash-Limestone Synergy",
Klaartje De Weerdt 2011:32, ISBN 978-82-471-2584-7 (printed version) ISBN 978-82-471-2584-4 (electronic version) ISSN 1503-8181.

"Chloride induced reinforcement corrosion in concrete" Concept of critical chloride content – methods and mechanisms.
Ueli Angst 2011:113, ISBN 978-82-471-2769-9 (printed version) ISBN 978-82-471-2763-6 (electronic version) ISSN 1503-8181.

"A thermo-electric-Mechanical study of the carbon anode and contact interface for Energy savings in the production of aluminium".
Dag Herman Andersen 2011:157, ISBN 978-82-471-2859-6 (printed version) ISBN 978-82-471-2860-2 (electronic version) ISSN 1503-8181.

"Structural Capacity of Anchorage Ties in Masonry Veneer Walls Subjected to Earthquake". The implications of Eurocode 8 and Eurocode 6 on a typical Norwegain veneer wall.
Ahmed Mohamed Yousry Hamed 2011:181, ISBN 978-82-471-2911-1 (printed version) ISBN 978-82-471-2912-8 (electronic ver.) ISSN 1503-8181.

"Work-hardening behaviour in age-hardenable Al-Zn-Mg(-Cu) alloys".
Ida Westermann , 2011:247, ISBN 978-82-471-3056-8 (printed ver.) ISBN 978-82-471-3057-5 (electronic ver.) ISSN 1503-8181.

"Behaviour and modelling of selfpiercing riveted connections using aluminium rivets".
Nguyen-Hieu Hoang, 2011:266, ISBN 978-82-471-3097-1 (printed ver.) ISBN 978-82-471-3099-5 (electronic ver.) ISSN 1503-8181.

"Fibre reinforced concrete".
Sindre Sandbakk, 2011:297, ISBN 978-82-471-3167-1 (printed ver.) ISBN 978-82-471-3168-8 (electronic ver) ISSN 1503:8181.

"Dynamic behaviour of cablesupported bridges subjected to strong natural wind".
Ole Andre Øiseth, 2011:315, ISBN 978-82-471-3209-8 (printed ver.) ISBN 978-82-471-3210-4 (electronic ver.) ISSN 1503-8181.

"Constitutive modeling of solargrade silicon materials"
Julien Cochard, 2011:307, ISBN 978-82-471-3189-3 (printed ver). ISBN 978-82-471-3190-9 (electronic ver.) ISSN 1503-8181.

"Constitutive behavior and fracture of shape memory alloys"
Jim Stian Olsen, 2012:57, ISBN 978-82-471-3382-8 (printed ver.) ISBN 978-82-471-3383-5 (electronic ver.) ISSN 1503-8181.

“Field measurements in mechanical testing using close-range photogrammetry and digital image analysis”
Egil Fagerholt, 2012:95, ISBN 978-82-471-3466-5 (printed ver.) ISBN 978-82-471-3467-2 (electronic ver.) ISSN 1503-8181.

“Towards a better under standing of the ultimate behaviour of lightweight aggregate concrete in compression and bending”,
Håvard Nedrelid, 2012:123, ISBN 978-82-471-3527-3 (printed ver.) ISBN 978-82-471-3528-0 (electronic ver.) ISSN 1503-8181.

“Numerical simulations of blood flow in the left side of the heart”
Sigrid Kaarstad Dahl, 2012:135, ISBN 978-82-471-3553-2 (printed ver.) ISBN 978-82-471-3555-6 (electronic ver.) ISSN 1503-8181.

“Moisture induced stresses in glulam”
Vanessa Angst-Nicollier, 2012:139, ISBN 978-82-471-3562-4 (printed ver.) ISBN 978-82-471-3563-1 (electronic ver.) ISSN 1503-8181.

“Biomechanical aspects of distraction osteogensis”
Valentina La Russa, 2012:250, ISBN 978-82-471-3807-6 (printed ver.) ISBN 978-82-471-3808-3 (electronic ver.) ISSN 1503-8181.

“Ductile fracture in dual-phase steel. Theoretical, experimental and numerical study”
Gaute Gruben, 2012:257, ISBN 978-82-471-3822-9 (printed ver.) ISBN 978-82-471-3823-6 (electronic ver.) ISSN 1503-8181.

“Damping in Timber Structures”
Nathalie Labonnote, 2012:263, ISBN 978-82-471-3836-6 (printed ver.) ISBN 978-82-471-3837-3 (electronic ver.) ISSN 1503-8181.

“Biomechanical modeling of fetal veins: The umbilical vein and ductus venosus bifurcation”
Paul Roger Leinan, 2012:299, ISBN 978-82-471-3915-8 (printed ver.) ISBN 978-82-471-3916-5 (electronic ver.) ISSN 1503-8181.

“Large-Deformation behaviour of thermoplastics at various stress states”
Anne Serine Ognedal, 2012:298, ISBN 978-82-471-3913-4 (printed ver.) ISBN 978-82-471-3914-1 (electronic ver.) ISSN 1503-8181.

“Hardening accelerator for fly ash blended cement”
Kien Dinh Hoang, 2012:366, ISBN 978-82-471-4063-5 (printed ver.) ISBN 978-82-471-4064-2 (electronic ver.) ISSN 1503-8181.

“From molecular structure to mechanical properties”
Jianyang Wu, 2013:186, ISBN 978-82-471-4485-5 (printed ver.) ISBN 978-82-471-4486-2 (electronic ver.) ISSN 1503-8181.

“Experimental and numerical study of hybrid concrete structures”
Linn Grepstad Nes, 2013:259, ISBN 978-82-471-4644-6 (printed ver.) ISBN 978-82-471-4645-3 (electronic ver.) ISSN 1503-8181.

“Mechanics of ultra-thin multi crystalline silicon wafers”
Saber Saffar, 2013:199, ISBN 978-82-471-4511-1 (printed ver.) ISBN 978-82-471-4513-5 (electronic ver). ISSN 1503-8181.

“Through process modelling of welded aluminium structures”
Anizahyati Alisibramulisi, 2013:325, ISBN 978-82-471-4788-7 (printed ver.) ISBN 978-82-471-4789-4 (electronic ver.) ISSN 1503-8181.

“Combined blast and fragment loading on steel plates”
Knut Gaarder Rakvåg, 2013:361, ISBN978-82-471-4872-3 (printed ver.) ISBN 978-82-4873-0 (electronic ver.). ISSN 1503-8181.

“Characterization and modelling of the anisotropic behaviour of high-strength aluminium alloy”
Marion Fourmeau, 2014:37, ISBN 978-82-326-0008-3 (printed ver.) ISBN 978-82-326-0009-0 (electronic ver.) ISSN 1503-8181.

“Behaviour of threated steel fasteners at elevated deformation rates”
Henning Fransplass, 2014:65, ISBN 978-82-326-0054-0 (printed ver.) ISBN 978-82-326-0055-7 (electronic ver.) ISSN 1503-8181.

“Sedimentation and Bleeding”
Ya Peng, 2014:89, ISBN 978-82-326-0102-8 (printed ver.) ISBN 978-82-326-0103-5 (electric ver.) ISSN 1503-8181.

“Impact against X65 offshore pipelines”
Martin Kristoffersen, 2014:362, ISBN 978-82-326-0636-8 (printed ver.) ISBN 978-82-326-0637-5 (electronic ver.) ISSN 1503-8181.

“Formability of aluminium alloy subjected to prestrain by rolling”
Dmitry Vysochinskiy, 2014:363,, ISBN 978-82-326-0638-2 (printed ver.) ISBN 978-82-326-0639-9 (electronic ver.) ISSN 1503-8181.

“Experimental and numerical study of Yielding, Work-Hardening and anisotropy in textured AA6xxx alloys using crystal plasticity models”
Mikhail Khadyko, 2015:28, ISBN 978-82-326-0724-2 (printed ver.) ISBN 978-82-326-0725-9 (electronic ver.) ISSN 1503-8181.

“Behaviour and Modelling of AA6xxx Aluminium Alloys Under a Wide Range of Temperatures and Strain Rates”
Vincent Vilamosa, 2015:63, ISBN 978-82-326-0786-0 (printed ver.) ISBN 978-82-326-0787-7 (electronic ver.) ISSN 1503-8181.

“A Probabilistic Approach in Failure Modelling of Aluminium High Pressure Die-Castings”
Octavian Knoll, 2015:137, ISBN 978-82-326-0930-7 (printed ver.) ISBN 978-82-326-0931-4 (electronic ver.) ISSN 1503-8181.

“Ice Abrasion on Marine Concrete Structures”
Egil Møen, 2015:189, ISBN 978-82-326-1034-1 (printed ver.) ISBN 978-82-326-1035-8 (electronic ver.) ISSN 1503-8181.

“Fibre Orientation in Steel-Fibre-Reinforced Concrete”
Giedrius Zirgulis, 2015:229, ISBN 978-82-326-1114-0 (printed ver.) ISBN 978-82-326-1115-7 (electronic ver.) ISSN 1503-8181.

“Effect of spatial variation and possible interference of localised corrosion on the residual capacity of a reinforced concrete beam”
Mohammad Mahdi Kioumarsi, 2015:282, ISBN 978-82-326-1220-8 (printed ver.) ISBN 978-82-1221-5 (electronic ver.) ISSN 1503-8181.

“The role of concrete resistivity in chloride-induced macro-cell corrosion”
Karla Horbostel, 2015:324, ISBN 978-82-326-1304-5 (printed ver.) ISBN 978-82-326-1305-2 (electonic ver.) ISSN 1503-8181.

“Flowable fibre-reinforced concrete for structural applications”
Elena Vidal Sarmiento, 2015-335, ISBN 978-82-326-1324-3 (printed ver.) ISBN 978-82-326-1325-0 (electronic ver.) ISSN 1503-8181.

“Development of chushed sand for concrete production with microproportioning”
Rolands Cepuritis, 2016:19, ISBN 978-82-326-1382-3 (printed ver.) ISBN 978-82-326-1383-0 (electronic ver.) ISSN 1503-8181.

“Withdrawal properties of threaded rods embedded in glued-laminated timer elements”
Haris Stamatopoulos, 2016:48, ISBN 978-82-326-1436-3 (printed ver.) ISBN 978-82-326-1437-0 (electronic ver.) ISSN 1503-8181.

“An Experimental and numerical study of thermoplastics at large deformation”
Marius Andersen, 2016:191, ISBN 978-82-326-1720-3 (printed ver.) ISBN 978-82-326-1721-0 (electronic ver.) ISSN 1503-8181.

“Modeling and Simulation of Ballistic Impact”
Jens Kristian Holmen, 2016:240, ISBN 978-82-326-1818-7 (printed ver). ISBN 978-82-326-1819-4 (electronic ver.) ISSN 1503-8181.

“Early age crack assessment of concrete structures”
Anja B. Estensen Klausen, 2016:256, ISBN 978-82-326-1850-7 (printed ver). ISBN 978-82-326-1851-4 (electronic ver.) ISSN 1503-8181.

"Uncertainty quantification and sensitivity analysis for cardiovascular models"
Vinzenz Gregor Eck, 2016:234, ISBN 978-82-326-1806-4 (printed ver.) ISBN 978-82-326-1807-1 (electronic ver.) ISSN 1503-8181.

"Dynamic behaviour of existing and new railway catenary systems under Norwegain conditions"
Petter Røe Nåvik, 2016:298, ISBN 978-82-326-1935-1 (printed ver.) ISBN 978-82-326-1934-4 (electronic ver.) ISSN 1503-8181.

"Mechanical behaviour of particle-filled elastomers at various temperatures"
Arne Ilseng, 2016-295, ISBN978-82-326-1928-3 (printed ver.) ISBN 978-82-326-1929-0 (electronic ver.) ISSN 1503-8181.

"Nanotechnology for Anti-Icing Application"
Zhiwei He, 2016:348, ISBN 978-82-326-2038-8 (printed ver.) ISBN 978-82-326-2019-5 (electronic ver.) ISSN 1503-8181.

"Conduction Mechanisms in Conductive Adhesives with Metal-Coated Polyer Spheres"
Sigurd Rolland Pettersen, 2016:349, ISBN 978-326-2040-1 (printed ver,) ISBN 978-82-326-2041-8 (electronic ver.) ISSN 1503-8181.

"The interaction between calcium lignosulfonate and cement"
Alessia Colombo, 2017:20, ISBN 978-82-326-2122-4 (printed ver.) ISBN 978-82-326-2123-1 (electronic ver.) ISSN 1503-8181.

"Behaviour and Modelling of Flexible Structures Subjected to Blast Loading"
Vegard Aune, 2017:101, ISBN 978-82-326-2274-0 (printed ver.) ISBN 978-82-326-2275-7 (electronic ver.) ISSN 1503-8181.

"Behaviour of steel connections under quasi-static and impact loading"
Erik Løhre Grimsmo, 2017:159, ISBN 978-82-326-2390-7 (printed ver.) ISBN 978-82-326-2391-4 (electronic ver.) ISSN 1503-8181.

"An experimental and numerical study of cortical bone at he macro and Nano-scale"
Masoud Ramenzanzadehkoldeh,, 2017:208, ISBN 978-82-326-2488-1 (printed ver.) ISBN 978-82-326-2489-8 (electronic ver.) ISSN 1503-8181.

"Optoelectrical Properties of a Novel Organic Semiconductor: 6,13-Dichloropentacene"
Mao Wang, 2017:130, ISBN 978-82-326-2332-7 (printed ver.) ISBN 978-82-326-2333-4) (electronic ver.) ISSN 1503-8181.

"Core-shell structured microgels and their behavior at oil and water interface"
Yi Gong, 2017:182, ISBN 978-82-326-2436-2 (printed. ver.) ISBN 978-82-326-2437-9 (electronic ver.) ISSN 1503-8181.

“Aspects of design of reinforced concrete structures using nonliear finite element analyses”
Morten Engen, 2017:149, ISBN 978-82-326-2370-9 (printed ver.) ISBN 978-82-326-2371-6 (electronic ver.) ISSN 1503-8181.

“Numerical studies on ductile failure of aluminium alloys”
Lars Edvard Dæhli, 2017:284, ISBN 978-82-326-2636-6 (printed ver.) ISBN 978-82-326-2637-3 (electronic ver.) ISSN 1503-8181.

“Modelling and Assessment of Hydrogen Embrittlement in Steels and Nickel Alloys”
Haiyang Yu, 2017:278, ISBN 978-82-326-2624-3 (printed. ver.) ISBN 978-82-326-2625-0 (electronic ver.) ISSN 1503-8181.

“Network arch timber bridges with light timber deck on transverse crossbeams”
Anna Weronika Ostrycharczyk, 2017:318, ISBN 978-82-326-2704-2 (printed ver.) ISBN 978-82-326-2705-9 (electronic ver.) ISSN 1503-8181.

“Splicing of Large Glued Laminated Timber Elements by Use of Long Threated Rods”
Martin Cepelka, 2017:320, ISBN 978-82-326-2708-0 (printed ver.) ISBN 978-82-326-2709-7 (electronic ver.) ISSN 1503-8181.

“Thermomechanical behaviour of semi-crystalline polymers: experiments, modelling and simulation”
Joakim Johnsen, 2017-317, ISBN 978-82-326-2702-8 (printed ver.) ISBN 978-82-326-2703-5 (electronic ver.) ISSN 1503-8181.